Università degli Studi di Trieste
Sede Amministrativa del Dottorato di Ricerca

Dottorato di Ricerca in
Nanotecnologie

XXI ciclo

Extensive oxidation treatments: ageing effects on a catalytic model system studied in UHV by STM

(SSD FIS/03–Fisica della Materia)

Dottoranda
Cecilia Blasetti

Direttore della Scuola
Chiar.mo Prof. Maurizio Fermeglia (Università di Trieste)

Supervisore
Chiar.mo Prof. Giovanni Comelli (Università di Trieste)

Tutore
Dr. Cristina Africh (Università di Trieste, CNR-INFM Laboratorio TASC)

Tutore
Dr. Friedrich Esch (CNR-INFM Laboratorio TASC)

Anno accademico 2007–2008

φύσις κρύπτεσθαι φιλεῖ.

Heraclitus

A Francesco

Abstract

This thesis concerns a surface science approach for the investigation of the ageing process of a model catalyst. It combines extreme oxidation conditions with Ultra High Vacuum (UHV) compatible characterization techniques. Our model system was the surface oxide formed on Rh(110); to grow such oxide, we used three alternative oxygen sources, optimizing for each case the preparation recipe. When dosing molecular oxygen, pressures in the $\sim 10^{-4}$ mbar range were used, therefore bridging, to some extent, the pressure gap. For characterization of the oxides we used mainly Scanning Tunneling Microscopy (STM) and Thermal Desorption Spectroscopy (TDS), providing atomic scale and desorption mechanism information, respectively. Low Energy Electron Microscopy (LEEM) and X-ray Photoelectron Specroscopy (XPS) complemented our measurements with large scale morphology and reactivity data and with chemically resolved results. To mimic real catalytic conditions, we setup an ageing protocol consisting of cycles of oxidation and annealing in UHV (up to more than ~ 40), with each of the three oxygen sources. In this way, we were able to observe two different kinds of ageing: a "contaminant-driven" and an "intrinsic" one, caused by the iterative oxidation procedure. The latter is connected to the presence of a new species we detected on the (1×1) surface obtained after the oxide desorption, that we named "units" (or ageing fingerprints). By decreasing their number we were able to show that the intrinsic ageing is, at least partially, reversible. We could not uniquely determine the structure of the "units", but plausible models are proposed.

Sommario

Questa tesi si occupa dello studio dell'invecchiamento artificiale di un catalizzatore modello, combinando condizioni di ossidazione estreme con le tecniche di caratterizzazione, compatibili con l'ultra-alto-vuoto (UHV), proprie della scienza delle superfici. Il nostro sistema modello era l'ossido superficiale formato sul Rh(110); per crescere questo ossido, abbiamo utilizzato tre sorgenti alternative di ossigeno, ed abbiamo ottimizzato la ricetta di preparazione nei singoli casi. Utilizzando l'ossigeno molecolare abbiamo dosato a pressioni dell'ordine di $\sim 10^{-4}$ mbar, ed in questo modo abbiamo in parte colmato la "pressure gap" che solitamente divide gli studi su sistemi modello da quelli di catalisi reale. Per caratterizzare gli ossidi abbiamo usato principalmente la microscopia a scansione ad effetto tunnel STM e la spettroscopia di desorbimento termico TDS, che ci hanno fornito rispettivamente informazioni su scala atomica e sul meccanismo di desorbimento. Le tecniche LEEM e XPS hanno contribuito in modo complementare alle nostre misure con dati di morfologia e reattività su larga scala, da un lato, e con dati risolti chimicamente, dall'altro. Per simulare le condizioni della catalisi reale, abbiamo sviluppato un protocollo di invecchiamento ("ageing") composto da cicli di ossidazione e riscaldamento in ultra-alto-vuoto (fino a ~ 40), con ognuna delle tre sorgenti di ossigeno. Seguendo questa procedura, abbiamo osservato due diversi tipi di invecchiamento dell'ossido di rodio: un primo tipo dominato dalla presenza di contaminanti, ed un secondo invece che abbiamo chiamato "intrinseco", causato cioè dalle ripetute ossidazioni. Quest'ultimo dipende dalla presenza di una nuova specie osservata sulla superficie (1×1) che si ottiene a seguito del desorbimento di ciascun ossido, che abbiamo chiamato "units" (o -ageing fingerprint-). Riducendo la densità di questa specie siamo stati in grado di mostrare come l'invecchiamento intrinseco sia, almeno in parte, reversibile. Non abbiamo potuto determinare univocamente la struttura delle "units", ma alcuni modelli possibili vengono proposti.

Contents

Chapter 1

Introduction

A catalyst is a material that facilitates a reaction so that it can occur under energetically favourable, milder conditions of pressure and temperature. Catalysis is fundamental for a wealth of reactions that are important for our daily needs: production of chemicals like fertilizers, energy production and conversion, pollution control. It is also at the basis of our lives: enzymes in our body, in fact, are among the most specific catalysts [1–4].

A great number of the industrially relevant reactions apply "heterogeneous" catalysts. "Heterogeneous" indicates that the catalyst and reactants are in different phases; typically the catalyst is a solid, while the reactants are liquid or gases. A real catalyst usually consists of a support material, on top of which the active species are deposited, in order to maximize both surface area and mechanical strength [5].

Transition metals of the $4d$ group (Ru,Rh,Pd and Ag) are among the most used active metals, since they can adopt a variety of coordination numbers and oxidation states. They are nowadays also finding increased use in organic reactions, in the synthesis of biologically active compounds under sufficiently mild conditions, and in the treatment of contaminated water. Rhodium, in particular, is a well-known catalyst for hydrocarbon and CO oxidation, as well as for NOx reduction in automotive Three Way Catalyst (TWC) [4, 6, 7].

Rational catalyst design requires the knowledge of the structure-reactivity relationship, down to the atomic level. This is one of the goals of *Surface Science*, that has developed a great number of techniques to study extended model surfaces, i.e. surfaces that are well-defined and much less complex than industrial catalytic systems. Figure 1.1 shows a schematic view of a typical model catalyst: a metallic single crystal is used as a substrate for a thin oxide film, over which nanoparticles are deposited as the active phase. This approach

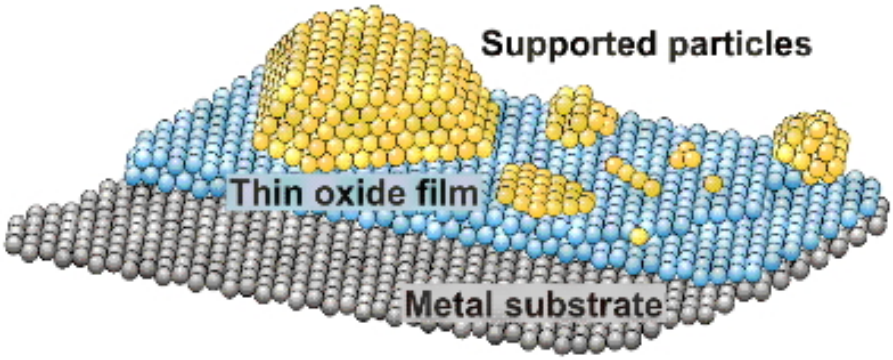

Figure 1.1: Schematic of a typical surface science compatible model catalyst (adapted from [15]).

is fruitful for tackling catalytic questions of increasing complexity, as described in the literature ([8–12]) and in the review book by Niemantsverdriet [13]. The Nobel prize in chemistry assigned in 2007 to professor Ertl for his surface science studies of the ammonia production reactions testifies the key role of basic research for issues of industrial, global importance. In some cases, atomic-scale insights opened the possibility of controlling crucial aspects of catalysis and directly lead to the development of a real, patented catalyst with improved performance: the BRIM^{TM} catalyst for hydrodesulfurization, for example, is based on model studies by the group of Besenbacher on MoS_2 nanoclusters [14].

The relevant properties of a catalyst are its *activity*, *selectivity* and *stability*. The activity is a measure of the rate increase of the reaction of interest, while the selectivity is the capability to favour a desired product (or limit undesired byproducts). Stability means how the catalytic properties, including mechanical ones, evolve with time: standard requirements consist in thousands of hours of continuous operation, before any significant deactivation is observed. The progressive deterioration of a catalyst is referred to as *ageing*, and a wealth of real catalysis studies have addressed the task of slowing down the ageing or of reactivating an aged catalyst [16–18].

Up to know, only few surface science studies have addressed the ageing of a model catalyst, and most examples refer to the poisoning problem [14]. For the catalysis of oxidation reactions, such as CO and hydrocarbon oxidation on automotive catalysts, one of the most challenging ageing effects results from the oxidizing atmosphere at high temperatures. Since the interaction of transition metals with oxygen is strong, the ageing effects can be dramatic [16, 17].

Studies over model catalysts have to face not only the "material gap" (the difference from the industrial system), but also the so-called "pressure gap", i.e. the difference in pressure of several orders of magnitude between the laboratory and the industrial environment. As a general rule, higher pressures favour the formation of O-rich phases. To bridge this gap and in order to enhance surface oxidation, many different attempts have been made [19, 20]. A first approach is to realize special instruments to use surface science techniques at high pressure ("*in-situ*" measurements). Two of the most significant examples are the "Reactor-STM" developed by Frenken and coworkers, capable of looking into catalytic reactions while operating at $\sim 5\,\mathrm{bar}$, and the specifically designed Surface X-ray Diffraction beamlines, that operate at high pressures and temperatures [21, 22]. A second way is to prepare the sample in a separate chamber, where pressures up to several mbars can be reached, and then transfer it to UHV for characterization ("*ex-situ*"). A third possibility is to perform the oxidation with highly efficient methods (based on O radicals), therefore remaining in UHV for both preparation and characterization.

In this thesis we used the last approach and we tackled the ageing of a model catalyst under oxidation conditions while retaining the possibility, given by surface science techniques and instrumentation, of performing detailed measurements down to the atomic scale level. Accordingly, the systems were prepared and characterized in an UHV environment. For oxidation we employed three different, UHV compatible, oxygen sources: a thermal cracker and a plasma source supplying atomic oxygen, and a doser providing molecular oxygen at high pressures; in this last case we reached the pressure limits of the experimental setup and somehow bridged the pressure gap.

The ageing under oxidation conditions is expected to strongly involve the oxidizability of the surface. Surface oxides grown on $4d$ transition metals are important as precursor states for bulk oxides formation: in the case of Rhodium [23–26] the thin layers, formed even in UHV ambient, have shown to kinetically hinder the incorporation of oxygen into deeper layers of the crystal, which is commonly the critical step for the growth of a bulk-like oxide [20, 27–32].

The oxidative ageing touches therefore one of the central questions of the research on transition metal catalysts in the last years: which is the active state, the oxidized (insulator) or the reduced (metal) one? When oxidation reactions are carried out, the oxidation of the catalyst itself may play a major role in the overall catalytic activity. Therefore a great number of studies has addressed

the problem of determining which is the active state between the metal and the oxidized phases. The results depend on both the reactions investigated and the materials: as an example, Pt oxide was found to be the active phase in catalytic CO oxidation, while metallic Pd proved to be the active phase for alcohol oxidation ([19, 33–37] and references therein).

Finally, ageing effects on oxidizability are not only relevant for catalysis, but also for studies concerning corrosion, addressing questions like *why* and *how* a metal rusts.

Despite the large number of surface science studies on surface oxides, and of real catalysis studies about laboratory simulated ageing, there is a lack of ageing investigation on model systems.

In this context, our aim has been to exploit the capabilities of UHV techniques and equipment for setting up an ageing procedure of a Rh(110) surface oxide. We developed an oxidation cycle protocol alternating oxidation and annealing. To monitor the morphology changes at the sub-nanometer scale, we performed Scanning Tunneling Microscopy (STM) measurements on progressively aged oxides. With Thermal Desorption Spectroscopy (TDS) we investigated the oxide desorption mechanism and how it evolves during the cycles; Low Energy Electron Microscopy (LEEM) and X-ray Photoelectron Specroscopy (XPS) data added complementary information on the micrometer scale structure and reactivity of our system. We were then able to observe two kinds of ageing: a poisoning due to external contaminations, but also an "intrinsic" ageing, induced by the iterative oxidation and heating of the rhodium crystal.

This thesis is organized as follows: Chapter 2 provides an overview of the experimental techniques that were used in this work, and Chapter 3 presents the experimental equipment. Chapter 4 presents the growth of surface oxides on the low-index rhodium surfaces, and our results concerning the Rh(110) surface oxide. Chapter 5 deals with the oxidation cycle procedures, containing a thorough overview of the ageing effects that were observed; Chapter 6 is dedicated to a new species that was accumulated during the cycles on the (1×1) surface obtained after each oxide desorption. This species represents a fingerprint of the ageing. Chapter 7 presents reactivity studies over the surface oxide, performed with both STM and LEEM. Chapter 8 gives a summary of the results and an outlook.

Chapter 2

Experimental techniques

In this chapter we illustrate the main experimental techniques which have been used throughout this thesis work. In the first section the basic principles of STM are described; secondly we present TDS. Finally we shortly introduce less extensively used techniques, as Low Energy Electron Diffraction (LEED), XPS and LEEM.

2.1 Scanning Tunneling Microscopy

The STM technique has been invented in the early '80s by G.Binnig and H.Rohrer, who were awarded the Nobel prize in 1986 [38–40].

The development of the STM has been a revolutionary step in surface science, and one of the first milestones for Nanoscience and Nanotechonology.

This technique allows imaging a surface with atomic resolution; moreover, thanks to continuous improvements, it is nowadays possible to exploit its capabilities for several different purposes. In fact an STM can be used to manipulate atoms, to follow chemical reactions on the atomic scale in real time, and also to gain information on the optical properties of a material [41–43]. Furthermore, with some *ad hoc* modifications, STM can operate in reactive gas ambient up to pressures of 1 atm [21, 33, 44] or even in liquids.

The main disadvantage of STM is the lack of chemical resolution, i.e. it does not allow to unambiguously identify a specific element or compound from a single image. Recently a new method has shown promising possibilities to overcome this problem, but up to now was applied only at low temperatures and for organic adlayers [45]. Therefore, STM data have in general to be integrated by other experimental or theoretical methods, such as XPS or density functional theory (DFT) to have a complete understanding of the phenomena under consideration.

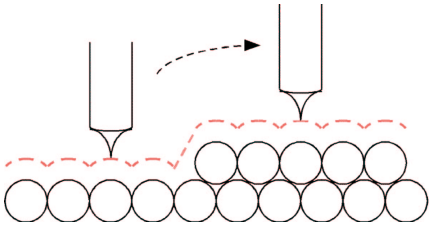

Figure 2.1: Tip scanning along a line across the sample in constant current mode [42].

2.1.1 Basic principles

STM measurements rely on the tunneling effect, which requires a quantum-mechanical description. When a conductive surface and a metallic tip are brought to distances of the order of a few ångstroms (Å) we have the formation of a narrow vacuum potential barrier between the electrodes. If an external bias voltage is applied between the two, electrons can *tunnel* across this barrier, giving rise to the *tunneling current*. This current is due to the extension of the wave functions of the electrodes into the vacuum and to their mutual overlap. Since it is strongly dependent on the tip-surface distance (varying by ~ 1 order of magnitude if the distance is changed by 1 Å), it is sensitive to very small variations of the surface topography. To form an image, the tip is scanned over an area of the surface in one of the two following operation modes:

constant height mode: the tip is kept at a constant vertical position during scanning, and the tunneling current is acquired at every scan point;

constant current mode: a feedback system is introduced to regulate the tip height so as to keep the tunneling current constant while scanning. What is recorded at each point is then the vertical displacement of the tip (z) as a function of the lateral (x, y) position.

The former mode allows higher scanning frequencies but there's no protection against tip crashes into surface bumps. Therefore the most commonly used is the constant current mode, which is also the one we used for this thesis work. As sketched in figure 2.1, while scanning along a line across the sample in constant current mode, the tip follows in a first approximation the profile of the surface. By iterating this operation line by line over the area of interest and then converting the vertical displacements of the tip into a suitable color-coding, an "image" of the surface is formed. A schematic drawing of an STM operating in constant current mode is shown in fig 2.2.

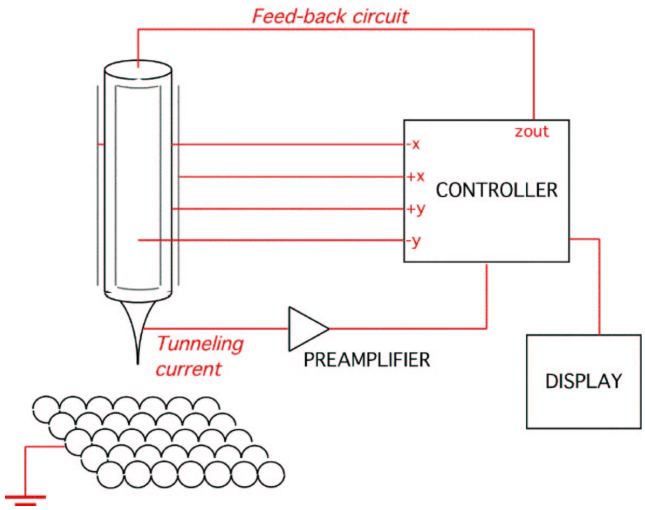

Figure 2.2: Schematic representation of an STM system operating in constant current mode [42].

2.1.2 Scanning Tunneling Microscopy theory

The tunneling current -and hence the image contrast- depends not only on the surface topography but also on the tip/sample electronic states available for the process. An extensive presentation can be found, e.g., in [46–48]; here we give just an overview of the theoretical basis of the tunneling theory.

In a simplified picture we can imagine electron tunneling across a 1D vacuum potential barrier between the tip and the sample, as shown in figure 2.3. If U is the height of the barrier and E is the energy of the electron which flows across it, we can write the time independent Schrödinger equation of the system as:

$$-\frac{\hbar^2}{2m}\frac{\mathrm{d}^2\psi(z)}{\mathrm{d}z^2} + V(z)\psi(z) = E\psi(z) \tag{2.1}$$

The general solution in the region $0 \leq z \leq d$ is:

$$\psi(z) = Ae^{-kz}$$

where

$$k = \sqrt{\frac{2m(U-E)}{\hbar^2}} \tag{2.2}$$

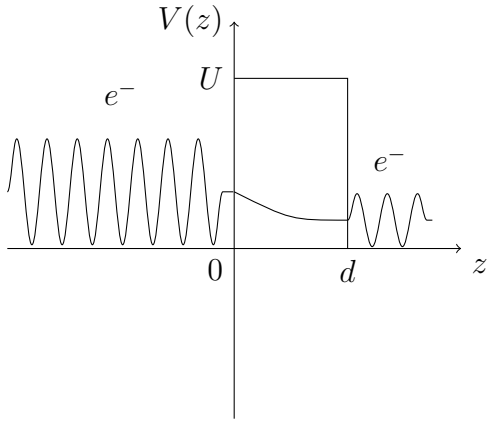

Figure 2.3: An electron impinging from the left on a one-dimensional potential barrier can cross the barrier even if $E < U$ provided the width d of the barrier is small enough [41].

Taking into account the continuity constraints on the wave function and its derivative, the solution in the region $0 \leq z \leq d$ becomes:

$$\psi(z) = \psi(0)e^{-kz}$$

If we assume the sample to be in the $z = 0$ plane and the tip to be positioned at $z = d$, the probability for an electron to tunnel from the sample ($z = 0$) to the tip ($z = d$) is:

$$w \propto |\psi(d)|^2 = |\psi(0)|^2 e^{-2kd} \tag{2.3}$$

Equation 2.3 reveals the exponential dependence of the tunneling probability on the tip-sample distance, that is responsible for the sub-ångstrom resolution of STM in the z direction (orthogonal to the sample surface) [48].

To get an approximate expression for the tunneling current, we will now take into account the energy levels involved in the tunneling process. When the tip and the sample are connected through a voltage supply, their Fermi energy E_F is the same, and in the $T \approx 0\,\mathrm{K}$ approximation, all and only the electronic states below E_F are occupied. When no bias voltage is applied between the two, there is no tunneling current since there are no available states for the electrons to tunnel into. By applying a negative bias voltage V to the sample with respect to the tip (figure 2.4 left), a tunneling current flows: an electron in a sample state ψ_n with energy E_n lying between E_F and $E_F + eV$ has a

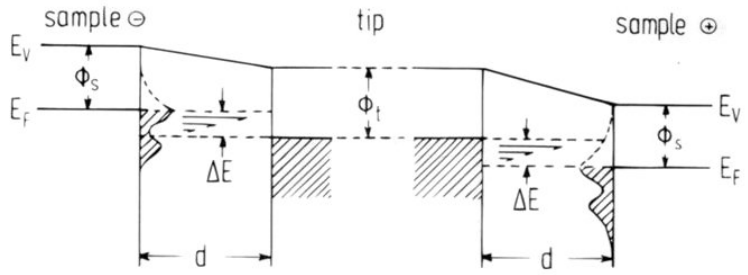

Figure 2.4: Tunneling from occupied sample states to tip empty states (negative sample bias, on the left) and from tip filled states to empty sample states (positive sample bias, on the right) [49].

chance to tunnel into an empty tip state. Vice versa, when a positive bias is applied to the sample, the electrons will tunnel from the tip filled states into the sample empty states.

The work function of the metal, ϕ, is defined as the energy threshold required to bring an electron from the bulk to the vacuum level[1]. Neglecting all temperature effects, we have $E_F = -\phi$; if we assume that the bias is much lower than the work function, $eV \ll \phi$, the energy of the electronic states involved in the tunneling process is $E_n \approx -\phi$. From equation 2.3, the probability w for an electron in the nth state ψ_n to tunnel into the tip is:

$$w \propto |\psi_n(0)|^2 \, e^{-2kd} \tag{2.4}$$

where

$$k = \sqrt{\frac{2m\phi}{\hbar^2}}$$

because from equation (2.2)

$$eV - E_F = eV + \phi \approx \phi$$

The tunneling current, within the given approximation, can be obtained by summing the contribution of all the electronic states with energy E_n in the

[1]From now on we assume it to be the same for sample and tip.

$(E_F \div E_F + eV)$ range.

$$I \propto \sum_{E_n=E_F-eV}^{E_F} |\psi_n(0)|^2 \, e^{-2kd} \tag{2.5}$$

If V is small enough, the sum in eq. 2.5 can be replaced by the local density of states (LDOS) at the Fermi level. The LDOS is the number of states per unit volume per unit energy at a given point in space and at a given energy: at a distance z from the sample, the LDOS at the energy E is defined as

$$\rho_S(z, E) \equiv \frac{1}{\varepsilon} \sum_{E_n=E-\varepsilon}^{E} |\psi_n(z)|^2 \tag{2.6}$$

if ε is small. By using this expression, the current can be re-written as [48]:

$$I \propto V \rho_S(0, E_F) e^{-2kd} \tag{2.7}$$

$$\approx V \rho_S(0, E_F) e^{-1.025\sqrt{\phi}d} \tag{2.8}$$

If we consider a typical metal work function $\phi \approx 4\,\mathrm{eV}$, we obtain a value of $\sim k = 1\,\mathrm{\AA}^{-1}$, i.e. the current decays by a factor $e^2 \approx 7.4$ when the distance changes by $\Delta d = 1\,\mathrm{\AA}$. Equation (2.8) has two important consequences: first of all, according to this model, an STM image is a contour of the LDOS of the sample surface at the Fermi level. Secondly, the tunneling current is extremely sensitive to very small differences in the tip–sample distance, and this property accounts for the atomic resolution of the STM [48].

In 1961, well before the invention of the STM, Bardeen [50] calculated the tunneling problem in the three dimensional case. Instead of solving the complicated Schrödinger equation for the entire metal–insulator–metal system, his approach was to treat the two electrodes as separate entities and then calculate their overlap. Bardeen determined the rate of electron transfer between the two states using the Fermi golden rule; if we assume that $k_B T$ is small enough[2], we obtain the following expression for the tunneling current [48]:

$$I = \frac{4\pi e}{\hbar} \int_0^{eV} \rho_S(E_F - eV + \epsilon) \rho_T(E_F + \epsilon) \, |M|^2 \, d\epsilon \tag{2.9}$$

The probability of tunneling from a state ψ, on one side of the barrier, to a

[2] to approximate the Fermi distribution with a step function

state χ on the other side [48] is given by the matrix element M :

$$M = \frac{\hbar}{2m} \int_{z=z_0} \left(\chi^* \frac{\partial \psi}{\partial z} - \psi \frac{\partial \chi^*}{\partial z} \right) dS$$

where $z = z_0$ is a separation surface lying entirely within the two electrodes.

Finally, if M is assumed to be almost constant within the range of interest, we obtain the tunneling current in a simplified form:

$$I \propto \int_0^{eV} \rho_S(E_F - eV + \epsilon) \rho_T(E_F + \epsilon) d\epsilon \tag{2.10}$$

From the equation above we see that the tunneling current, within Bardeen's extension of the one–dimensional tunneling problem, is not simply the LDOS of the sample at the Fermi level, but rather a convolution of the density of states (DOS) of both electrodes.

Later, Tersoff and Hamann [51, 52] extended Bardeen's description to the case of STM by considering the problem in the limits of $V \to 0$ and $T \to 0$, where the Fermi function exhibits a step like behaviour and only energy levels close to E_F contribute to the tunneling current. They obtained the following expression for the tunneling current:

$$I = \left(\frac{2\pi e^2}{\hbar} \right) V \sum_{ts} |M_{ts}|^2 \, \delta(E_s - E_F) \delta(E_t - E_F) \tag{2.11}$$

where E_t and E_s are the energies of the unperturbed wave functions of the tip and the sample, respectively. By considering the tip as an s wave function of radius R and the sample as a plane wave parallel to the surface plane, decaying exponentially outside the metal, they could calculate the M_{ts} matrix and found that

$$I \propto D_t(E_F) \cdot \sum_s |\psi_s(\vec{r}_0)|^2 \, \delta(E_s - E_F) \tag{2.12}$$

where D_t is the density of states per unit volume of the tip and $\vec{r}_0$ is the position of the tip's center of curvature. We can now define the quantity

$$\rho(\vec{r}_0, E_F) \equiv \sum_s |\psi_s(\vec{r}_0)|^2 \, \delta(E_s - E_F)$$

which is the LDOS of the sample at E_F at the position of the tip. Therefore

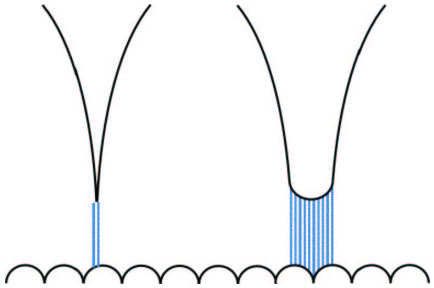

Figure 2.5: Tunneling process with a sharp and a blunt tip [42].

by substituting this expression in equation 2.12 we obtain:

$$I \propto D_t(E_F) \cdot \rho(\vec{r}_0, E_F) \tag{2.13}$$

Since the wave function of the sample along the tunneling junction (i.e. perpendicular to the surface, in the tip direction) has the expression $\psi_s(\vec{r}) \propto e^{-kr_\perp}$, its square modulus becomes:

$$|\psi_s(\vec{r_0})|^2 \propto e^{-2k(d+R)} \propto e^{-2kd} \tag{2.14}$$

where d is the tip–sample distance, measured from the tip apex. Therefore, if we insert this formula into the density of states and finally into the current (eq. 2.13), this detailed treatment of the tunneling problem leads again to the same kind of proportionality for the tunneling current: $I \propto e^{-2kd}$ (see equations 2.5 – 2.8).

2.1.3 Tip effects

As described in the previous paragraph, despite the fact that the most common approximation for the tunneling current (eq. 2.3) does not include any tip-dependent term, a more accurate description (eq. 2.10) points out that the tip is as important as the sample. In fact, a "good" tip is one of the key factors for obtaining reliable STM images.

The density of states ρ_T of a tip is mainly determined by its shape and chemical identity. Since the tunneling process involves the very most protruding atom(s) of the tip, the resolution that can be achieved strongly depends on the curvature at the tip apex. As sketched in figure 2.5, in the case of a blunt tip many atoms will contribute to the current, thus lowering the spatial resolution with respect to the case in which only one or a few atoms are participating. STM tips are usually made of tungsten (W) or more inert materials like Ag and

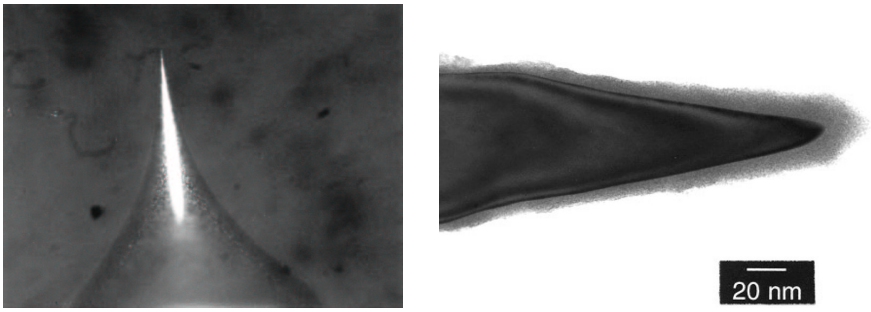

(a) photograph (b) TEM image

Figure 2.6: Large scale and small scale (TEM, [53]) images of an STM tip.

PtIr; we prepare our tips by electrochemical etching[3] of a 0.38 mm W wire. In this way we obtain tips like the one in figure 2.6a, with hyperbolic shaped edges and apparently a sharp termination. To better judge the quality of a tip, however, closer inspection is needed: the Transmission Electron Microscopy (TEM) permits to look at the tip apex on the nanometer scale. Anyway, all we can state about the tip in figure 2.6b is that it has good chances to reach atomic resolution. Due to the exponential dependence of the tunneling current on the distance, the achievable resolution is determined by the tip shape on a sub-nanometer scale, i.e. not visible even with a TEM. In other words, from figure 2.6b we can not distinguish if this tip is sharp or blunt at its very end (fig. 2.5). Nevertheless, even a tip as one with many single atom terminations can achieve atomic resolution, provided there is only one termination that is more protruding, i.e. that the other ones do not contribute significantly to the tunneling current. One of the most common problems to face is the so called "double" tip: when two terminations have the same height (within about 1 Å), every physical feature on the surface gets blurred or even duplicated in the STM image, because it is imaged sequentially by the two twin protruding tips.

The chemical identity of the outermost atoms at the tip apex is the second parameter determining the tip DOS. When scanning at high temperatures or during a chemical reaction, an atom can easily be picked up by the tip. The same can happen also when measuring on an adsorbate structure, if the adsorbed atoms are only weakly bond to the surface. In all these cases the tunneling current flows between the sample and the foreign atom: the interpretation of

[3]For the details of the process, see [42, 53].

STM images would then require to know the identity of the foreign atom and also to take into account the possible chemical interactions between the tip and the sample: for example oxygen, which is usually imaged as a depression, can be imaged as a protrusion if an O atom is picked up [54]. It is also possible to tailor the tip preparation to change at will the chemical identity of the tip apex: in this case STM can gain in both spatial and chemical resolution [45].

If the surface is covered by adsorbates, even when tip artifacts can be ruled out from the data analysis, the understanding of an STM image is not straightforward: in fact, the full electronic structure overall of the system must be considered. The interaction between an adsorbate and the surface can often lead to a change in the LDOS at the Fermi level; even if the involved orbitals are centered far away from the tunneling window, the DOS can still be influenced by their tails. Moreover, the metal electronic structure can be modified by the removal of surface states or by polarization effects. Therefore, as a general rule, STM images of adsorbates do not simply reveal the position of their ion cores.

As described in [55], it is possible to formulate qualitative predictions on image contrast in the case of adsorbates on metal surfaces by using the Tersoff and Hamann approximation. When an adsorbate polarizes the surface, a depression can be imaged in STM; Tilinin and coworkers proved that the depression is more pronounced when the adsorbate is more electronegative [56]. In the case of an oxygen atom [57], for example, there is a significant charge transfer from the metal to the O2p orbitals; since these states, however, are far below the Fermi level, they do not contribute to the tunneling current. The O3s state is also involved: the charge that is transfered to this level leads to an increase in the LDOS at the Fermi level, but at large distances from the surface [57]. Nevertheless, the main effect of oxygen adsorption, which has a strong influence on the tunneling, is the polarization of the metal surface, with the creation of a charge depletion area just below the O atom. This is the reason why in STM oxygen is usually imaged as a depression, while at large distances ($\geq 6\,\text{Å}$, where the O3s level contributes) it can appear as a protrusion.

2.2 Thermal Desorption Spectroscopy (TDS)

One of the oldest surface science methods to study the adsorption properties of molecules on a surface is to prepare the overlayer and subsequently anneal the whole system in a controlled way, while monitoring the desorbing species with a mass spectrometer. This technique is commonly referred to as Thermal Desorption Spectroscopy (TDS), or Temperature Programmed Desorption

(TPD) [1].

From the data analysis of a TDS experiment it is possible to obtain information on adsorption kinetics, as described in references [58–60]. If the pumping speed is infinitely high, re-adsorption may be ignored, and the relative rate of desorption $r(\theta)$ of a given species follows the Wigner-Polanyi equation:

$$r(\theta) = -\frac{d\theta}{dt} = \nu\ \theta^n\ e^{-(\frac{E_{des}}{RT})} \tag{2.15}$$

where E_{des} is the desorption activation energy, $R = 8.314\,\mathrm{JK^{-1}mol^{-1}}$ is the universal gas constant, T is the temperature, θ is the coverage (varying between 0 and 1), and ν is the pre-exponential frequency factor. The order of the desorption process is given by the exponent n:

- $n = 0$, zeroth-order desorption: occurs if the rate of desorption does not depend on the adsorption coverage; the peaks have a characteristic exponential leading edge and the temperature of the maximum of the desorption peak shifts towards higher values with increasing coverage
- $n = 1$, first-order desorption: the peaks have symmetric line shapes, and their temperature is independent of the initial coverage.
- $n = 2$, second-order desorption: is typical of dissociative adsorption; the peaks are symmetric, and the temperature of the maximum shifts to lower values when increasing the initial coverage.

For the Rh(110) surface oxide, as will be shown in section 4.3, the desorption mechanism is slightly more complicated than the ones presented above: it follows in fact autocatalytic kinetics, not governed by equation 2.15 but by

$$r(\theta) = -\frac{d\theta(tot)}{dt} = -\frac{d\theta(dp)}{dt}(1 - F) \tag{2.16}$$

$$F = \frac{\theta(tot) - \theta(dp)}{\theta(cp)_{crit} - \theta(dp)_{crit}} \tag{2.17}$$

where cp (complex phase) is the oxide, dp (diluted phase) is the $c(2\times8)$ oxygen adsorption structure [61], and F is the surface fraction of the complex phase. When the total oxygen coverage lowers to reach the coverage of the diluted phase, $F = 0$ and simple first order desorption (eq. 2.15) of the adsorption structure governs the kinetics [61, 62].

2.3 Low Energy Electron Diffraction (LEED)

The diffraction of low energy electrons from a crystal surface was first discovered in 1927 by Davisson and Germer [46, 63]. A low voltage V accelerates the electrons towards the sample surface, were they are scattered. If we consider an electron with a momentum p, its wave function will have the following de Broglie wavelenght λ [64]:

$$\lambda = \frac{h}{p} = \frac{h}{mv} = \frac{h}{\sqrt{2mE_{kin}}} = \frac{h}{\sqrt{2meV}} \tag{2.18}$$

where $h = 6.626 \times 10^{-34}$ Js is the Planck constant, $m = 9.11 \times 10^{-31}$ kg is the electron mass and $e = 1.6022 \times 10^{-19}$ C is the elementary charge. According to this equation, the typical LEED voltages, in the range $20 \div 200$ eV, correspond therefore to wave lenghts lower than 0.3 nm (i.e. of the order of interatomic distances in the crystalline sample lattice). Part of the electrons are hence elastically scattered, giving rise to interference (i.e. diffraction) patterns that are collected on a luminescent screen opposite to the sample. The electron energies involved in the LEED process have a second crucial property: as shown in figure 2.7, their inelastic mean free path[4] is minimum: this means that low energy electrons are probing only the *very topmost layers* of the sample surface.

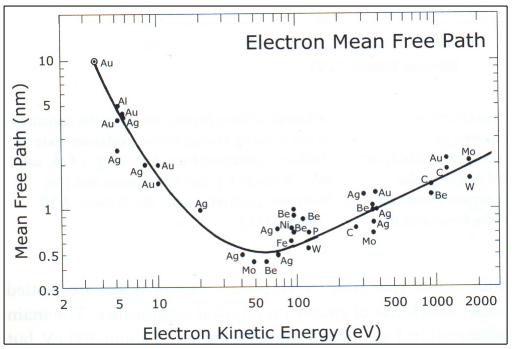

Figure 2.7: Inealstic mean free path of electrons in solids [1].

In routine sample cleaning and preparation procedures, LEED is used to check the surface ordering (by the sharpness of the diffraction spots and the background intensity), the lack or presence of adsorbates ad-structures, and to prepare phases with distinct LEED patterns.

[4]The mean distance that the particle can travel before being inelastically scattered in a host material and thus before loosing energy.

2.4 X-ray Photoelectron Spectroscopy (XPS)

XPS is one of the most widely used techniques in surface science (and catalysis): it probes the chemical composition and the oxidation state(s) of the atoms, thus being the crucial complement to measurements that lack chemical contrast like those by STM [1]. During this thesis work, we performed XPS experiments with two aims: to check the cleanliness of our sample, i.e. to see if there were unwanted contaminants, and to study the surface structure and composition. For these purposes, we have exploited the capabilities of a MgKα laboratory source and of the dedicated "SuperESCA" beamline at the Elettra Synchrotron, respectively.

XPS is based on the photoelectric effect [65], i.e the capability of photons to extract electrons from a bond state, that results in a detectable electrical current. An atom absorbs a photon with energy $h\nu$ so that a core or valence electron (hence named photoelectron) with binding energy BE is ejected with kinetic energy E_{kin}:

$$E_{kin} = h\nu - BE - \phi \tag{2.19}$$

where ϕ is the workfunction of the material.

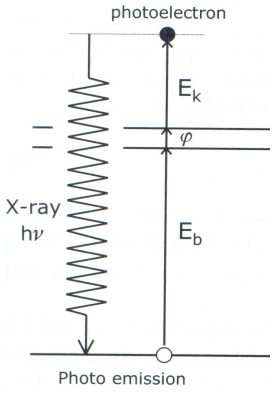

Figure 2.8: Sketch of the photoemission process [1].

Binding energies (BE) of electrons are unequivocally characteristic of the element from which the photoelectron originates, and so an XPS spectrum is a fingerprint of the system[5]. Moreover, BEs are not only element specific but

[5]Photoelectron peaks are labeled according to the quantum numbers of the level from which the electron originates, i.e. Rh3d, O1s, etc.

contain information on the atomic environment as well, because the energy levels of the core electrons depend slightly on the atomic coordination. Atoms in the first layer of the surface have a lower coordination number than bulk atoms, and this leads to a shift in the measured BE (called Surface Core Level Shift -SCLS). As another example, a change in the oxidation state also affects the BE of core levels (it increases with higher oxidation state); these shifts are tipically in the range $0 \div 3\,\text{eV}$. In chapter 4 we will present Rh3d and O1s spectra of the Rh surface oxide, in which we were able to distinguish components separated by a few 100 meV, each one corresponding to a specific atomic coordination [24, 66].

2.5 Low Energy Electron Microscopy (LEEM)

LEEM is an analytical surface science technique that enables real-time observations of dynamic processes at surfaces. Such phenomena include: phase transitions, adsorption, reaction, segregation, thin film growth, strain relief, sublimation [67].

It was invented by E.Bauer in 1962, but the first working instrument was developed in 1985 by Bauer and Telieps. As described in [68, 69], low energy electron microscopy uses diffracted electron beams to get a real-space image of the surface. The microscope is capable to monitor surface structure at nanometer scale in real time. The imaging is done with a series of electromagnetic lenses and properly chosen apertures.

2.5.1 LEEM setup

In figure 2.9 the basic setup of the LEEM instrument is shown. Electrons leaving the electron gun are accelerated to an energy of several keV. These high energy electrons fly upwards, and pass a set of lenses that keep the beam position and focus them onto the sample. After passing through the beam splitter, the electrons enter the sample chamber passing through the objective lens, being decelerated to low energy (by holding the sample at a potential close to the accelerating one). The low energy electrons are elastically backscattered at the sample surface, in the same way as in a LEED experiment. Due to the potential difference between sample surface and the objective, they are again accelerated on this path. The separator deflects the electrons back into the imaging column, where the projector lenses and the detector are located.

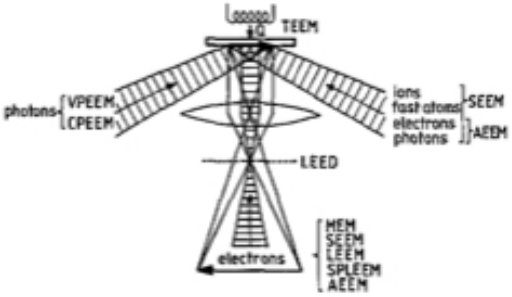

Figure 2.9: Schematic representation of a Low Energy Electron Microscope [70].

2.5.2 LEEM methods

When the low energy electrons are scattered from the sample surface, they produce a diffraction pattern; depending on the beam that is selected, the diffraction contrast method can be used on two different ways [71]:

Bright-field imaging If the specular (0,0) beam is used, "bright field" imaging is performed. In this case, the contrast is purely structural (*diffraction contrast*) and depends on the local differences in diffraction for the different surface phases present on the sample.

Dark-field imaging By selecting a secondary diffracted beam, a "dark field" image of the surface is produced. Here all areas that contribute to the formation of the selected beam appear bright.

In figure 2.10 we report a LEED image of the W(110) surface after depositing 0.5 ML of oxygen: two rotational domains are formed ((1×2) and (2×1)), and choosing the red and the green spot we obtain the two darkfield imaging showing opposite contrast.

Other methods available in LEEM are phase contrast and quantum size contrast [71, 73]. In the first, the height difference between terraces on the surface leads to a phase difference in the backscattered waves that can converted into an amplitude difference, allowing to image steps at surfaces. The second method is based on the interference of waves that are backscattered at the surface and at the interface of a thin film, producing maxima and minima in the backscattered intensity depending on the local thickness of the film. The three methods (diffraction, phase and quantum) are sketched in figure 2.11. Finally a LEEM instrument can be also used to image non-crystalline samples or to acquire LEED data from microscopic areas: these two methods are MEM and μ-LEED:

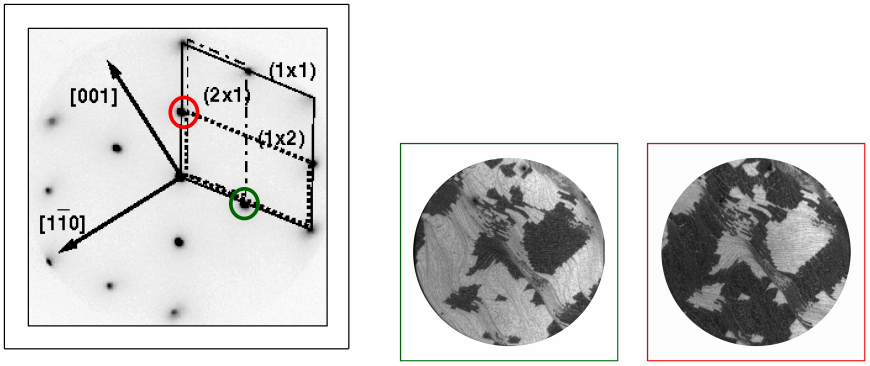

(a) LEED (b) darkfield using the green spot (c) darkfield using the red spot

Figure 2.10: LEED (28 eV) and LEEM darkfield images ($E = 9eV$, $fov = 10\,\mu m$) of the W(100) surface; the central and right images are acquired using the diffraction spot in green and red, respectively [72].

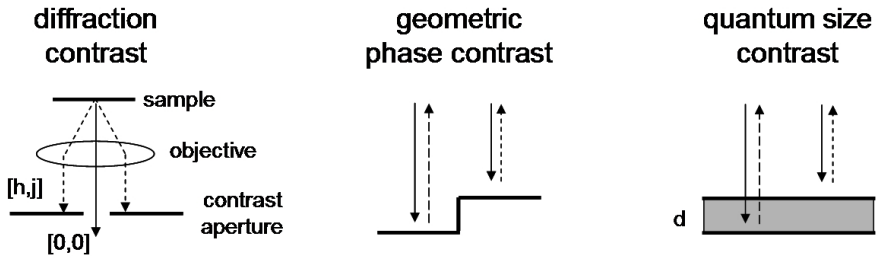

Figure 2.11: Contrast methods in LEEM.

MEM in mirror electron microscopy the surface is illuminated with electrons at very low energy: since the bias is tuned to minimize their interaction with the surface, the contrast is due to work function differences and topography variations;

μ-LEED in this case, the microscope is operated as a LEED, but the probe area can be restricter to $2\,\mu m$ either by inserting an aperture in the image plane in the input or exit side of the beam separator, respectively.

2.5.2.1 The SPELEEM microscope at Elettra

Our measurements have been performed with the SPELEEM microscope (Spectroscopic PhotoEmission and Low Energy Electron Microscope) at the Nanospectroscopy [71] beamline at the Elettra Synchrotron in Trieste ([74–76]). The SPELEEM combines into one single instrument a LEEM and an energy filtered X-ray photoemission electron microscope (XPEEM), therefore offering a unique combination of complementary imaging and diffraction methods. The high temporal and structural sensitivity of LEEM make it a useful complementary technique ([77, 78]), which helped us in understanding the morphology and the reactivity of the Rh(110) surface oxide. The oxides were grown in a separate UHV chamber, connected to the main chamber through a gate valve. However, the chemical reactions that will be presented in chapter 7 have been performed by dosing molecular hydrogen directly in the main chamber, while measuring. The best lateral resolution we could achieve in LEEM mode was $\sim 20\,\text{nm}$ at $30\,\text{eV}$.

Chapter 3

Experimental setup

In this chapter the VT-STM experimental chamber of the Surface Structure and Reactivity (SSR) group is described, together with the instrumentation used during this thesis; in particular, three different oxygen sources are presented.

3.1 The UHV system

Ultra-High-Vacuum (UHV, i.e. a base pressure below 1×10^{-9} mbar), is required for most surface science experiments. At a pressure of 1×10^{-10} mbar, in fact, a contaminant with sticking coefficient 1 and mass 28 needs about 10 000 sec (3 hrs) to form a complete overlayer on the Rh(110) surface. UHV is therefore needed, to slow down adsorption from the background atmosphere so that it becomes negligible on the time scale of the experiments. This is a prerequisite especially for reliable STM studies, since the microscope gives no straightforward information on chemical identity.

Our preparation and characterization system is equipped with a turbomolecular pump, an ion getter pump together with a Ti sublimation pump, so as to mantain a base pressure of $\sim 2 \times 10^{-10}$ mbar. When dosing oxygen at high pressures (chapter 5) we set up an additional differential pumping system, that allowed to make STM measurements right after oxides preparation, remaining in the 10^{-10} mbar pressure range.

3.1.1 The experimental chamber

Our experimental system consists of a main preparation chamber (on the left in figure 3.1a) and of a smaller chamber, housing the Scanning Tunneling Microscope (on the right in fig. 3.1a), connected through a gate valve. Figure 3.1b shows the back side of the system. The chamber contains:

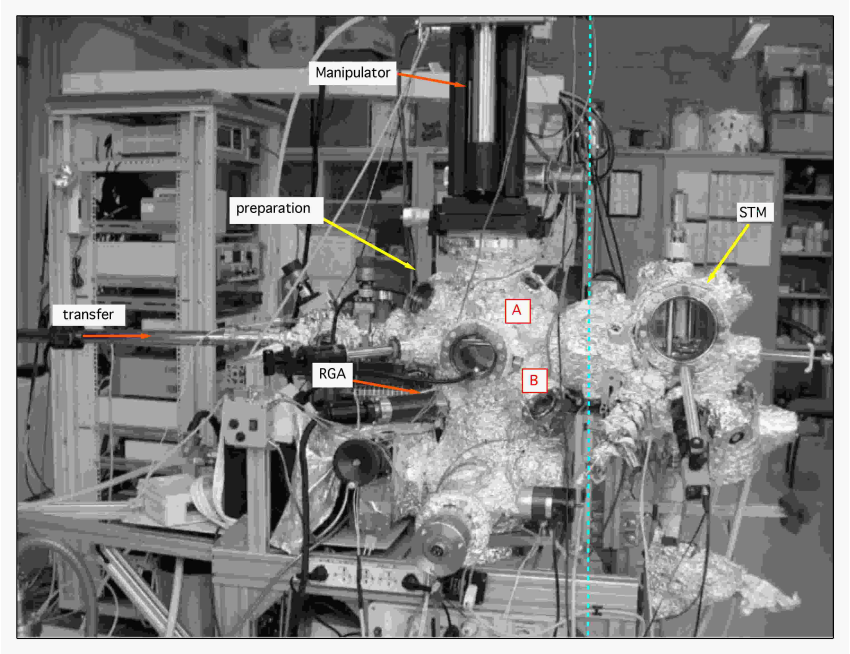

(a) front view

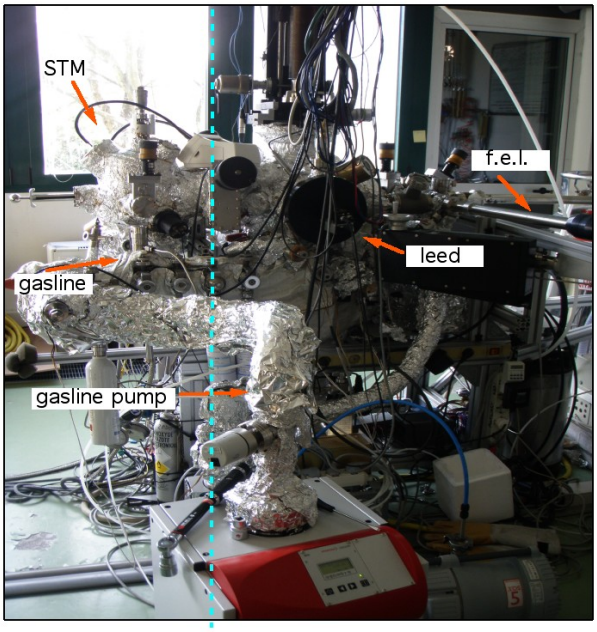

(b) back view

Figure 3.1: The experimental system located in the TASC laboratory, SSR group.

a **Fast Entry Lock system:** allows quick transfers of samples and tips from the air to the chamber and vice versa[1], without breaking the vacuum in the main chamber;

a **manipulator** in which the sample can be cooled down to 90 K by liquid nitrogen and heated up to 1300 K by means of a Pyrolytic Boron Nitride (PBN) heater integrated into the sample holder;

a **transfer rod** actuated by a magnet, that permits to go from the manipulator directly into the STM chamber and to the fast entry lock;

a **gasline** equipped with the most commonly used gases for surface science: O_2, H_2, CO, NO, H_2O;

a **doser**, which will be described in section 3.2.3;

a **hot filament ion gauge**;

a **sputter gun** for sample and tips cleaning with Ar^+ ions;

a **mass spectrometer** (SRS RGA 200) to monitor the composition of the background pressure and to acquire TPD spectra;

a **combined LEED/Auger system** for checking surface cleanliness and ordering.

3.1.2 The VT-STM

The microscope used in this thesis work is a Variable-Temperature STM (VT-STM) by Omicron, capable of working in the $130\,\mathrm{K} \div 800\,\mathrm{K}$ temperature range. This is a useful tool for studying systems that are conductive only at high temperatures, as well as to perform chemical reactions [42]. The minimum temperature is attained by filling a liquid N_2 cryostat and then pumping it down to freeze the nitrogen: a copper braid connects the cryostat to a cooling block that is put in contact with the sample holder. As on the manipulator, the heating is provided by the PBN in the sample holder. Since the electrical wires inside the STM are very thin, a maximum heating current of only 1.8 A can be applied, therefore limiting the maximum achievable temperature to lower values than on the manipulator. Recently our group developed a system to measure the temperature of the sample inside the STM through a K-type thermocouple directly spot-welded to the sample, as described in [42].

[1]The Fast Entry Lock is pumped by a turbomolecular pump with its prepumping stage; these pumps have to be switched off during STM measurements.

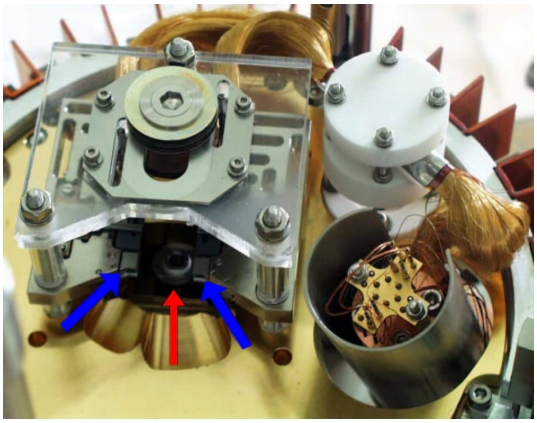

Figure 3.2: The VT-STM: the blue arrows point to the slits for the insertion of the sample holder, the red one indicates the piezo tube where the tip sits. In the upper left and right corners, the copper plates which are part of the eddy current damping system are visible.

Vibration isolation is a crucial issue for obtaining good STM images. While measuring, the whole microscope is suspended by four vertical springs that damp the high-frequency vibrations. In order to reduce low-frequency vibrations, the base platform (round plate in figure 3.2) is surrounded by copper plates that are centered between permanent magnets fixed on the chamber, leading to an additional eddy-current damping system. The sample is mounted in the STM with the surface pointing downwards, and the tip is approached from the bottom up.

In the latest years an add-on *FAST-STM* electronical module has been realized and tested within our group ([79, 80]). It permits to acquire movies with the commercial VT-STM at video rate, i.e. a factor of 1000 times faster than with the usual system.

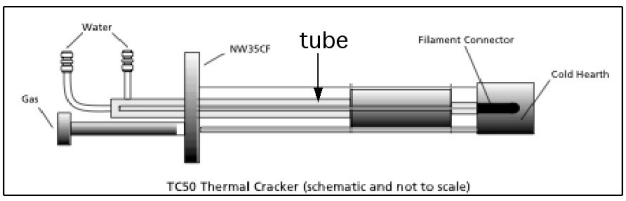

(a)

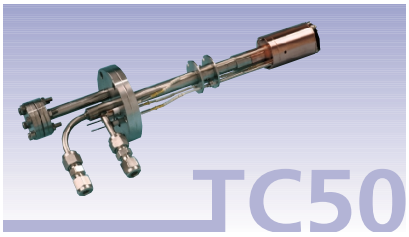

(b)

Figure 3.3: TC50 source: schematic drawing and photograph [81].

3.2 Oxygen sources

In this section the three oxygen sources used during this PhD work are described, namely a thermal cracker, a microwave plasma source and a molecular oxygen doser. At the time figure 3.1a was taken, neither the thermal cracker nor the plasma source were mounted; anyway, the flanges in which they have been inserted are indicated in the picture as A and B, respectively.

3.2.1 Thermal cracker

Right before the beginning of this doctoral thesis, the SSR group had decided to add an atomic oxygen source to their experimental equipment. The source had to be highly efficient in cracking even at low working pressures, to be UHV compatible: our choice had been the $TC50$ thermal gas cracker by Oxford Applied Research (OAR). This source combines excellent cracking efficiency with low working background pressures. As will be shown in section 5.1, we discovered that the source is easily attacked by oxygen, thus contaminating the sample by deposition of volatile oxides. A significant period of this doctoral thesis has been spent in trying to fix the source problems, partially in collaboration with the company, but up to now we could not setup a clean and working thermal cracker.

3.2.1.1 Working principle

Most of the available thermal crackers employ very hot ($\sim 2500\,^{\circ}\mathrm{C}$) tungsten filaments operated at high power ($\sim 4000\,\mathrm{W}$), thus causing an unwanted heat load on UHV systems. Moreover, this kind of cracker is of limited application since W is severely attacked by reactive gases like oxygen. The $TC50$ incorporates a fine-bore cracker *tube*[2], made of iridium, connected directly to the gas-inlet line. In this way gas load is confined and minimized, whilst providing a large surface area and long path length for high efficiency cracking. The catalytic nature of the cracker tube, heated by electron beam bombardment, significantly lowers the otherwise-high temperature and power necessary to achieve substantial ($> 70\%$) dissociation: in fact this percentage can be reached with $T < 1000\,^{\circ}\mathrm{C}$ at $60\,\mathrm{W}$. Direct water-cooling of the cracker body minimizes outgassing of the instrument. In figure 3.3 we show a sketch and a picture of the source.

3.2.1.2 Cracking efficiency

A simple procedure to evaluate the percentage of atomic oxygen in the beam, described in [82], is the "lost parent/precursor (LP)" method. When the "parent" species (O_2 in our case) is thermally dissociated in a vacuum chamber, the resultant atomic and radical species form other compounds (oxides in our case, especially CO_2 at chamber walls), and there is nearly no recombination to form the reconstituted "parent": thus the dissociated gas is permanently "lost". By acquiring a mass spectrum of the gas partial pressure before and after switching the cracker on, we obtain therefore a direct measurement of the dissociation efficiency (in figure 3.4 the oxygen curve is plotted).

3.2.1.3 Mounting and operating performances

The source was mounted on a $CF35$ flange on our UHV chamber, as shown in figures 3.5 and 3.1a. When inserted into the chamber, we could reach a minimum distance of $\sim 5\,\mathrm{cm}$ between the end of the catalytic capillary (tube) and the sample (fig. 3.5b); when switched on, the source illuminated the chamber (fig. 3.5c). Following the technical notes provided by the company [82], we measured with our mass spectrometer the drop in the $M32$ signal when switching the source on. From the two signals I_{32}^{off} and I_{32}^{on}, defined as the $M32$ values as detected by the Residual Gas Analyzer (RGA) with the source switched *off* and *on*, respectively, we then calculate the following relevant

[2] in [81] the tube is defined as *inert*, but we now know is not true at least for our working conditions.

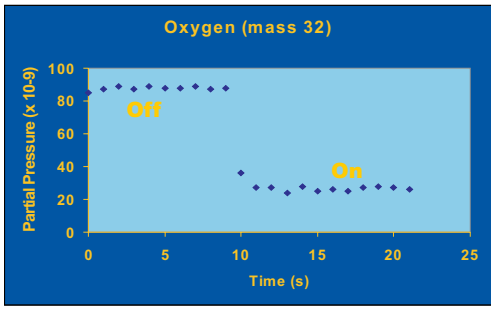

Figure 3.4: Parent loss method applied to oxygen: the cracking efficiency is derived from the drop of the $M32$ partial pressure when switching on the cracker [82].

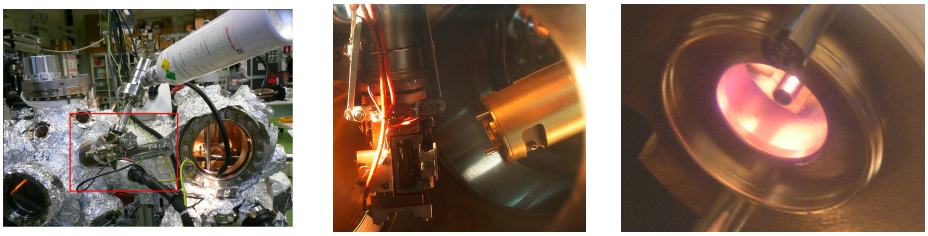

(a) (b) (c)

Figure 3.5: TC50 source: a) as mounted on our UHV chamber, with the O_2 bottle and leak valve visible; b) as inserted into the chamber, in front of the sample holder; c) the hot capillary illuminating the inside of the chamber.

quantities: the cracking efficiency

$$cracking = \frac{I_{32}^{off} - I_{32}^{on}}{I_{32}^{off}} \tag{3.1}$$

and the percentage of atomic oxygen in the (O_2, O_{at}) beam:

$$\%O_{at} = \frac{2 * (I_{32}^{off} - I_{32}^{on})}{2 * (I_{32}^{off} - I_{32}^{on}) + I_{32}^{on}} \times \frac{1}{100} \tag{3.2}$$

This last expression is the one that is used for estimating the effective doses on the sample. The best oxidizing conditions for preparing a trilayer surface oxide (i.e., a compromise between dosing time and pressure raise in the chamber)

were found to be 50 W power and $p_{O_2} = 1 \times 10^{-7}$ mbar. With these values we can estimate that $\sim 30\%$ of the beam impinging on the sample was composed by atomic oxygen.

3.2.1.4 Discovering contaminations

When analyzing with synchrotron radiation the oxides formed by atomic oxygen from the thermal cracker we found out that the surface was contaminated with Ir and Pt, both in oxidized and metallic form. The measurements have been performed at the *SuperESCA* beamline at the Elettra synchrotron in Trieste, that provided enough photon flux and energy resolution[3]. Platinum and iridium came from the $TC50$, because they were not present on a clean Rh crystal and their load was related to the amount of oxidation cycles made with the cracker. We detected a maximum Ir coverage of $\sim 1.5\%$ ML[4], while the Pt coverage was up to $\sim 7\%$ ML.

We assigned the iridium contamination to the catalytic cracking tube (figure 3.6), while the origin of the platinum contaminants was initially unclear. It turned out that it stemmed from a modification of the cracking tube that had been done by OAR in collaboration with us, in order to avoid the impingement of ions or electrons on the surface, generated by the electron bombardment that heats the capillary[5]. The shield covers the line of sight between heating filaments and cracker outlet, and had been built, against our explicit indications, out of platinum.

In conclusion, by synchrotron based XPS we discovered that the thermal cracker was not inert in oxygen ambient. In fact, we were able to extract volatile Ir oxide and Pt oxide even at relatively moderated O_2 pressure and using the source below its maximum power. This contamination becomes relevant for strong oxidation experiments as in this work, since we did not sputter the surface during our oxidation cycles.

[3]The flux is $\sim 10 \times 10^{+11}$ photon/s at 400 eV, and at this same energy the energy resolution is $\sim 10 \times 10^{+4}$. On the contrary, with a laboratory XPS source the cross sections for Pt and Ir would have been one order of magnitude lower, therefore making hard to detect a few percent of these contaminants.

[4]One Monolayer (ML) corresponds to the number of Rh atoms on the Rh(110)-(1×1) surface, $9.8 \times 10^{+14}$ atoms/cm^2.

[5]Also with the shield mounted, the amount of charged species reaching the sample was never zero, but was minimum (~ 5 nAsec) for the operation conditions chosen.

Figure 3.6: Inner part of the TC50: the Ir cracking tube with the Pt circular shield.

3.2.1.5 Tentative modifications

We tried to minimize contaminations by remounting the first cracking capillary, i.e. the one without the platinum shield, as shown in figure 3.7a. In collaboration with OAR we assembled and tested a quartz frit (fig. 3.7b) to be mounted on the outermost part of the source head: this window was intended to block any metallic particle coming from the capillary area, while letting gases pass through it.

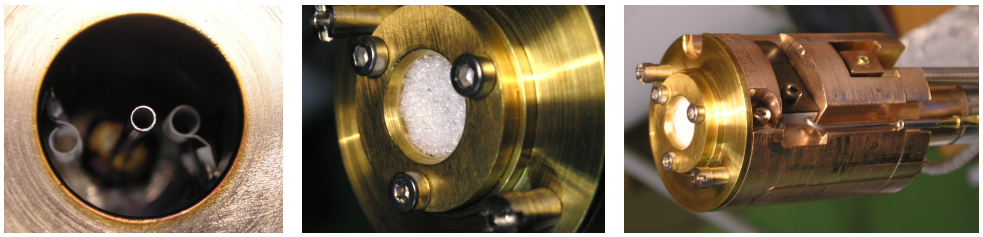

(a) (b) (c)

Figure 3.7: a)TC50 original cracking tube, surrounded by the two filaments; b) quartz frit window; c) source assembled with the described modifications.

The resulting setup of the $TC50$ is shown in figure 3.7c; unfortunately this assembly was not successful: both filaments got burned after only a few minutes of operation, due to higher effective oxygen pressures in the cracker. Moreover, we could never reproduce a relevant cracking efficiency as in the the previous mountings.

3.2.2 Micro Wave Plasma source

The second source of atomic oxygen source that we have used was a commercial TECTRA plasma source ([83]). The Tectra Plasma Source is a multi-purpose source which can be easily configured to produce either atoms or ions: we used it in the Atom mode[6]. A plasma is created in a coaxial waveguide by evanescent wave coupling of microwave energy at $\nu = 2.45\,\mathrm{GHz}$. The plasma is further enhanced by Electron Cyclotron Resonance (ECR)[7].

To estimate the cracking efficiency of the Plasma source, we tried to apply the "lost parent/precursor (LP)" method described in 3.2.1.2. Despite the values specified in [83] ($\sim 30\%$ of O_{at} in the beam), we measured a drop in the $M32$ signal corresponding to a percentage of atomic oxygen in our beam of only $\sim 6\%$, while the CO and CO_2 signals increased significantly (from 5% to 20% of the total pressure). Such a low cracking efficiency could be related to the source geometry -due to the partial recombination of O atoms on the chamber walls- or due to pumping rate effects that lead to a $M32$ signal at the RGA that does not reflect the $M32$ content in the beam. With respect to the thermal cracker, the plasma source was positioned twice as far from the sample ($\geq 10\,\mathrm{cm}$) and more retracted from the RGA: indeed, the dosing pressure had to be increased at least to cover the surface with an oxide layer.

3.2.3 Molecular oxgen doser

As a complementary method for oxide preparation, we finally used molecular oxygen instead of atomic one, also with the aim to obtain surfaces free of contaminants, i.e. composed only by rhodium and oxygen. A doser had been set up for working with reactive gases such as H_2O or NH_3, to minimize the effect of dosing on the background pressure [42]. In fact, in this way the partial pressure in front of the sample can be increased locally, thus reducing the dosing time and avoiding any significant worsening of the background pressure. The doser is composed of a thin tube, connected to the gas-line by a valve; at the end of the tube there is a microchannel plate. It can be inserted into the preparation chamber so as to reach distances of $< 5\,\mathrm{mm}$ from the sample surface (see figure 3.8).

[6] In this mode, a specially designed aperture plate (in molibdenum) should inhibit ions to escape from the plasma, yet allowing reactive neutral species to come out. However, the fraction of charged particles is not reduced to zero: we registered residual currents in the order of some nA (nanoampere) when dosing. A further addition of an ion-trap option is needed to completely remove the residual ion content.

[7] The cyclotron motion has two main positive effects on the plasma density: increasing the electron energy and thus increasing the ionization probability, and reducing electron diffusion to the walls and thus reducing electrons loss.

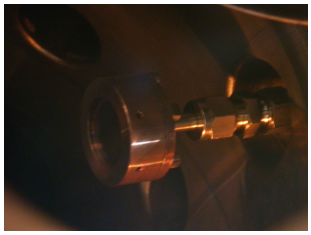

(a) doser

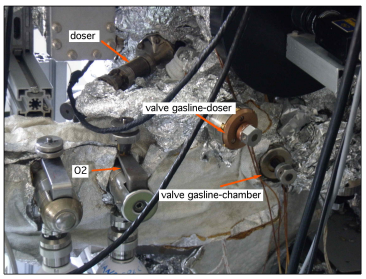

(b) gasline, doser and connection valves

Figure 3.8: a) The doser inserted the UHV chamber. b) View from the outside of the chamber: the valves connecting doser, gasline and chamber are outlined, together with the O_2 leak valve.

In order to perform the oxygen exposure, the procedure is as follows: the valve that connects the gasline and the chamber (fig. 3.8b) is kept closed while the gasline is filled with high pressure of the gas (in our case, $p_{O_2} \leq 1 \times 10^{-2}$ mbar). At this point the valve connecting the doser and the gasline is opened and the gas flows through the channel plate straight to the sample. When the exposure is terminated the doser valve is closed and the gasline is separately evacuated (and eventually baked). As shown in fig. 3.1b, for the oxide preparation we added a pumping system directly to the gasline: in this way we were able to evacuate the gasline faster[8]. Thanks to this experimental setup, the pressure in the chamber raised *only* up to $p_{bkg} \sim 1 \times 10^{-5}$ mbar while dosing oxygen.

To get an indication of the real dose seen by the sample, we performed a calibration using the $c(2 \times 8)$ O/Rh(110) adsorption structure [84]. We know that this structure has a well defined O coverage of 0.75 ML, and we usually form it by dosing 5 min with $p_{O_2} = 5 \times 10^{-8}$ mbar (i.e.$\sim$ 11 L). When using the doser, the pressure in the chamber increased by 5×10^{-9} mbar; with this value we were able to form the $c(2 \times 8)$ in only 2.5 min. From this result we can estimate that the effective pressure at the sample was nearly 20 times higher than in the background. Working at much higher oxygen pressures, the flow through the microchannels is no longer molecular. As a consequence, the scaling factor for the pressure at the sample might be lower.

[8]Sometimes we needed to prepare the sample more than once a day, thus needing to quickly re-open the valve connecting the gasline and the chamber; without the extra pumping we would have had to wait many hours before opening the gasline towards the chamber.

Chapter 4

The Rh(110) trilayer surface oxide.

We have already introduced in chapter 1 the importance of studying the surface oxides of catalytic model systems, as active phases in oxidation reactions, precursor states for bulk oxides formation and as layers covering Rh nanoparticles [24, 33**?**]. Our interest in highly oxidized phases of Rh(110) is based on an extensive investigation program of the oxygen adsorption phases on this surface [61, 84, 85]. In addition, we wanted to contribute to delineate a picture of the surface oxides grown on low-Miller-index Rh surface, completing the existing knowledge about Rh(111) and Rh(100) and highlighting common features and differences [23, 86, 87].

After a short presentation of the two similar rhodium surface oxides that have previously been studied, we discuss the Rh(110) trilayer surface oxide structure, and we describe the surfaces as formed with atomic and molecular oxygen. Finally we analyze the TDS spectrum of such an oxide, that can be explained by an autocatalytic desorption mechanism. The reactivity of the trilayer, on the other hand, will be presented in chapter 7.

4.1 Surface oxides on low-index Rh surfaces

Gustafson *et al.* have studied the structures obtained on Rh(100) and Rh(111) by dosing molecular oxygen at pressures from $\sim 1 \times 10^{-10}$ mbar up to 0.5 bar, in a wide temperature range and with a combination of several experimental and theoretical techniques. On the Rh(111) surface, as described in [23], at $p_{O_2} = 2 \times 10^{-4}$ mbar and a sample temperature of 800 K, a surface oxide starts to grow from steps. By comparison of STM, XPS and Density Functional

Theory (DFT) data it was possible to infer that this phase is a O-Rh-O trilayer, and that the lattice can be described as an (8×8) hexagonal Rh oxide on a (9×9) Rh(111) unit cell. A ball model of this structure, together with a simulated STM image, is displayed in fig. 4.1a. DFT calculations suggested that the trilayer is only *kinetically* stabilized[1], and remarkably, DFT calculation predicted the thicker oxides to be formed by stacking of several trilayers.

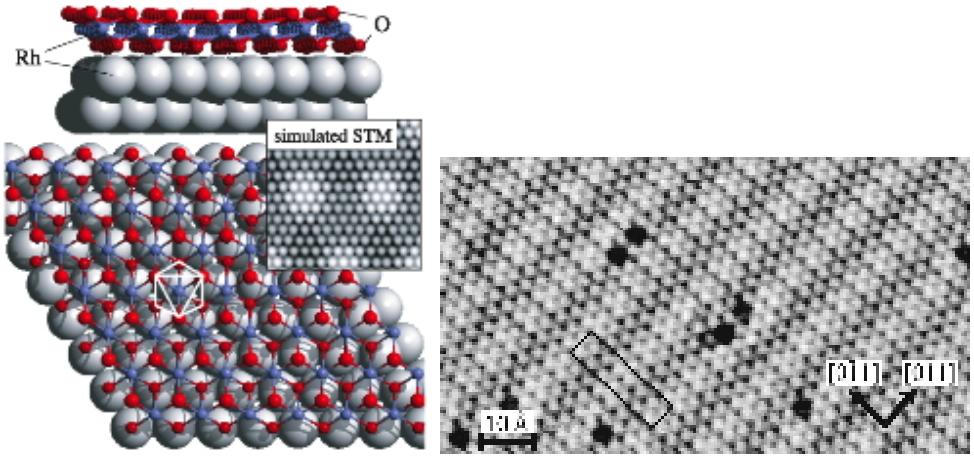

(a) (b)

Figure 4.1: a) Side and top view of the Rh(111) surface oxide; the inset shows the STM simulation using the Tersoff-Hamann approach (filled states between $-0.6\,\mathrm{V}$ and $0\,\mathrm{V}$. b) STM image of the $c(8 \times 2)$ structure formed by dosing for 600 sec at 700 K in $p_{O_2} = 1 \times 10^{-5}$ mbar; $V_B = -0.11\,\mathrm{V}$, $I = 1\,\mathrm{nA}$ [23, 86].

Similar results have been obtained, on the Rh(100) surface, by Gustafson and co-workers. In fact, despite the squared atomic arrangement of the substrate, the trilayer grows in a close-to-hexagonal structure: the ball model is very similar to the one proposed for the Rh(111) surface oxide.

In figure 4.1b we show an STM image of the trilayer formed on Rh(100); a part from the hexagonal pattern, we can distinguish an intensity modulation along the $[0\bar{1}1]$ direction: this is due to the periodic matching of the trilayer structure with the squared substrate one. As we will show in the next section, an analogous undulation is present also on our oxide.

[1] contrary to the Rh(100) and the Pd_5O_4/Pd(111) cases where the adlayers are *thermodinamically* stable for intermediate oxygen potentials [86, 87].

4.2 The Rh(110) trilayer surface oxide

The atomic structure of the Rh(110) surface oxide had already been resolved in previous studies; however, we were able to investigate the trilayer's properties more deeply, thanks to the different recipes tested in this work and to complementary techniques such as LEEM.

In ref. [66], a surface oxide was grown in UHV at $\sim 520\,\mathrm{K}$ using atomic oxygen[2], keeping the pressure in the chamber in the $10^{-6}\,\mathrm{mbar}$ range. The same surface oxide was prepared with molecular oxygen (in a separate chamber), requiring pressures above $10^{-4}\,\mathrm{mbar}$ and higher temperatures. The oxide was studied with several surface science techniques[3] that were complemented by extensive DFT calculations, thus providing enough information for an atomic level understanding of the surface structure.

It has to be remarked, however, that all the oxides prepared in these ways coexisted with adsorption structures (see also chapter 7): therefore the first attempt of this thesis work has been to improve the recipe in a way to form complete surface oxides covering 100% of the surface.

Figure 4.2 summarizes the theoretical and experimental results available for the Rh(110) surface oxide. DFT calculations [24] indicated that the oxide is thermodinamically only metastable and therefore it is probably stabilized by kinetic effects, as happens on the (111) surface. From the LEED measurements a $c(2 \times 4)$ coincidence periodicity for the oxide is derived, with respect to the underlying (110) substrate: the Rh reciprocal unit cell is indicated by the solid line while the oxide one is enclosed by the dashed line. This periodicity corresponds to the quasihexagonal[4] structure of a trilayer surface oxide whose structural model is displayed in fig. 4.2b; it is composed of two oxygen layers separated by a Rh layer, and the atoms are arranged with an ABC stacking. The trilayer unit constant was estimated from LEED to be $3.04\,\text{Å}$, and the DFT calculated one for a free standing trilayer was close to this value: $\sim 3.12\,\text{Å}$.

The quasihexagonal structure of the surface oxide was confirmed by both simulated and experimental STM images, displayed in fig. 4.2b: in the left and right part, empty and filled electronic states are imaged, respectively. The agreement between the theoretical and the experimental data is good: oxygen atoms are imaged as bright protrusions, as in the Rh(111) and (100) oxides cases. The periodic brightness modulation along the $[1\bar{1}0]$ rows is analogous to

[2]Provided by the TECTRA plasma source, described in 3.2.

[3]Namely LEED, STM, XPS and Scanning PhotoEmission Microscopy (SPEM).

[4]The hexagon is compressed along the [001] direction, therefore allowing the oxide to be commensurate with the substrate: in fact, in this direction 5 $c(2 \times 4)$ lattice constants are included in 4 Rh ones.

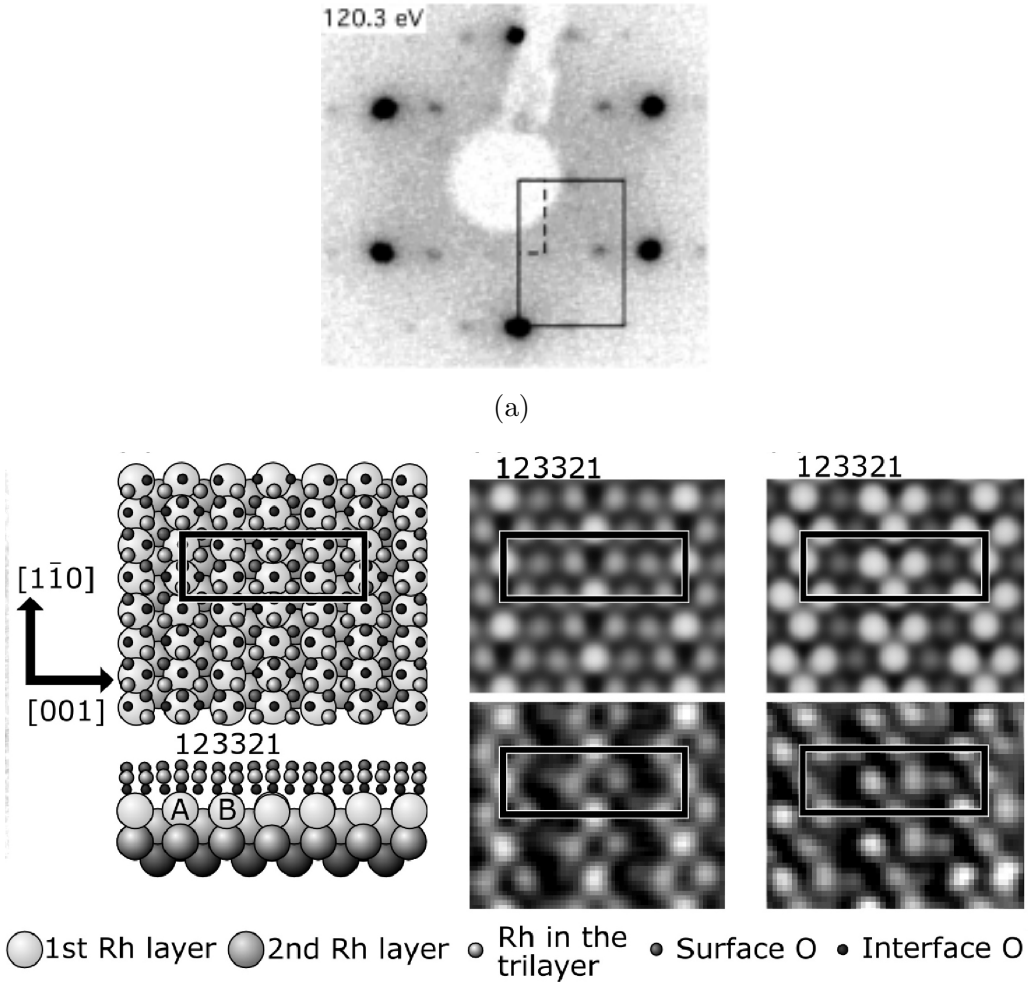

Figure 4.2: a) LEED pattern of the $c(2\times4)$ phase; b) structural model of the $c(2 \times 4)$ phase; simulated (top) and measured (bottom) STM images, $(2.2 \times 1.9\,)nm^2$ of the surface oxide. On the left: empty states topograph for states up to 0.6 eV above the Fermi level; on the right: from -0.2 eV to 0 eV below the Fermi level. The black rectangles mark the unit cell.

what observed on Rh(100): the oxygen atoms at the interface that sit on top of the rhodium ridge atoms (labeled as "1" and "A" in fig. 4.2b, respectively) give rise to an enhanced intensity in the STM images.

The structural model was supported by the STM image in figure 4.3a: in fact, theory predicted two equivalent rotational domains on the oxide, which can indeed be distinguished on the two sides of the picture. The unit cells are shifted in the $[1\bar{1}0]$ direction by $\sim 25\%$, as shown also in the structural model in fig 4.3b, and the domain on the right can be explained by a $180\,^\circ$ rotation of the domain on the left around the axis orthogonal to the surface, intersecting the position of a substrate Rh atom[5].

In previous studies the atomic scale structure of the rotational domains was already unraveled; during this thesis work, however, we were able to gain unprecedented insight in the domains size and distribution, thanks to the LEEM technique: these measurements will be presented in chapter 7.2.

The surface oxide $c(2 \times 4)$ structure was supported also by XPS data, summarized in figure 4.4 [24, 66]. From the peak integrals it was possible to establish that the rhodium layer in the oxide has a higher atomic density with respect to the clean Rh(110) layers: in fact, it contains 1.25 ML of rhodium. Each of the two oxygen layers has the same number of atoms, therefore the amount of oxygen contained in the trilayer was found to be 2.5 ML.

In the Rh3d5/2 spectrum of a clean (1×1) surface a bulk and a surface component can be distinguished; the trilayer's curve shows two new components, shifted by -0.20 eV and $+0.85$ eV with respect to the bulk one, that are assigned to the oxide and the interface Rh atoms, respectively. The oxide related core levels have almost the same binding energies as those measured for the oxide grown on Rh(100) and (111), both for the Rh3d5/2 and for the O1s levels.

In the O1s spectrum, two components were resolved: one related to the outermost oxygen layer, and another one due to the oxygen at the interface between the Rh crystal and the trilayer. Since there are three non-equivalent oxygen sites in the oxide, theoretically we would expect each component to be splitted into three contributes. Anyway, due to the extreme proximity of the oxygen sites (and therefore of their binding energies), the only detectable feature was the average separation (~ 1.1 eV) between the two major components.

[5]The calculated shift, according to the model, of the unit cell along $[1\bar{1}0]$ should be 30.6%, thus larger than the measured one. The simulated STM images explain this difference as due to the fact that the bright spots originating from surface oxygen atoms are slightly off center.

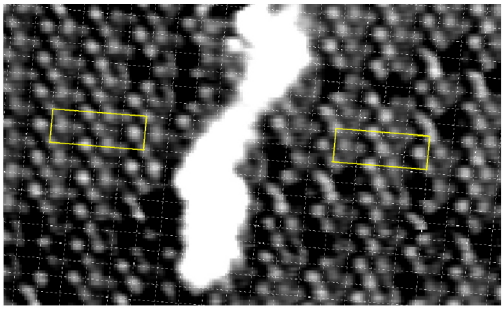

(a)

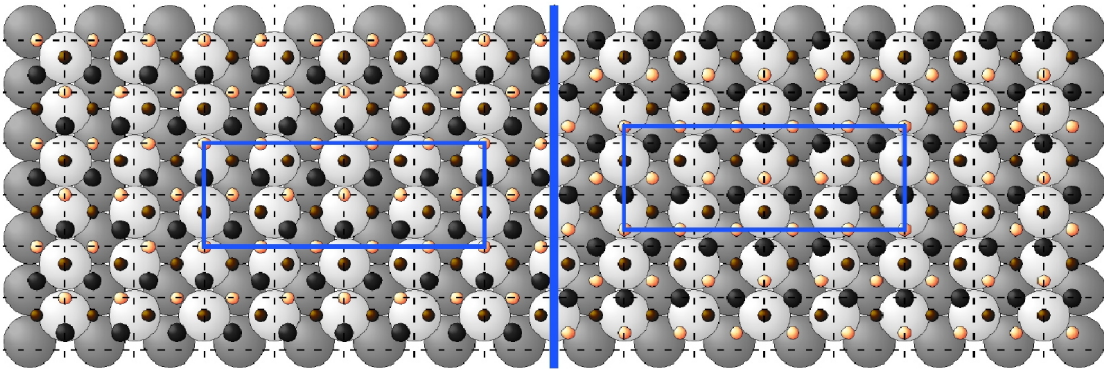

(b)

Figure 4.3: a) STM image showing the two oxide domains, with $c(2\times4)$ unit cells highlighted; $(9.7\times5.2)nm^2$, $V_B = -0.1\,\mathrm{V}$, $I = 1\,\mathrm{nA}$. b) Structural model where the domain on the right is rotated by 180 °. Large spheres: bulk Rh atoms; medium dark ones: trilayer Rh atoms; yellow and purple small spheres stand for oxygen atoms in the topmost and interface layers, respectively. [24].

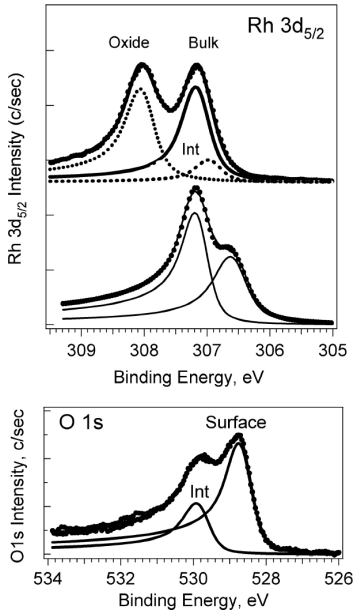

Figure 4.4: Deconvoluted Rh3d5/2 spectra of the surface oxide (top), of a clean Rh(110) surface (middle) and O1*s* spectrum of the surface oxide (bottom) [24].

During this PhD thesis, we performed a series of XPS measurements at the SuperESCA beamline at the Elettra synchrotron in Trieste[6]. Thanks to this experimental setup, we could acquire high-resolution spectra of our oxides. In figure 4.5 we plot an O1*s* spectrum of an oxide: the surface component (i.e. the one stemming from the atoms in the topmost layer) is highlighted in blue, while the remaining two are both assigned to interface atoms because of their shift with respect to the surface component[7]. The capability of resolving more than one interface component allowed us to confirm the trilayer model exposed above; moreover, it turned out to be useful in monitoring of the ageing process: as discussed in chapter 5.4.1, the green component was observed to increase as long as we proceeded with the oxidation cycles.

In this thesis work, we studied the oxides evolution upon the cyclic procedures described in 5.2. For this purpose, we used three different oxygen sources (chap. 3.2), and we started from the analysis of the different morphologies of

[6]See chapter 5.1

[7]The green component is shifted by $\sim 0.55\,\text{eV}$ with respect to the surface one, while the orange component is shifted by $\sim 1.15\,\text{eV}$. DFT calculations predicted a splitting between 0.3 and 1.1 eV between the surface and interface components [23, 24, 86]; therefore both the green and the orange belong to interface atoms.

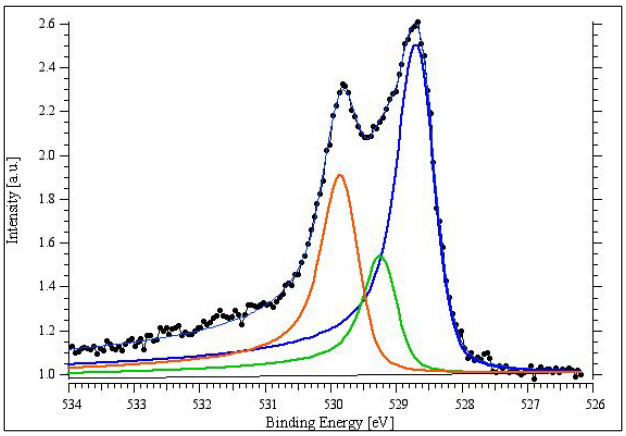

Figure 4.5: O1s spectrum of a first oxide acquired at the SuperESCA beamline: the blue curve correspond to the surface component, the orange and green ones originate from the interface oxygen atoms [24].

the first oxides[8] prepared with the three O sources. Before presenting the single cases, however, we describe two common features that have been found over *all* the oxides: the "strain" lines and the oxygen vacancies network.

4.2.1 Strain effects

The oxides prepared in previous works always coexisted with several oxygen adsorption structures; to better study the surface oxide phase, the first milestone of this PhD thesis has been the preparation of complete oxides, saturating all the surface.

Such oxides (see sec. 4.2.3) were characterized by large terraces -up to $(500 \times 500)nm^2$-, over which we could distinguish a series of lines, roughly aligned along the $[1\bar{1}0]$ direction, that appeared darker than the oxide terrace[9]. In figure 4.6 we show three images over large, medium and small areas; fig. 4.6b was obtained by filtering fig. 4.6a to enhance the appearance of these lines. They have an average separation of $\sim 5 \div 10$ nm and are influenced by surface defects like holes, into which they "enter": they resemble electromagnetic field lines running between electrodes. This observation suggested that these lines

[8] With *first* oxide we intend the trilayer formed on a pristine surface, that is the starting point for any oxidation cycle.

[9] Their visibility depended on the tunneling parameters but on top of all on the overall images resolution.

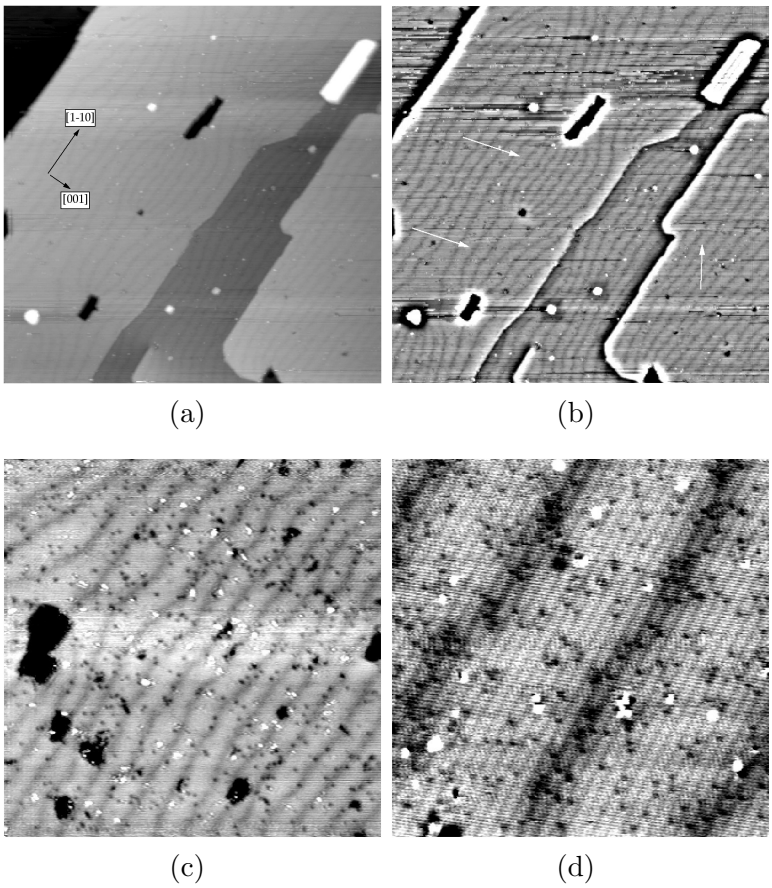

Figure 4.6: a)-b) $(250 \times 250)nm^2$, $V_B = 0.3\,\mathrm{V}$, $I = 0.6\,\mathrm{nA}$; the image on the right has been filtered to enhance the darker lines, and the white arrows indicate a few of them. c) $(100 \times 100)nm^2$, $V_B = 0.3\,\mathrm{V}$, $I = 0.4\,\mathrm{nA}$; d) $(25 \times 25)nm^2$, $V_B = 0.5\,\mathrm{V}$, $I = 1.6\,\mathrm{nA}$

could be due to strain, i.e. that the darker appearance could be a convolution of topographic and electronic effects in a region were strain is released. Some other considerations support this hypothesis:

- along these lines we always observed a higher concentration of oxygen vacancies with respect to the areas between the lines (fig. 4.6d);
- in the darker areas, the brightness modulation due to periodic matching of the trilayer with the Rh substrate (fig. 4.2b) is slightly reduced.
- Finally, the oxide lattice constant as determined from LEED was not exactly the same as the one calculated for a free-standing trilayer. As an example, 9.6 nm along the [001] direction contain 25 Rh lattice constants (3.8 Å) and ~ 31.2 oxide lattice constants, if we consider the experimentally determined 3.04 Å value. On the other hand, in this same distance we can arrange ~ 30.4 oxide lattice constants, if we consider the calculated 3.12 Å value for a free-standing trilayer. Therefore we can imagine the strain lines as created by the balance between the substrate constraints and the oxide tendency to assume its free-standing structure.

The strain hypothesis is confirmed also by the images presented in [66] (see also chapter 7), in which no darker lines patterns were observed. Since in this case the oxide terraces width never exceeded a few tens of nanometers, and the oxide was surrounded by adsorption structures, it is likely that the strain was released at these phase boundaries.

4.2.2 Oxygen vacancies

The most common defect of a surface oxide is a missing oxygen atom, i.e. an oxygen vacancy. An oxygen vacancy can be a favorable site for gas molecules dissociation and/or adsorption, therefore playing a crucial role in oxide-based catalysis [88–90].

On the Rh(110) surface oxide there are three different oxygen sites in both the outermost and the interface oxygen layers, labeled from 1 to 3 in figure 4.2b. Therefore we would expect three possible sites for oxygen vacancies: at low vacancies density, in fact, the dark features in fig. 4.7 can be identified with the three kind of vacancies [79].
When the density of vacancies increases, they are found to self-organize into a $c(2 \times 4)$ network, with the same lattice constant of the surface oxide [66]. The formation of such a structure was first observed as a precursor stage in the oxide titration with H_2 (see chapter 7); the same happened when CO was used as a reducing agent, and also when an oxide was left in UHV for several hours

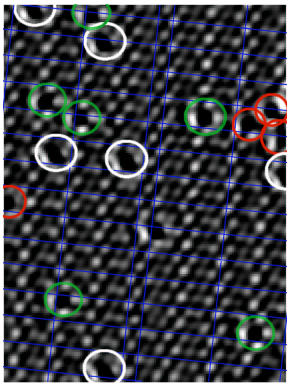

Figure 4.7: Empty states image of the surface oxide with the three possible kind of oxygen vacancies in the topmost layer: green circles correspond to atoms "1" missing, orange to atoms "2" and white to atoms "3" in figure 4.2b. In the middle of the image a mismatch defect (one extra atomic row) is visible; $(5.8 \times 7.8)nm^2$,$V_B = -0.6\,\mathrm{V}$, $I = 0.4\,\mathrm{nA}$ [79].

(see section 4.4). Moreover, this network was present over some areas of the surface after partial desorption of the trilayer (see chapter 5.4.3). In figure 4.8a we present a $(20 \times 15)nm^2$ area of the surface oxide, almost completely covered with the oxygen vacancies network: the defects are aligned along the $[1\bar{1}0]$ direction, and arranged in a $c(2 \times 4)$ structure. At room temperature, moreover, only one possibility for vacancy hopping was observed: from fig. 4.8b to 4.8c one dark hole jumps out of the $c(2 \times 4)$ network, moving to a neighboring site. In these two images we can also distinguish that the O atoms on the right-hand side of the vacancies have a slightly higher intensity; this helped us in recognizing them as the atoms in position "1" of the trilayer structure (fig. 4.2b). Therefore all the vacancies in the three central rows of these images[10] correspond to missing atoms of kind "2" . The only two possible configurations that we found for the vacancies network are built by removal of atoms "2" , on the right or on the left of the atoms "1": a confirming example is the fact that the vacancy that jumped away from the network in fig. 4.8b has moved from a site "2" into another site "2". In figure 4.8d we enclosed atoms "1" into yellow circles, while missing atoms "2" are circled in light blue. The $c(2 \times 4)$ unit cells of both the surface oxide and the vacancies network are also shown. We hereby demonstrated that even if the oxygen vacancies sites are randomly distributed for low densities, there is a specific preferred site for oxygen to desorb when

[10] As well as all the ones included in a $c(2 \times 4)$ network.

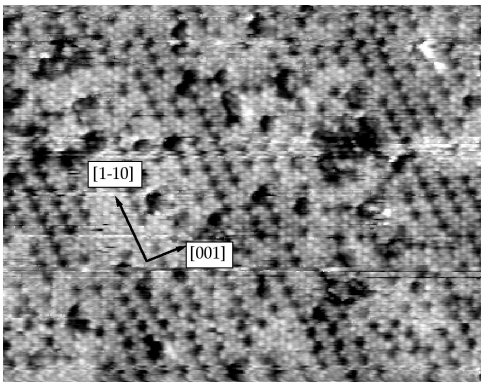

(a)

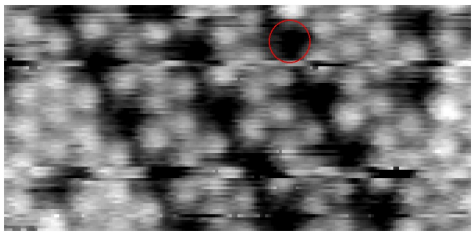

(b) t=0sec

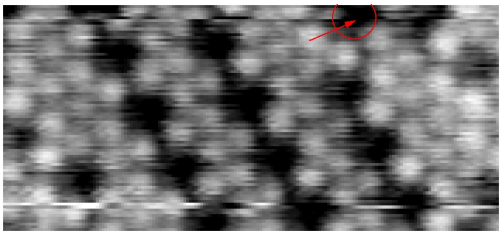

(c) t=30sec

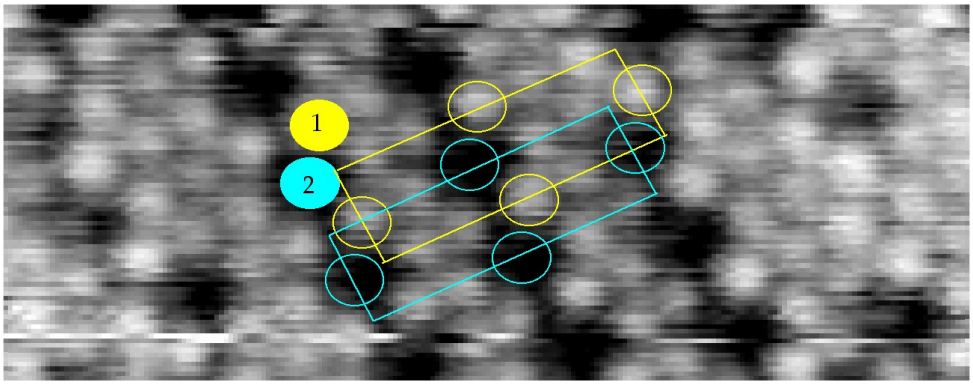

(d)

Figure 4.8: a) STM image of an oxide surface covered with the $c(2 \times 4)$ network of oxygen vacancies, $(20 \times 15)nm^2$, $V_B = 0.5\,\mathrm{V}$, $I = 1.2\,\mathrm{nA}$; b)-c) $(4 \times 2)nm^2$ $V_B = 0.5\,\mathrm{V}$, $I = 1.4\,\mathrm{nA}$; $V_B = 0.5\,\mathrm{V}$, $I = 1\,\mathrm{nA}$: high resolution images of the oxygen vacancies network with a vacancy hopping event highlighted. d) Image in which both the $c(2 \times 4)$ oxide unit cell and the $c(2 \times 4)$ oxygen vacancies network units cell are highlighted. Oxygen atoms "1" are marked in yellow, while missing "2" atoms are indicated in light blue; $(5 \times 2)nm^2$, $V_B = 0.5\,\mathrm{V}$, $I = 1\,\mathrm{nA}$.

their density increases. This $c(2 \times 4)$ network of vacancies plays an important role in both reactivity and ageing of the oxide: in fact, it was first observed as precursor state for titration reactions (see chapter 7.1); moreover, as will be shown in chapter 5.4.2 a trilayer covered with such a structure seemed not to undergo any ageing process.

4.2.3 Preparation dependent morphology

To prepare the surface oxides we used three different oxygen sources, described in chapter 3.2; in this section we describe the surface obtained in every case, that has been the starting point for the oxidation cycles presented in chapter 5.

With the thermal cracker we were able to set up and optimize a recipe that yielded a complete surface oxide all over the surface: the trilayer was the only phase present and it was arranged in very large terraces, as shown in figure 4.9[11]. Moreover, the surface was well-ordered also down to the atomic scale (fig 4.9c, with an extremely low density of defects such as oxygen vacancies or adsorbates. In figure 4.9a- 4.9b we present a large scale image of the oxide with two line profiles acquired along the green and red lines, respectively: the step height inferred from these measurement is $\sim 0.135\,\text{nm}$, corresponding to a single step height of the trilayer[12]; the red profile corresponds to a double step, which was found quite rarely on this surface. Therefore by dosing 24 L of atomic oxygen at 350 °C we were able to grow a perfect trilayer, but we could not form thicker oxides or different oxidation phases: as for other transition metal oxides ([23, 86] and references therein), the surface oxide kinetically hinders subsurface oxygen incorporation, which is required for bulk oxidation. In other words, with atomic oxygen the trilayer is formed so quickly that no extra oxygen can access the subsurface Rh layers. This is consistent with the TDS measurements presented in the next section, that assigned to such oxides the exact coverage of a complete, single trilayer, i.e. 2.5 ML of oxygen.

To form a wetting surface oxide with the TECTRA plasma source, we dosed $\sim 200\,\text{L}$ of atomic oxygen at 350 °C, having a background pressure in the chamber of $p_{O_2} \sim 4 \times 10^{-6}\,\text{mbar}$. Despite the higher exposure with respect to the thermal cracker case, the TDS peak integrals of the plasma-prepared oxides were always smaller than what expected for a complete trilayer (see chap. 5.3.2). STM images, presented in figure 4.10, confirmed that these oxides were not saturated. In fact, the surfaces always presented several oxygen

[11] Based on our experience, oxide formation always lead to terraces at least as wide as on the pristine surface. It has been recently demonstrated that oxidation can cause large terrace widening, also starting from a vicinal surface [91].

[12] This value is the same as for a clean Rh(110) surface.

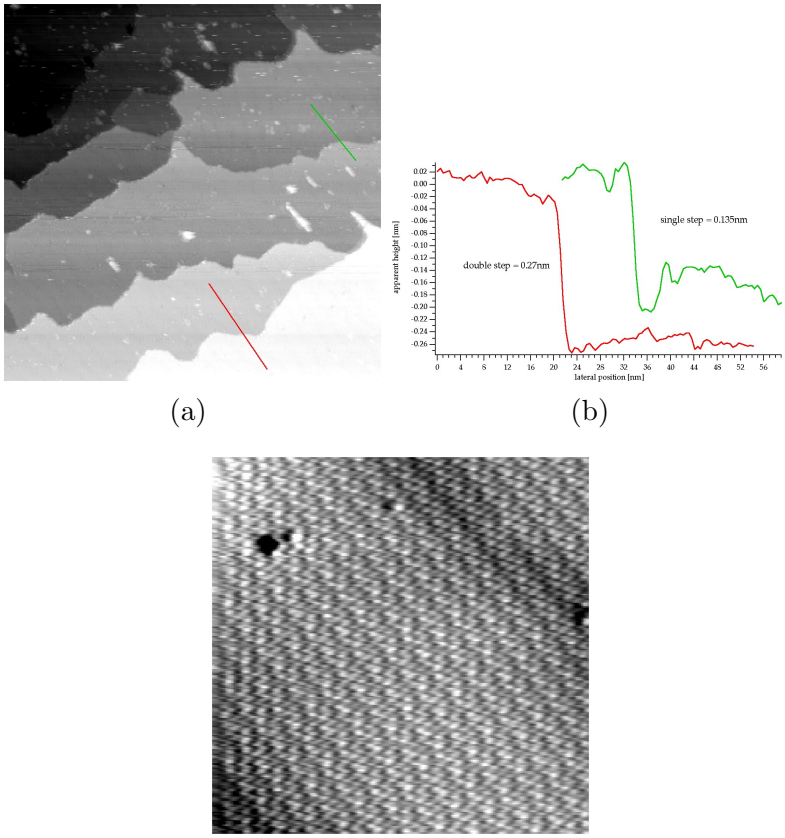

(a) (b)

(c)

Figure 4.9: STM images of a 1^{st} oxide grown with the thermal cracker oxygen source: a) ; b) $(200 \times 200)nm^2$, $V_B = 0.35\,\mathrm{V}$, $I = 0.6\,\mathrm{nA}$; b) image line profiles across the lines in a); c) $(15 \times 15)nm^2$, $V_B = 0.4\,\mathrm{V}$, $I = 0.8\,\mathrm{nA}$.

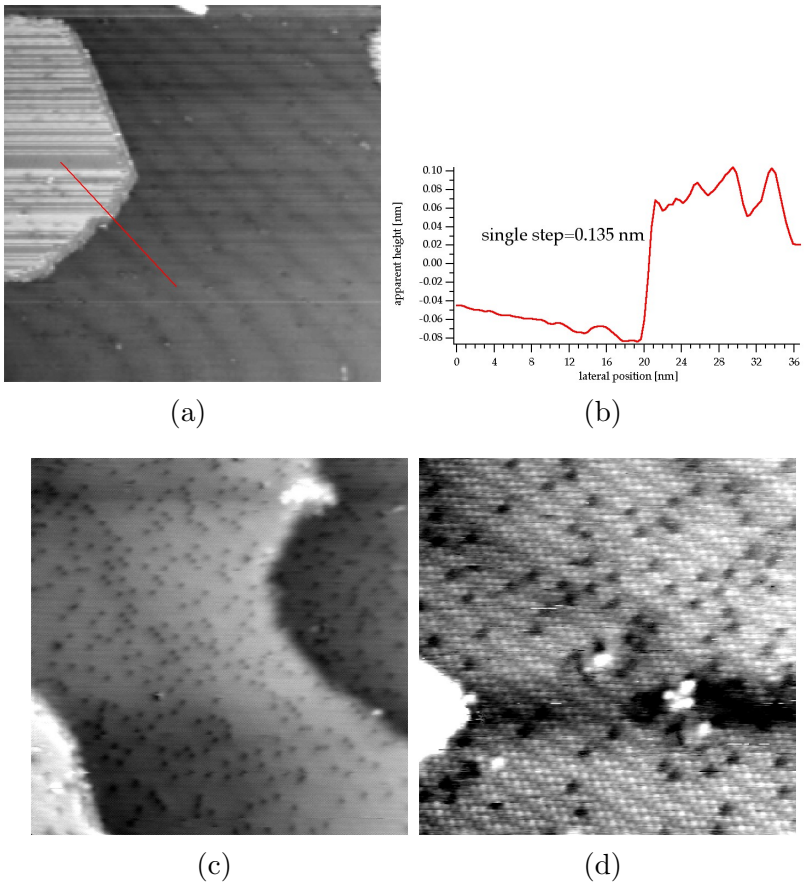

Figure 4.10: STM image of a 1^{st} oxide surface prepared with the plasma source: a) $(80 \times 80\,)nm^2$, $V_B = 0.3\,\mathrm{V}$, $I = 0.2\,\mathrm{nA}$; b) line profile across the line in a); c) $(25 \times 25\,)nm^2$, $V_B = 0.3\,\mathrm{V}$, $I = 0.4\,\mathrm{nA}$; d) $(15 \times 15\,)nm^2$, $V_B = 0.4\,\mathrm{V}$, $I = 0.6\,\mathrm{nA}$.

vacancies already immediately after dosing, while for complete oxides their appearance was observed only after several hours in UHV ambient. This was most probably due to the fact that the plasma beam contained also CO and CO_2, acting as reducing agents and therefore hindering the formation of a full oxygen trilayer[13].

When we decided to use only molecular oxygen for our oxidations, we modified the recipe in two ways:

[13]Moreover, this source yielded charged species that were accelerated to the sample, thus contributing to oxygen vacancies formation.

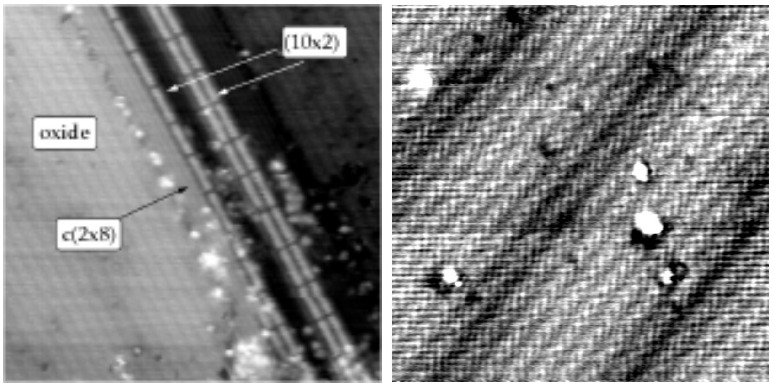

(a) (b)

Figure 4.11: STM images obtained after molecular oxygen exposure: a) at 350 °C, $(25 \times 25)nm^2$, $V_B = 0.5$ V, $I = 2$ nA; b) at 400 °C, $(15 \times 15)nm^2$, $V_B = 0.4$ V, $I = 0.6$ nA. This image is rotated by $\sim 70°$ clockwise with respect to a).

by increasing the sample temperature during dosing, to favour O_2 dissociation;

by increasing the exposure, up to $\sim 10^{+5}$ L[14].

The right temperature was chosen after several trials: keeping the sample at 350 °C, as for the atomic oxygen cases, resulted in surfaces like the one shown in fig. 4.11a. The oxide coexists with adsorption structures, namely the $c(2 \times 8)$ and a phase derived from the (10×2) [84]: the former surrounds the trilayer and occupies the steps proximity, while the latter was found either as segmented Rh-O rows, decorating the steps, or as coupled ones. The (10×2) is a 1D oxide, and is predicted to be the thermodinamically most stable phase at elevated pressures; it is therefore identified with a precursor state for the formation of the surface oxide (see also [91]). Dosing at 500 °C, on the other hand, we were never able to get any surface oxide areas: we only observed a mixture of the $c(2 \times 2n)$ adsorption structures.

Finally, 400 °C proved to be the best choice: a small scale image of a first oxide obtained at this temperature is displayed in figure 4.11b. It is clear that such an oxide does has almost no oxygen vacancies (with respect to a plasma-prepared one); moreover, we obtained terraces as large as 500 nm, as visible from figure 4.12. The growth of a trilayer requires quite large surface rearrangements: the topmost Rh layer increases its density by 25%, and it gets

[14] see chapter 5.

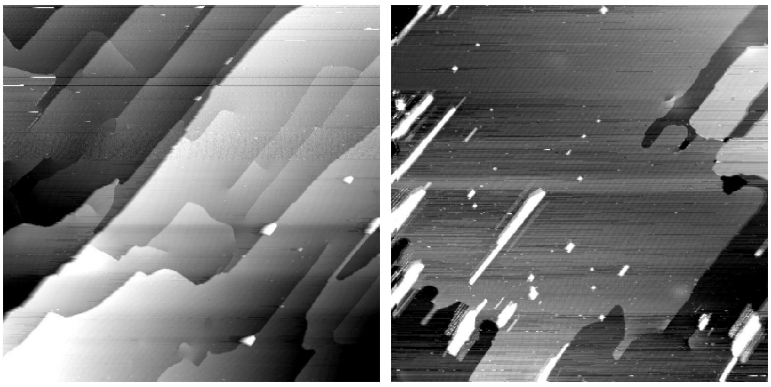

(a) (b)

Figure 4.12: Large scale images of the optimized molecular oxygen oxide: $(500 \times 500)nm^2$ a) $V_B = 0.4\,\mathrm{V}$, $I = 0.6\,\mathrm{nA}$ (1^{st} oxide); b)$V_B = 0.35\,\mathrm{V}$, $I = 0.45\,\mathrm{nA}$ (5^{th} oxide).

trapped between two oxygen layers. To our experience, these transformations often lead to a widening of the terraces; due to the high partial oxygen pressures we used, this effect seemed to be more pronounced than when dosing atomic oxygen.

In figure 4.13 we present two images of oxides prepared by molecular oxygen dosing, together with intensity profiles across the colored lines. The most notable difference between these oxides and the ones obtained by atomic oxygen dosing was indeed their *thickness*: when using O_2, we obtained very often multiple steps, with heights from 3 to 10 trilayer steps. On the contrary, O_{at} grown oxides never had more than double steps.

Since the trilayer step height is the same as the Rh(110) surface one, the measured step height is not a direct proof that we were really growing thicker oxides. However, the confirmation of this hypothesis came from the TDS peak integrals (see chapter 5.3.3): the first oxides obtained by high pressure oxygen exposure[15] contained nearly 70% more oxygen than a single -complete- trilayer, and even the most aged ones corresponded to $\sim 2.8\,\mathrm{ML}$ of O, i.e. to $\sim 40\%$ more.

Therefore exposing the sample to high pressure molecular oxygen resulted in thicker oxides with respect to any of the other recipes. This can be either due to the overall pressure, that was greater by at least one order of magnitude,

[15]before the ageing process set up

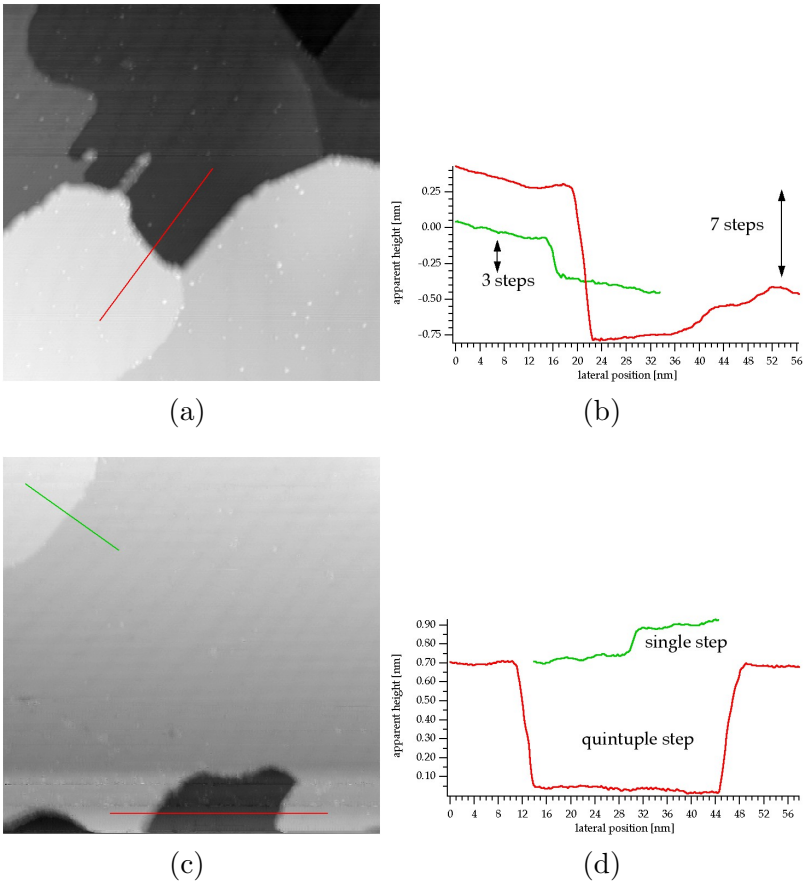

(a) (b)

(c) (d)

Figure 4.13: Large scale images of two oxides prepared by O_2 dosing: a) $(100 \times 100)nm^2$, $V_B = 0.4\,\mathrm{V}$, $I = 0.6\,\mathrm{nA}$ (1^{st} oxide); b) line profiles across the lines in a); c) $(100 \times 100)nm^2$, $V_B = 0.4\,\mathrm{V}$, $I = 0.7\,\mathrm{nA}$ (10^{th} oxide) ; d) line profiles across the lines in c).

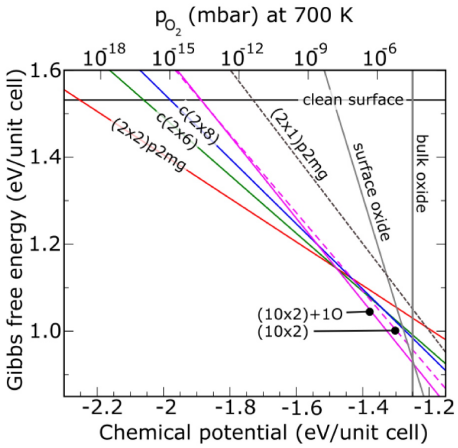

Figure 4.14: Calculated phase diagram displaying the stability of selected oxygen phases; the Gibbs free energy is based on DFT calculations [24] .

or to a different growth process. Oxygen is likely to dissociate at steps, and thus to start the growth from these undercoordinated sites. From the steps it can also enter deeper rhodium layers[16], building multiple trilayers one on top of the other. We know from LEEM data that also the thermal cracker oxides grow from the steps: in fact, the steps determine the prevailing domain on the surface (see sec. 7.2.1). However, we never found more then a double step on the O_{at} grown oxides. In figure 4.14 we plot a calculated phase diagram [24] for the oxygen phases under consideration: the trilayer and the bulk oxide Gibbs free energies intersect in one point at $-1.25\,\text{eV}$, and this indicates that the surface oxide is thermodinamically only metastable and it is probably kinetically stabilized, therefore hindering the formation of the bulk phase.

The oxygen pressure (in the $\sim 10^{-4}\,\text{mbar}$ range in front of the sample) and the temperature ($670\,\text{K}$) used for the molecular oxygen preparations would roughly correspond to a chemical potential at which also the bulk Rh_2O_3 can form; therefore the thicker oxides that we were able to grow represent an intermediate stage between the single surface oxide and the bulk one.

[16]The role of the steps in the oxide growth and in the subsurface oxygen incorporation was already suggested for the Rh(111) surface oxide [23].

4.3 TDS: understanding desorption

As a complementary technique to STM, for studying the Rh surface oxides, we used thermal desorption spectroscopy (see chapter 2.2. TDS provides information on the trilayer's desorption mechanism, therefore accessing the field of surface dynamics; moreover, the spectra are generated by the whole sample surface, contrary to STM images that refer to nanometer-scale areas.

In this section we present the surface oxide thermal desorption spectrum, together with a kinetic model for the mechanism which governs it. Our spectra were collected using an SRS-RGA quadrupole mass spectrometer, recording the oxygen (Mass=32) signal while annealing the sample[17]. To choose the heating rate we had to make a compromise between resolution, acquisition time and our sample holder's characteristics: the value of 2.5 K/sec turned out to be the best one.

To find the correct dose needed to form a complete trilayer, we prepared different surfaces by progressively increasing the oxygen exposure[18]. In figure 4.15a we plot the desorption spectra of the dose series, up to saturation: the grey curve, in fact, corresponds to a complete surface oxide, as confirmed by STM (figure 4.15b). The maximum of the peak shifts towards higher temperatures with increasing dose; if the leading edges had been superimposed, these two facts would have indicated a 0^{th} order desorption process [1, 60]. Nevertheless, this is not our case: the left hand sides of our spectra cross, thus suggesting a different modeling for the desorption kinetics. Such curves can be explained by a transformation, during desorption, of a high coverage phase into a low coverage one, coexisting on the surface. In ref. [62], Klötzer *et al* propose a kinetic model for oxygen desorption from Pd(111), that provides calculated TPD spectra in good agreement with the experimental ones, and remarkably similar to our dose series in fig 4.15a. Following this model, we then name the Rh(110) surface oxide as the "complex" phase (cp), while the one in which the oxide is being converted is named as "diluted" (dp) phase.

On Rh(110) the adsorption structures formed at $\sim 450\,^{\circ}$C with molecular oxygen are the $(2\times 2)p2mg$ (0.5 ML of oxygen), the $c(2\times 6)$ (0.67 ML) and the $c(2\times 8)$ (0.75 ML) [61]. In figure 4.16 the ball models of the $c(2\times 6)$ and the $c(2\times 8)$, together with an STM image, are shown. On the right side of the figure we show a TDS spectrum obtained after dosing ~ 11 L of O_2 at

[17] At the same time we acquired also other oxygen-related signals, namely: mass 16, 18 (H_2O), 28 (CO) and 44 (CO_2).

[18] The sample was sputtered and annealed prior to any dose, i.e. the oxides were always formed on a pristine surface.

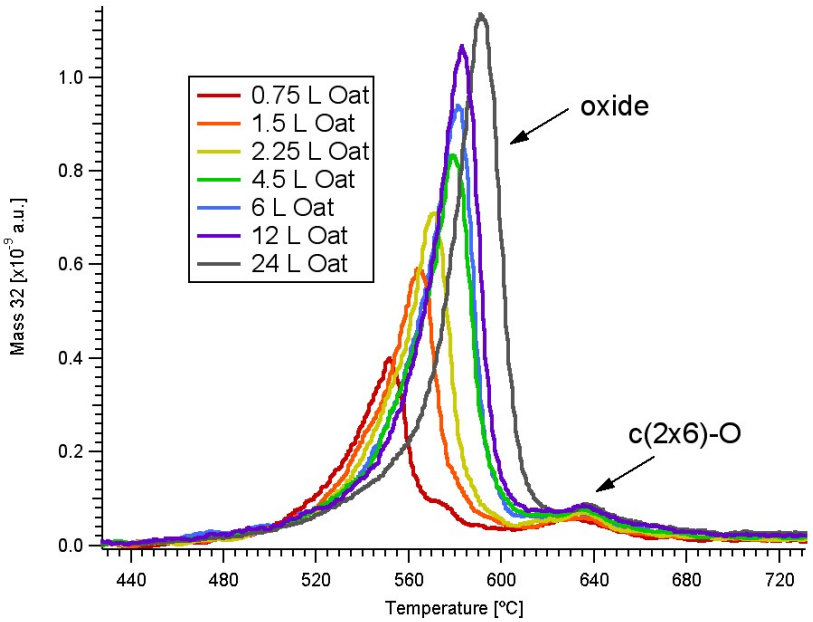

(a)

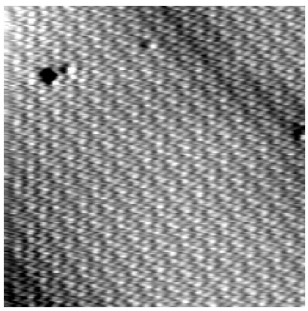

(b)

Figure 4.15: a) TDS spectra after atomic oxygen dosing @ 350 °C on the pristine Rh(110) surface; b) STM high resolution image of the perfect oxide obtained by dosing 24 L of Oat, corresponding to the grey curve, $(15 \times 15)nm^2$, $V_B = 0.4\,\mathrm{V}$, $I = 0.8\,\mathrm{nA}$.

450 °C. The peak at ∼ 565 °C is assigned to oxygen in the $c(2\times 8)$ structure and contains 0.08 ML of oxygen, the one at ∼ 535 °C corresponds to the $c(2\times 6)$ and contains 0.17 ML of oxygen while the remaining 0.5 ML desorb in the broad $(2\times 2)p2mg$ peak centered at around ∼ 830 °C[19] [61].

The maximum of the desorption peak for a complete oxide was found to be at ∼ 585 °C[20], thus in the same desorption window as the $c(2\times 8)$ structure. The $c(2\times 6)$ peak, on the other side, comes right after the oxide and it is clearly identifiable in figure 4.15a. This is an indication that the last $c(2\times 8)$ formed on the surface follows its usual desorption pathway, i.e. through the $c(2\times 6)$ and the $(2\times 2)p2mg$ structures. As a consequence, most of the oxygen desorbs in the lower temperature region, and therefore our main candidate for the "dilute" phase (in the first oxide case) is the $c(2\times 8)$. We can regard it as a stationary transition state, which is continuously formed and reduced. The assignement of the $c(2\times 8)$ as the structure in which the oxide is transformed during TDS is the $c(2\times 8)$ is confirmed by partial TDS experiments: when performing a partial annealing of the oxide (see chapter 5.4.3) we obtained a surface covered with both these structures[21].

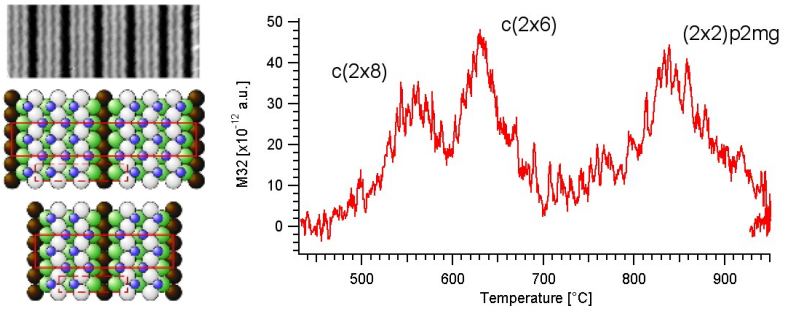

(a) (b)

Figure 4.16: a) STM image and corresponding ball models of the $c(2\times 8)$ and $c(2\times 6)$ oxygen adsorption structures; both structures are visible in the STM image ($c(2\times 6)$ on the right). $(8.9\times 3.3)nm^2$, $V_B = +0.54$ V, $I = 0.46$ nA [84]. b) TDS spectrum of the $c(2\times 8)$, $c(2\times 6)$ and $c(2\times 2)p2mg$ structures.

Given

[19] The $(2\times 2)p2mg$ integral was always lower than expected, most probably due to oxygen desorbing from this structure in other molecules than O_2.

[20] Small deviations from this value could be due to inefficient sample cleaning.

[21] Also annealing experiments in front of the LEED, not presented here, gave the same result.

- complex phase (cp) = surface oxide, and
- dilute phase (dp) = $c(2\times 8)$ structure,

the kinetics are based on the following processes:

$$2O(dp) \leftrightarrows \mathrm{O_2}(g) \quad desorption/adsorption\ of\ oxygen\ on\ dp \tag{4.1}$$

$$O(dp) \leftrightarrows O(cp) \quad transformation\ dp - cp \tag{4.2}$$

To complete the model, a few assumptions are needed:

1. direct desorption from the cp is much slower than from the dp and can therefore be neglected[22].
2. The cp can only decay via the dp: thus the decay of the cp acts as a reservoir of oxygen for the dp. This assumption is supported by the STM images taken at an intermediate stage of desorption (chapter 5.4.3).
3. During desorption the local coverage within the cp islands is constant.
4. The local dp coverage results from simultaneous supply from the cp and loss to the gas phase.

The rate and the mass balance equations can then be written:

$$-\frac{d\theta(dp)}{dt} = \nu(dp)\ \theta(dp)\ e^{-(\frac{E_{des}(dp)}{RT})} \tag{4.3}$$

for the local desorption rate from the dp structure, following 1^{st} order kinetics [61];

$$-\frac{d\theta(tot)}{dt} = -\frac{d\theta(dp)}{dt}(1-F) \tag{4.4}$$

for the total (mean) desorption rate, with

$$F = \frac{\theta(tot) - \theta(dp)}{\theta(cp)_{crit} - \theta(dp)_{crit}} \tag{4.5}$$

F being the surface fraction of the complex phase and θ_{crit} the saturation coverage of a defined phase. In our case $\theta_{crit}(cp) = 2.5\,\mathrm{ML}$, corresponding to the oxygen quantity in a complete surface oxide. If we assume that the diluted

[22]We know from reactivity studies (see chapter 7) that the oxide is much less reactive upon $\mathrm{H_2}$ titration than adsorption structures, thus making this assumption reasonable.

phase is the $c(2\times 8)$, $\theta_{crit}(dp) \simeq 0.75\,\mathrm{ML}$. The total (mean) coverage is simply:

$$\theta(tot) = \theta(initial) + \int \frac{d\theta(tot)}{dt} dt \tag{4.6}$$

While $1 > F > 0$:

$$\theta(dp) \;=\; \theta(dp)_{crit} \tag{4.7}$$

we have a phase transition: in other words, until there is some oxide on the surface ($F > 0$) the dilute phase is saturated.

When $F = 0$

$$\theta(dp) \;=\; \theta(tot) \tag{4.8}$$

the oxide is all converted, and from this point the $c(2 \times 8)$ desorbs via its usual $c(2 \times 8)$ pathway (i.e. first order, converting into the $= c(2\times 6)$ and $(2 \times 2)p2mg$).
From equations 4.4 and 4.5 it is clear that the kinetics during the phase transformation are autocatalytic (factor $(1 - F)$), since the dp area $1 - F$ needs at first to be increased in order to increase the total desorption rate, and in the meantime the temperature of the sample increases. In other words, the larger the fraction of the surface that is covered by the dp phase, the faster the complex phase is consumed. In fact if the starting surface has almost no dp area available, the autocatalytic decrease of cp area F (eq. 4.5) is much slower (at the same temperature/time) than if the starting situation involves e.g. 30% dp area. So the same dp area will become available at a significantly higher temperature. The forward shift of the peak maxima with increasing dose, as well as the crossing leading edges, can therefore be explained in the framework of "explosive" desorption [62, 92].

As will be shown in the following chapter, the desorption mechanism remained quite the same during the oxidation cycles, regardless of the presence of contaminants or of the oxygen source used. Moreover, this autocatalytic model turned out to be crucial to understand the ageing process.

4.4 Reduction by UHV background

The surface oxides were not in equilibrium with the background pressure of our UHV experimental system: we could systematically observe that they

got partially reduced after one night and, even more, after a week-end. Our background pressure ($p \sim 2 \times 10^{-10}$ mbar at best, $\sim 5 \times 10^{-10}$ mbar after a day of cycles) was mainly composed by hydrogen; when using the plasma source, moreover, CO and CO_2 partial pressure significantly increased during dosing. All these molecules are reducing agents for the oxide, even at room temperature. What we saw, as a matter of fact, was a progressive increase in the number of oxygen vacancies, which built up a $c(2 \times 4)$ network (fig. 4.17).

This structure, presented in detail in section 4.2.2, is exactly the same that forms during the induction time of the reduction reactions: only after its completion the reaction front could ignite and travel throughout the oxide [66](see chapter 7).

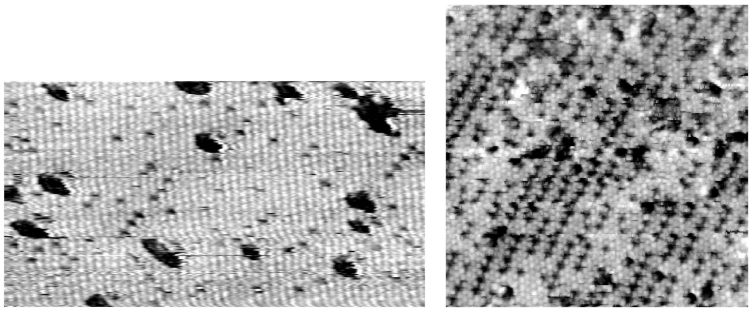

(a) $(15 \times 8)nm^2$ (b) $(10 \times 10)nm^2$

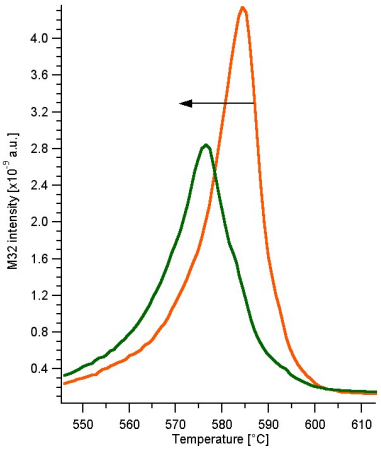

(c)

Figure 4.17: a) STM image of an oxide left overnight in UHV, $V_B = +0.4\,\mathrm{V}$, $I = 0.35\,\mathrm{nA}$; b) STM image of an oxide after a week-end, $V_B = 0.5\,\mathrm{V}$, $I = 1.4\,\mathrm{nA}$; c) TDS spectra of a fresh first oxide and of an oxide left in the UHV overnight.

The partial decomposition of an oxide at room temperature in UHV had a precise signature in its TDS spectrum: as shown in figure 4.17c, after leaving the oxide overnight in the chamber the peak was backshifted by $\sim 8\,^{\circ}\mathrm{C}$ with respect to a fresh first oxide. Moreover, the integral was lowered by $\sim 10\%$[23].

Reduction by background gases was observed not only on first oxides but also during the oxidation cycles, anytime an oxide was left for several hours in UHV. In these cases, we found a backshift and a lowering of the integral with resect to the previous oxide (i.e. not necessarily to the first one). As a consequence, these curves have to be removed from the series when analyzing the evolution of the spectra with the cycles.

An intuitive way of understanding the TDS backshift is to think that an oxide containing oxygen vacancies is more easily transformed into an adsorption structure, leading to a lower temperature for the desorption peak. More in detail, the total initial coverage $\theta(tot)$ of such an oxide is lower than the cp critical one (2.5 ML), thus decreasing the value of factor F in equation 4.5 and correspondingly leading to the peak backshift. This is exactly the same situation of the spectra in figure 4.15a, obtained after dosing lower quantities of oxygen than the one needed to form a complete layer.

[23] A 10% decrease is expected when all the topmost layer is covered with the oxygen vacancies network. Since this was not the case, adsorption from the background during the night (dark irregular features in the two images) and subsequent reaction of these contaminants with the oxide during TDS may therefore account for the observed decrease.

Chapter 5

Ageing effects upon oxidation cycles

In this chapter we present and analyze the various ageing effects that we observed during repeated oxidation cycles of our sample. The extreme oxidation conditions we applied are the following:

- atomic oxygen exposure, through the thermal cracker and the plasma sources, and high oxygen pressures when using the doser[1];
- the relatively high sample temperatures at which the oxides were formed: 350 °C-400 °C for the trilayer, and 730 °C for the first oxidation step in the mixed cycles (sec. 5.2).

The most important ingredient for the ageing, anyway, is the cycling procedure itself. The continuous iteration of oxidation and annealings was the key factor for the ageing progress. Opposite to the usual surface science approach, we do not prepare our system (i.e. an oxide) every time on a pristine surface: our oxides are dosed repeatedly over more and more aged surfaces, thus mimicking what happens in real catalysis than what comes out following a standard UHV recipe.

The ageing procedures lead to unavoidable contaminants accumulation throughout all this thesis work: we start therefore from an overview of these contaminations, coming either from the thermal cracker source or from different kinds of sample holders.

In the second section we expose the cycles idea, going into the details of the recipies which have been varied to maximize the ageing effects.

[1]The pressure in the preparation chamber was 1×10^5 mbar, but we estimated the real pressure at the sample to be $\geq 1 \times 10^4$ mbar (see 3.2)

The main body of the chapter is then composed by the subsequent two sections that present the ageing effects: the TDS and the STM measurements which have been performed while proceeding with the cycles. Finally, the last section is dedicated to the analysis of the ageing phenomena observed during the different cycles and to our explanations of the various processes.

5.1 Contaminants survey

As stated above, we found two sources of contaminations: the thermal cracker and our sample holders. Our experimental chamber is not equipped with an XPS tool (see chapter3.1); the only instrument capable of chemical resolution we have is a hybrid LEED/Auger Electron Spectroscopy (AES) system. However, the detection threshold of our Auger is about $\sim 10\%$ of a monolayer, i.e. too high for to the coverages we had. Moreover, given the source specifications, we did not expect any related specific contamination, and this is the reason why we discovered the problem only when acquiring overview spectra at the synchrotron. In figure 5.1 we present a collection of spectra corresponding to oxide preparations that yielded significant presence of Pt and Ir contaminants on the surface. As a general trend, we found out that the platinum coverage was increasing with increasing source power, while the iridium content was mainly related to the oxygen pressure. The first observation can be easily understood knowing that Pt was coming from the source's shield, which was poorly cooled (chapter 3.2.1): a higher power was supplying more heat to the shield, facilitating Ptox species formation and evaporation. Since the cracking capillary was made of iridium, Irox species were instead formed as by-products of the oxygen dissociation. Therefore a higher oxygen pressure onto the capillary walls was likely to generate more of these species and to cause a greater sample contamination.

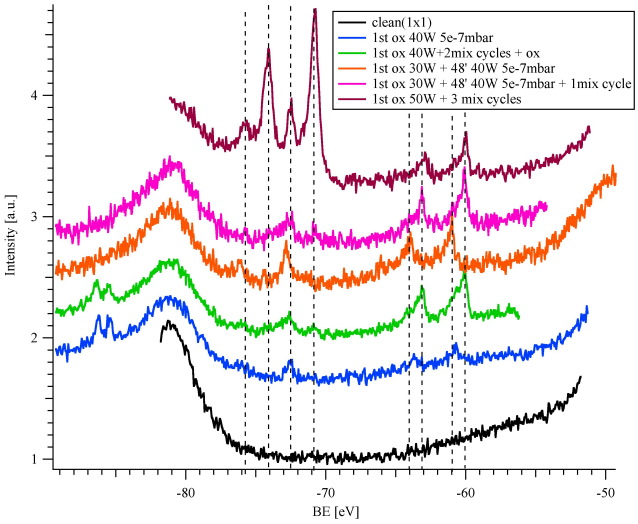

Figure 5.1: Pt4f and Ir4f region, showing the presence of platinum and iridium on the surface oxide in both their metallic and oxidic form. The broad peak on the left side is the Rh4s level. Unless specified, $p_{O_2} \sim 1 \times 10^{-7}$ mbar.

The two peaks at $\sim$ 70.8 eV and $\sim$ 74.1 eV correspond to the platinum $4f7/2$ and $4f5/2$ core levels for a metallic state Pt^0. The ones at $\sim$ 72.5 eV and $\sim$ 75.8 eV, on the other hand, are assigned to Ptox species [93]. Depending on the oxide preparations, different proportions between the oxidized and metallic components were observed. Also iridium was present on the surface in both metallic and oxidized form: Ir^0 gives the peaks at $\sim$ 60 eV and $\sim$ 63.1 eV ($4f7/2$ and $4f5/2$, respectively), while the $\sim$ 61 eV and $\sim$ 64.1 eV doublet originates from IrO_2. These XPS data suggested that our surface was covered with clusters composed of platinum and iridium, most probably organized in core-shell clusters, the inner part being metallic and the outer one oxidized. The purple spectrum in figure 5.1 corresponds to the longer oxygen exposure at the maximum power: it is also the one that shows the maximum content of platinum (and nearly the maximum of Ir), mainly in metallic state. Since the metallic component of a cluster increases with the volume while the oxidized one scales with the surface, this spectrum agrees with the proposed model.

As shown in more detail in section 5.4, the STM data confirmed this hypothesis. In fact, as presented in figure 5.2, when using the thermal cracker for the oxidation we observed a progressive increase in bar-like and rounded structures while proceeding with the cycles. The maximum coverage we estimated from the purple spectrum in fig. 5.1 was $\sim$ 7% for Pt and $\sim$ 1.5% for Ir; however,

from STM images, after 18 cycles the oxide looked completely covered by clusters (see fig. 5.2b). This apparent inconsistency can be explained by the fact that at Superesca beamline the source was at about twice the distance from the sample with respect to our chamber. It is thus reasonable to assume that a surface like the one in fig. 5.2b was covered with more Pt and Ir than in the presented spectra. A second hypothesis is that rhodium formed an alloy together with platinum and iridium: in that way the clusters observed with STM could have been made only in a small proportion by the contaminants, thus explaining both the surface morphology and the XPS derived data.

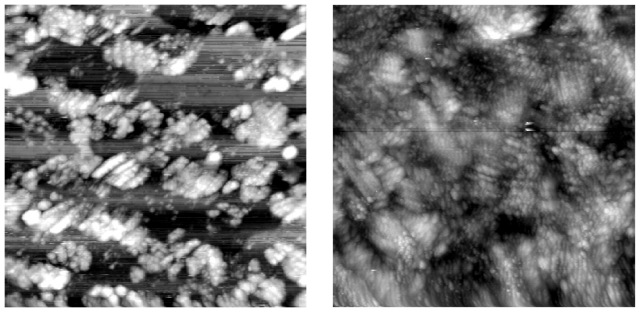

(a) $12^{th} oxide$ (b) $18^{th} oxide$

Figure 5.2: STM images of two oxides prepared with the thermal cracker oxygen source: a) 12^{th} oxide, $(100 \times 100)nm^2$, $V_B = +0.4\,\mathrm{V}$ (empty states), $I = 1\,\mathrm{nA}$; b) $(100 \times 100)nm^2$, 18^{th} oxide, $V_B = -0.4\,\mathrm{V}$ (filled states), $I = 0.6\,\mathrm{nA}$.

An indirect but convincing confirmation that the extra structures observed on the surface oxide were made of platinum and iridium derives from the fact that we never observed again clusters on our oxides, when using different oxygen sources. We know from XPS spectra (not shown) that already after an annealing to 620°C not only the surface oxide was decomposed, but also Pt and Ir were present only in their metallic form. From STM we deduced that they were not dissolving into the bulk, and in fact we could find "foreign" islands on the (1×1) surface obtained after annealings to 1030°C. In figure 5.3a we present four images of the different areas we observed. Islands of "A" show a semiordered hexagonal structure, which has to be related to platinum and/or iridium since it was never seen without using the thermal cracker, as well as the clusters on the oxide. The same holds for structure "B", which is also hexagonal but with brighter rows along the$[1\bar{1}0]$ direction with almost regular periodicity; moreover, "B" was only seen at the borders of "A". Structure "C", shown in figure 5.3d, was quite rare with respect to the previous two, was

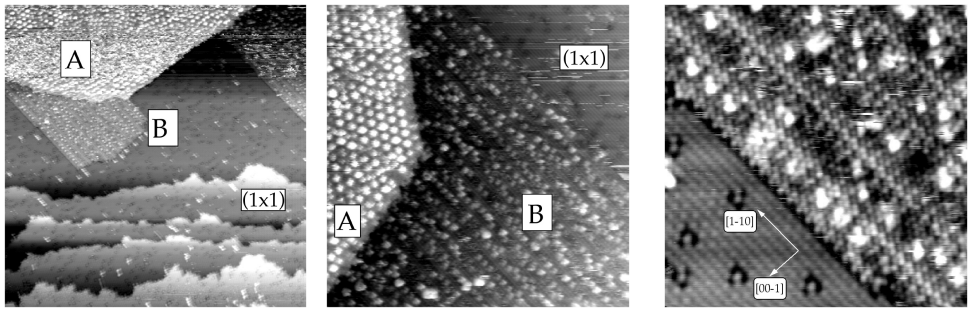

(a) $(100 \times 100)nm^2$ (b) $(50 \times 50)nm^2$ (c) $(15 \times 15)nm^2$

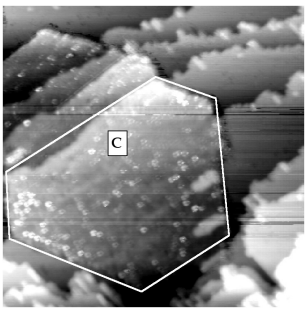

(d) $(100 \times 100)nm^2$

Figure 5.3: a)-b) "A" and "B" regions found on the (1×1), $V_B = 0.5\,\mathrm{V}$, $I = 1.4\,\mathrm{nA}$; c) zoom on the "B" structure and the nearby (1×1), $V_B = 0.5\,\mathrm{V}$, $I = 2.4\,\mathrm{nA}$; d) Trapezohedral island of structure "C", $V_B = 0.5\,\mathrm{V}$, $I = 1.8\,\mathrm{nA}$.

organized in islands of trapezohedral shape and was found again also using the doser (see fig. 5.6).

The second source of contamination in our experiments was closer to the sample with respect to the O_{at} source: some of the materials of our sample holders (Al, Ni, Ta) were attacked by atomic or molecular oxygen, leading to the formation of volatile oxides which stuck on the crystal surface. As in the thermal cracker case, accumulation was caused by the cycles procedure itself; it has to be remarked, anyway, that even after $\sim$40 cycles the maximum quantity of these contaminants was $\sim 1.5\%$. In figure 5.4 we present the three different kind of sample holders which we used for our experiments. In the third picture our sample holder (1^{st} kind) is inserted in a cage. This hybrid system was specifically designed and assembled to perform XPS measurements

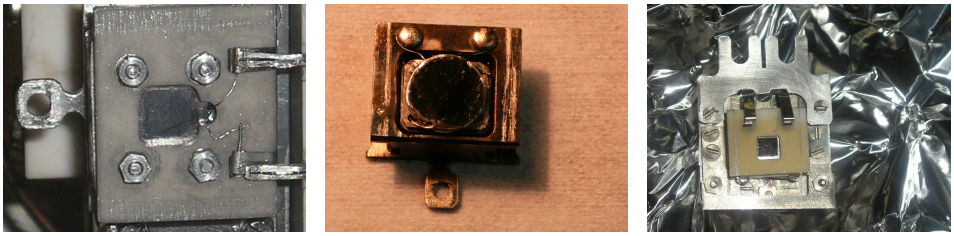

(a) (b) (c)

Figure 5.4: a) First kind of sample holder used, with the Alumina ceramic top plate ; b) Second kind, with the sample fixed over a tantalum foil; c) hybrid STM–XPS system: the STM sample holder (1^{st} kind) enters the large cage rotated by 90°.

at the TASC Photoelectron Diffraction group[2]. The first kind of sample holder (fig. 5.4a) is a modified Omicron design, in which type K thermocouples in direct contact with the sample have been added. The upper plate is made of Alumina, and the sample can be accessed from a hole in the plate. On the right side there are the Chromel and Alumel junctions[3], contacted either by the manipulator (like in the picture) or by the STM ones; the two thin wires (0.25 mm) connect directly the contacts with the crystal, on whose they are spotwelded. This modification was essential for reactivity studies ([42]) but also for our TDS spectra, to have a measurement of the sample temperature in real time. After ∼20 cycles with the thermal cracker source and this kind of sample holder, the contaminants concentrations could be roughly estimated as:

Alumina $\lesssim 0.5\%$ML

Nickel $\lesssim 1\%$ML

For both the plasma and the doser cycles (see 3.2) we used a new kind of sample holder, showed in fig. 5.4b. In this case, the entire crystal is exposed, fixed by two wires spotwelded on a Ta foil, thus protruding outwards from the sample holder. In this way we were able to go a couple of millimeters closer when oxidizing, and we got rid of the alumina contamination. Nevertheless, we had again nickel coming from our thermocouples and, most probably due to the high pressure of oxygen in front of the sample, a tantalum contamination. In

[2]This group is a branch of the SSR one, working at Elettra with a SPA-LEED and a laboratory XPS equipment.

[3]Containing $90 - 95\%$ of Ni.

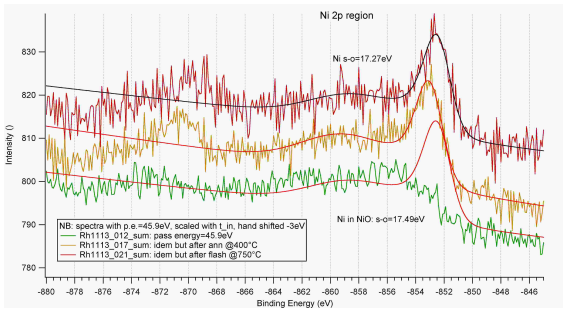

(a) Ni2p

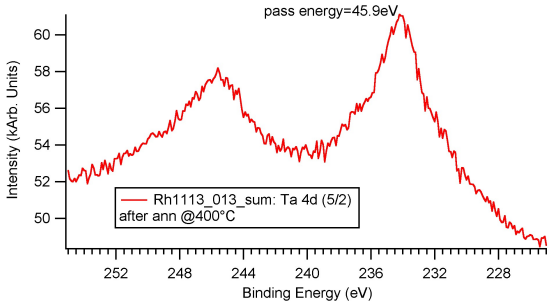

(b) Ta4d

Figure 5.5: Ni2p and Ta4d spectra acquired with a Mg$K\alpha$ laboratory source.

fig. 5.5 we plot the spectra of the Ni2p and the Ta4d levels; both were oxidized after the surface oxide preparation, but Nickel became progressively metallic upon annealing. From these spectra we estimated the following contaminants concentrations:

Tantalum $\lesssim 1.5\%$ML

Nickel $\lesssim 1\%$ML

Also after desorbing the oxides formed with the doser (and the second kind of sample holder) we observed some "foreign" islands on the (1×1) surface. They were much rarer than in the thermal cracker case and all showing the same structure, with a trapezohedral shape. As shown in figure 5.6, the islands seem to block terrace expansion, making steps curving around them. Unluckily we do not have any high-resolution image to understand their inner atomic arrangement, but their shape, position and contrast resemble those of structure

"C" presented above[4]. From these data we cannot conclude if they were made of tantalum or nickel; there's only a little hint towards the second hypothesis, due to the fact that Ni was the only common contaminant in all our experiments.

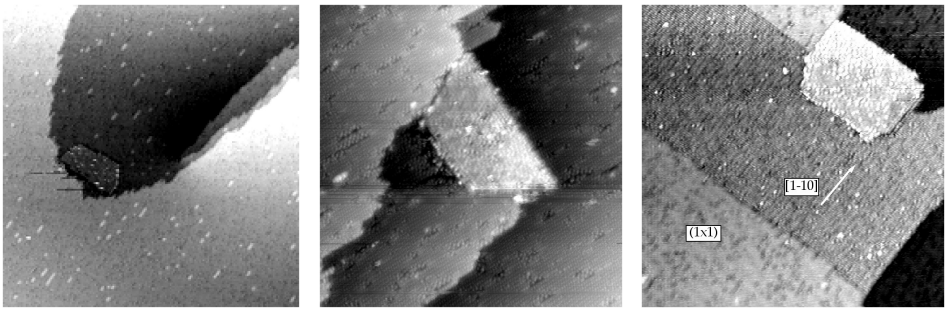

(a) $(140 \times 140)nm^2$ (b) $(35 \times 35)nm^2$ (c) $(80 \times 80)nm^2$

Figure 5.6: a) large scale image showing a trapezohedral island (compare with image 5.3d) deviating the terrace growth, $V_B = 0.4\,\mathrm{V}$, $I = 0.2\,\mathrm{nA}$; b) close up on such an exotic region, $V_B = 0.3\,\mathrm{V}$, $I = 0.35\,\mathrm{nA}$; c) trapezohedral area at the boundary with a more rare extra structure, $V_B = 0.3\,\mathrm{V}$, $I = 0.4\,\mathrm{nA}$.

To summarize, in this section we presented an overview of the different contaminants which we found on our surfaces during this PhD work; the only one which was common to all our preparations was nickel.

5.2 The cycles idea

The usual surface science approach is based on well defined preparation conditions and quite strict requirements: in many cases all the preparation and characterization processes are realized in UHV chambers, dosing ultra-pure gases and using single crystals as simplified model samples. In fact, if the experimentalist wants to look at structure and dynamics of matter down to the atomic scale level, the quenching of any possible external influence on the studied system is of uttermost importance.

Nevertheless, linking a model system to its counterpart in "real" (e.g. industrial) life is far from straightforward. After having studied the structure and reactivity of the trilayer surface oxide grown in UHV conditions on

[4]When mounted in the second sample holder the crystal was rotated by $\sim 90\,^\circ$ with respect to the first mounting; thus the crystallographic directions are swapped in the STM images

Rh(110)(chapters 4, 7) we wanted to mimic the oxidation process as it is performed in real Rh-based catalysis. As rhodium (together with platinum and palladium) is widely used as the active part of TWC, a wealth of studies have addressed its behaviour under realistic reaction conditions ([17, 18] and references therein). One of the main goals of such a research work is to understand the mechanisms leading to catalyst deactivation (i.e. ageing), so as to prevent or at least minimize them.

Probably the best method for artificially ageing a three way catalyst is to perform the so called *engine ageing cycles*, that means running an engine over a bench for several tens of hours. Kallinen *et al* first exposed the catalyst to an engine ageing procedure, i.e. to varying conditions: stoichiometric, strongly oxidizing and reducing with simultaneous rapid temperature variations [17]. In a laboratory, however, oven ageing under controlled air pressures at high temperatures (~ 1000°C) is more easily coupled with characterization techniques to determine the surface area and the oxygen storage capacity. In figure 5.7 Kallinen *et al* report the temperature diagram of a TWC cell during both engine and laboratory ageing cycles: the laboratory one could follow quite well the temperature increase of the engine one (dark curve in the figure), but the cooling edge was much smoother. This study confirmed that the driving forces in the ageing are the concentration changes of the exhaust gas together with the temperature fast variations.

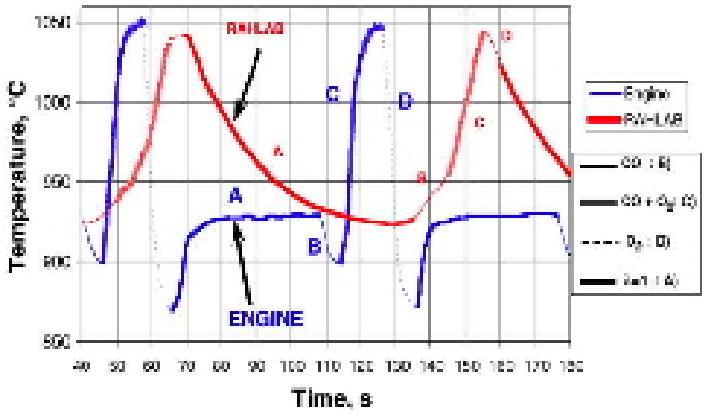

Figure 5.7: Temperatures of the cell during the engine and the laboratory ageing cycles: (A) stoichiometric phase, dark thick line; (B) enrichment phase, dark thin line; (C) additional air and CO phase, thick cracked line; (D) oxidizing phase, thin dash line [17].

Our step from surface science towards real catalysis consisted in the development of a laboratory ageing procedure for our Rh(110) sample, that allowed us to mimic a real catalytic cycle and at the same time to use the standard UHV preparation and characterization techniques (chap. 3.1). Since it has been proved that the most damaging effect on the catalyst performance originates from the oxidizing atmosphere at high temperatures [94, 95], we setup a cycle in which both ingredients were present: an oxidation with either atomic or high pressure molecular oxygen is followed by an annealing up to ~ 1000°C.

A schematic representation of this idea is depicted in figure 5.8: after the preparation of an oxide, we study the surface with atomic detail with our STM (represented by the orange arrow). Subsequently, we make an annealing, during which we acquire a TDS spectrum, thus obtaining a complementary set of informations on the system while doing this second step of the cycle. The resulting surface can be covered with oxygen adsorption structures or can be the clean (1×1), depending on the temperature reached during the TDS; as will be shown in chapter 6, the STM study of the (1×1) evolution during the cycles turned out to be a crucial issue for the overall understanding of the ageing process. This characterization is represented by the blue arrow, that leads right to the beginning of the subsequent cycle.

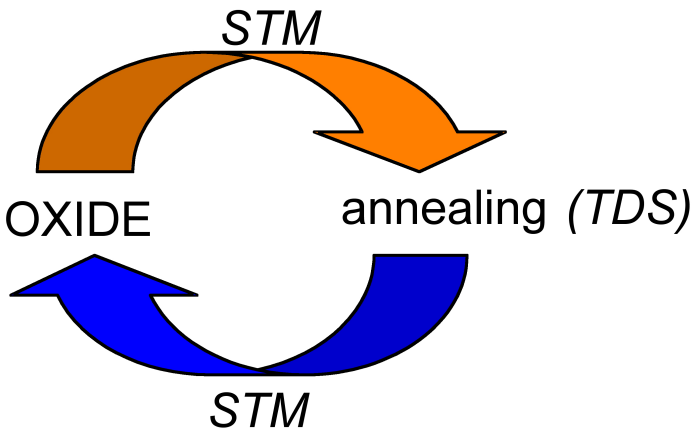

Figure 5.8: Schematic view of the cycle idea.

A single cycle in the original recipe we setup had the following structure:
OXIDE CYCLE :

- oxide formation @350 °C
- annealing (TDS) up to 1030 °C

and we had the possibility to characterize our system before or after each step. As already presented in chapter 4, the formation of a complete oxide using the thermal cracker required a dose of 16 min using $p_{O_2} \sim 1 \times 10^{-7}$ mbar and operating the source at 50 W; this corresponded to an atomic oxygen dose of ~ 24 Langmuir[5]. While using the thermal cracker, we developed also an alternative procedure where the oxidation step was performed at two different temperatures; we therefore called this recipe "mixed" cycles.

MIXED CYCLE :

- mixed oxidation

  1. oxygen dose (1 h) @730 °C
  2. H_2 titration (~ 5 L) @500 °C
  3. oxide formation @350 °C

- Annealing (TDS) up to 730 °C

- H_2 titration (~ 5 L) @500 °C

In the mixed cycles, the first oxidation step supplied ~ 96 L of atomic oxygen[6]. After the TDS up to 730 °C, only the $(2 \times 2)p2mg$ adsorption structure remains on the surface; we wanted to remove this structure (i.e. lifting the reconstruction) to get a flat (1×1) surface over which to dose a standard oxide[7]. The titration follows our standard recipe (~ 7 L of H_2 at 500 °C for the removal of the $(2 \times 2)p2mg$ structure [61, 84]. The final part of the oxidation is made of a single oxide formation, and the cycle is closed by taking again a TDS up to 730 °C and titrating with H_2 before the beginning of the subsequent cycle. Since the interesting part of the TDS spectra is the oxide desorption temperatures range, it was enough to stop the annealings up to 730 °C. For this same reason, also the simple oxidation cycles we performed using the plasma source contained an annealing to 730 °C instead of 1030 °C.

When using the doser, the oxidation cycles had to be slightly modified in both sections:

[5] In addition to O_{at} we dosed also molecular oxygen: its overestimated dose is obtained by considering the source as switched off, so ~ 60 L.

[6] and ~ 180 L of O_2 from the background.

[7] As shown in chapter 7.2, a starting surface which is not flat may lead to a complete different oxide morphology.

- the oxide preparation was done at 400 °C instead of 350 °C because this was the temperature providing the best oxide; the differences can be traced back to the O_2 dissociation step.

- The maximum temperature we could reach was $\lesssim 850$ °C, due to the 2^{nd} kind of sample mounting.

The doser was operated using a maximum value of $p_{O_2} \sim 1 \times 10^{-2}$ mbar in the gasline, while the pressure in the preparation chamber was $\sim 1 \times 10^{-5}$ mbar. The partial pressure in front of the sample was estimated to be one order of magnitude higher (see 3.2.3); to form a complete oxide we needed to dose for 20 min, equivalent to a molecular oxygen dose of the order of $\sim 10^{+5}$ L. In the following table we summarize the recipes that have been used to produce the data sets presented in this thesis, together with the oxygen source and the number of cycles (i.e. iterations) that have been performed.

source	**recipe**	**♯ cycles**
Thermal cracker	oxides @350 °C	20
Thermal cracker	mixed cycles	6
Plasma	oxides @350 °C	12
Doser	oxides @400 °C	46

5.3 TDS data: desorption evolution

The two main techniques that we used to monitor the evolution of the surface oxides as long as we proceeded with the oxidation cycles are TDS and STM. In this section we present the information obtained by TDS, that is integrated over the whole surface of the sample, thus being complementary to STM measurements. Depending on the oxygen source used, we observed different behaviours upon cycles iteration; nevertheless, the desorption mechanism was found to be always the same.

When dosing atomic oxygen, we overcame the oxygen dissociation step, which indeed turned out to be a crucial one in the (intrinsic) ageing process[8](see sec. 5.3.3). Notwithstanding all this, the huge changes that we observed in the spectra as long as we proceeded with the cycles can all be explained starting from the phase transformation described in chapter 4.3.

[8]Modifying our recipes to use molecular oxygen only, in fact, was a further step to better mimic what happens in real catalysis.

5.3.1 Thermal cracker cycles

The first cycles' series that we tested on our Rh(110) sample consisted in oxidation at 350 °C and subsequent annealing (TDS) up to 1030 °C (chapter 5.2). For the oxidation we used the thermal cracker described in section 3.2, generating a beam with 30% of atomic oxygen. This allowed us to form the oxides at relatively low background pressures in the UHV chamber ($p_{O_2} \sim 1 \times 10^{-7}$ mbar), but on the other hand we had to face a contamination of the surface (sec. 5.1).

In the following graphs, we plot an overview of the 20 oxidation cycles: it is immediately evident that the TDS spectra changed both in shape and peak temperature. The overall shift of the peak towards higher temperatures between the first and the 20^{th} cycle is ~ 40 °C. Moreover, comparing the black and the purple curve in fig. 5.9, we see that the peak-maximum of the last oxide is in the desorption temperature range of the $c(2 \times 6)$ adsorption structure, where the first oxide showed only a small shoulder. On the other hand, the first oxide maximum is in the $c(2 \times 8)$ region[9], where the 20^{th} oxide has a shoulder. Therefore, these two spectra point toward an exchange process between the $c(2 \times 8)$ and $c(2 \times 6)$ adsorption structures as dilute phases the oxide desorbs through.

The spectra which have a backshifted maximum, with respect either to the first oxide or to their previous one in the series, always correspond to oxides which have been left for several hours (i.e. night or week-end) in UHV. The overall trend, anyway, is a continuous shift of the prevailing peak towards higher temperatures. In figure 5.10 we present the evolution of the peak temperature as long as we proceeded with the cycles, together with the peaks integrals. While the peak temperature shows a pronounced increasing trend, the amount of oxygen desorbing from the surface is only slightly higher for late oxides with respect to the first ones. The integrals are calculated from 380 °C to ~ 730 °C, so as to include the surface oxide region but not the $(2 \times 2)p2mg$ structure. Since this structure contains 0.5 ML of oxygen [61, 84], the peak integrals calculated up to 730 °C correspond to only 2.0 ML out of the 2.5 ML of the oxygen building the trilayer.

[9]The first oxide maximum is at ~ 595 °C, higher than what stated in the previous paragraph. We can attribute this difference to the sample's cleaning procedure we used at that time, that consisted in sputtering with 1 keV Ar^+ ions. In later measurements, like those with molecular oxygen, we always sputtered with 3 keV and the first oxide peak position was much more reproducible around ~ 585 °C.

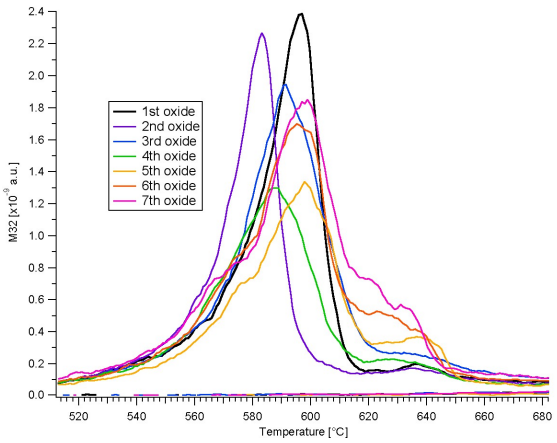

(a) oxides $1^{st} - 7^{th}$

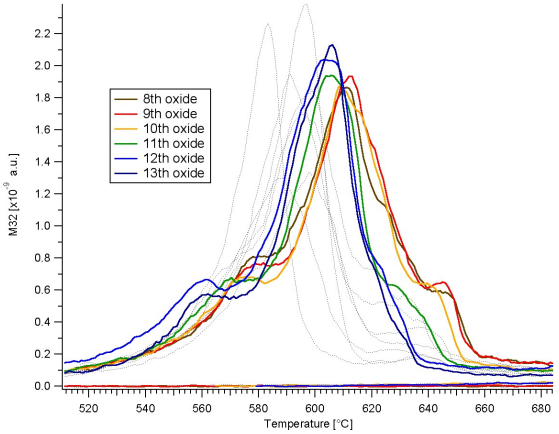

(b) oxides $8^{th} - 13^{th}$

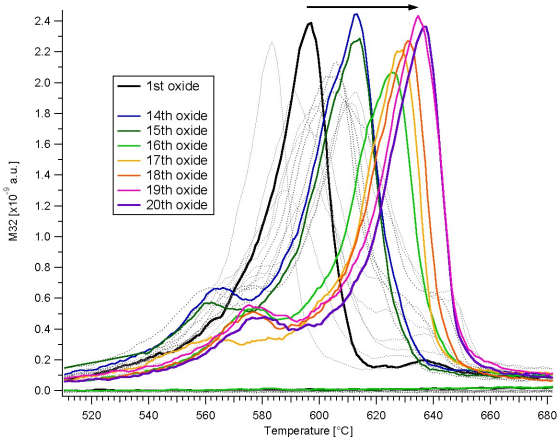

(c) oxides $14^{th} - 20^{th}$

Figure 5.9: TDS spectra of the 20 oxidation cycles.

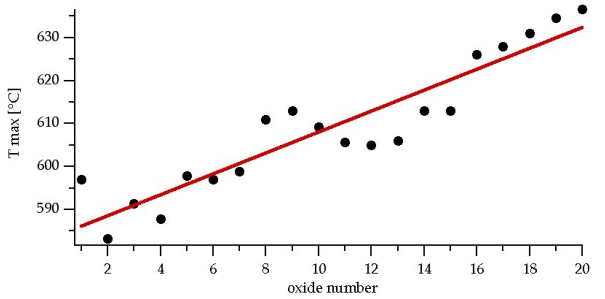

(a) T_{max}

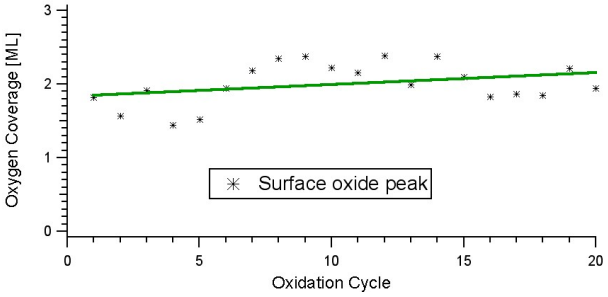

(b) *integrals*

Figure 5.10: a) Peak-maximum temperatures within the 20 oxidation cycles; b) integrals of the TDS spectra (up to 730 °C).

The shape and position of the TDS peaks suggest a progressive transition, during the cycles, from $c(2 \times 8)$ to the $c(2 \times 6)$ as "dilute" phase in which the oxides are converted prior to oxygen desorption. Thus the desorption mechanism remains the same, and the evolution consists in different proportions of the two adsorption structures during the phase transformation. The change in the desorption pathway is a TDS-signature of the ageing process.

In order to give a comprehensive picture of the desorption mechanism evolution we need to recall what has been stated in sections 5.1 and 4.3. As will be also confirmed by STM images in the next section of this chapter, the oxides were progressively affected by the presence of contaminant species, namely platinum and iridium in both metallic and oxidic form, which were removed from the crystal only by sputtering. We do not have a precise estimate of the contaminants coverage during these cycles; however, we can reasonably assume that they were present in a similar quantity to what measured after some mixed cycles, i.e. less than $\sim 10\%$ of a monolayer (see chapter 5.1). We propose hereafter some possible explanations for the shift of the peak temperatures,

which are not mutually exclusive:

We know from XPS data (sec. 5.1) that after annealing to $\sim 620\,^{\circ}\mathrm{C}$ both platinum and iridium were completely reduced, i.e. present on the surface only in metallic form. During the annealing the Pt and Ir clusters were dissolving into the surface oxide, supplying oxygen to it and thus "slowing down" the oxide phase transformation into adsorption structures. In mathematical terms, they were keeping the F factor (equation 4.5) equal to 1, and so pushing the onset of desorption towards higher temperatures. However, comparing the two graphs in figure 5.10, we see that there is no straightforward correlation between the most shifted spectra and the higher integrals values. Either the oxidized outer shell of the clusters is not the main responsible for the peak shifts, or oxygen from these structures was able to dissolve into the subsurface region, thus not contributing to our integrals.

A second possibility is that Pt and Ir atoms were mechanically hindering the conversion of the oxide into the $c(2 \times 8)$ adsorption structure.

Moreover, it cannot be excluded that the change in the desorption pathway was caused by a "complex" phase different from a first oxide. If an alloy between rhodium, platinum and/or iridium had formed (either during oxide formation or during decomposition), it is likely that reconstruction into an adsorption structure would have also been slowed down.

Most probably, the real desorption pathway contains a combination of these three hypothesis; unfortunately, since it was not possible to measure the contaminants amounts and stoichiometries at the same time as the spectra were acquired, we cannot go deeper with the analysis.

5.3.1.1 Mixed cycles

The second ageing recipe we tested is the mixed cycles one (see 5.2), consisting in a double oxidation at high and (relatively) low temperature. When designing it, we focused on the following targets:

1. To go one step further towards real catalysis (see fig. 5.7): this is why we chose a first oxidation step at $730\,^{\circ}\mathrm{C}$. In our specific case, we wanted to put oxygen in the subsurface region and this is also why we chose a temperature at which the rhodium mobility is extremely high.

2. Starting from the simple oxidation cycles, we were looking for a way to achieve the maximum shift of the TDS peak in the shortest time as

possible; from this point of view, the mixed cycles turned out to be a significant improvement.

As explained in section 5.2, in this recipe we acquired the TDS spectrum of each cycle after the second oxidation step, i.e. the one that yields a surface oxide[10].

In figure 5.11 the TDS spectra of a mixed cycles series, together with the evolution of the peak-maximum temperatures and integrals, are presented. The first clear characteristic is that the peak shift was as large as $\sim 60\,^{\circ}\mathrm{C}$, the highest value we ever obtained. Since only six mixed cycles were required to obtain such a shift, we can state that this recipe was effective in quick TDS evolution. Moreover, the changes in the spectra are smoother with respect to the previous case: this can be either due to the surface treatment at high temperature or simply to the short time range in which the experiments were performed.

The temperature of the peak maxima was almost linearly increasing as long as we proceeded with the cycles; this was also the case for the peak integrals, in a much more pronounced way than in the simple oxidation cycles.

The first oxide prepared prior to the cycles series had already a greater integral with respect to previous first oxides; this can be due to a mis-calibration through the $c(2 \times 8)$ structure in this case. However, the important result is the progressive increase of the oxygen amount desorbing from the surface: after 6 mixed cycles this quantity was higher by $\sim 20\%$ of the starting value. We propose two possible explanations for such a behaviour:

either with the high temperature oxidation step we were able to put some oxygen in the subsurface region (forming more than one trilayer or having oxygen dissolved into the metal),

or dosing in each cycle for $\sim (1\,\mathrm{hr} + 16\,\mathrm{min})$ we were accumulating more contaminants (also in their oxidized form) than in the simple oxidation cycles.

The explanation of the TDS spectra evolution follows the one proposed for the 20 oxidation cycles. The surface oxide desorption mechanism remains the same as for the first oxide (see chapter 4.3), but the pathway changes during the cycles: when the phase transformation of the oxide into the $c(2 \times 8)$ adsorption structure is hindered, more energy (i.e. a higher temperature) is required to

[10]Each cycle lasted about 2 hrs, and to minimize any background pressure influence we prepared 5 complete cycles within the same day. Before starting the cycles, a single oxide was prepared to check its TDS spectrum shape and temperature of the peak maximum.

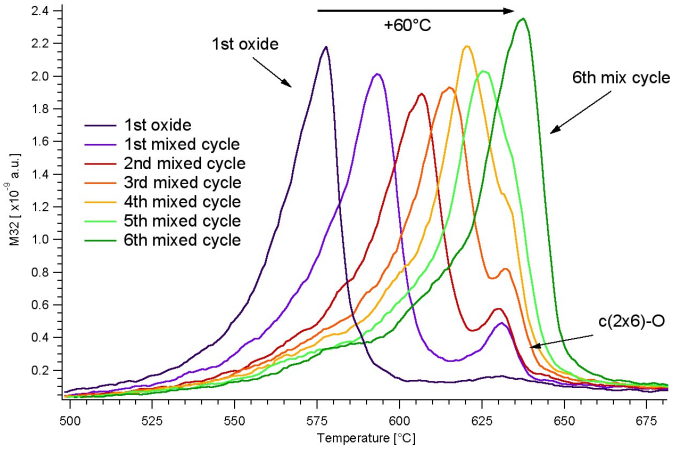

(a) TDS spectra

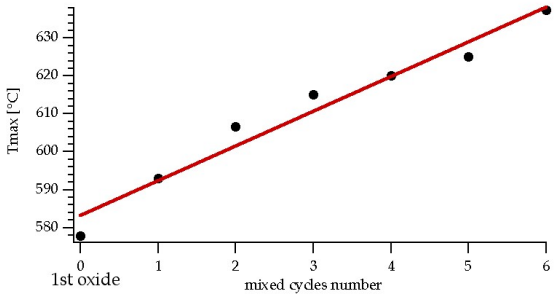

(b) oxides $8^{th} - 13^{th}$

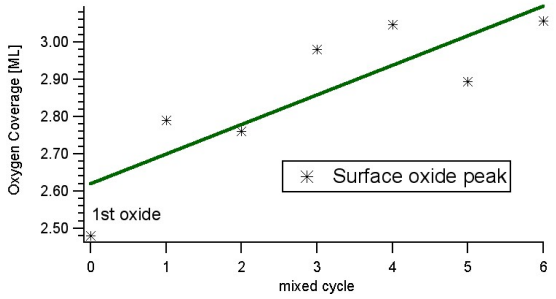

(c) oxides $14^{th} - 20^{th}$

Figure 5.11: a) TDS spectra of a first oxide followed by 6 mixed oxidation cycles; b) Prevailing peak maxima evolution during the cycles; c) Integrals evolution.

allow desorption. Thus the "dilute" phase, through which the oxide desorbs, shifts gradually from the $c(2 \times 8)$ to the $c(2 \times 6)$.

With respect to the simple oxidation cycles, we observed a more pronounced ageing effect after a shorter time: the main peak was shifted by $\sim 60\,^{\circ}\mathrm{C}$. In order to understand this, some considerations can be added:

- a higher contaminants quantity may have lead to more Pt and Ir oxides dissolving into the oxide, increasing the local oxygen coverage and so slowing down the phase transformation into the adsorption structures;
- dosing at $730\,^{\circ}\mathrm{C}$ may have caused subsurface oxygen accumulation, creating a buffer for the oxide;
- high temperature dosing may have also favored alloying between rhodium and the contaminants, creating a "complex" phase which needed higher temperatures to get decomposed.

5.3.2 Plasma source cycles

The second kind of source we used to oxidize our sample was the Microwave Plasma Source by Tectra, described in chapter 3.2.2. The cracking efficiency was lower than in the thermal cracker case ($\sim 6\%$ of O_{at} in the beam), but the operating pressure was higher ($p_{O_2} \sim 4 \times 10^{-6}\,\mathrm{mbar}$[11]), so to form an oxide we dosed $\sim 200\,\mathrm{L}$ of atomic oxygen. Despite this higher exposure, STM and TDS proved that the oxides were never complete: as will be shown in section 5.4.2, in most cases an oxygen vacancies network was already present on freshly prepared surfaces; the TDS integrals, moreover, always corresponded to coverages $\leq 2.0\,\mathrm{ML}$.

In figure 5.12 the TDS spectra of 12 consecutive oxidation cycles are presented: no evolution of the shape nor of the peak-maximum temperature was observed in this case. The integrals were slightly increasing during the cycles; nevertheless, their maximum value never exceeded $\sim 2.0\,\mathrm{ML}$. A possible reason for non stoichiometry of oxides is that CO and CO_2, which were unavoidably dosed together with oxygen, acted as reducing agents preventing the occupation of all the O sites in the trilayer. A second possibility (not alternative to the first one) is that the charged ions coming out from the source contributed to the incomplete oxide formation[12]. An oxide covered with the $c(2 \times 4)$ array of vacancies is then expected to be more easily converted into the $c(2 \times 8)$ adsorption structure than a complete oxide: according to equation 4.6, a lower

[11] It was the minimum value to ignite the plasma beam.

[12] See chap. 3.2.2; moreover, the measurements have been performed on a new crystal, which may have contained some carbon, therefore being less easily oxidized.

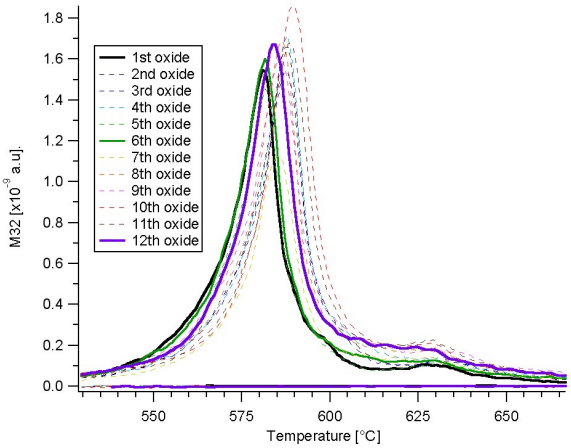

Figure 5.12: TDS spectra of 12 oxidation cycles performed with the microwave plasma source.

initial coverage speeds up the transformation of the "complex" into the "dilute" phase (see chap. 4.3). The ordered array of vacancies can favor the transition to the adsorption structure also in a more intuitive way: the defects leave free space for the reconstruction to build up. These facts can justify the slightly lower desorption temperatures with respect to the thermal cracker cycles, together with the fact that the oxides spectra looked always the same as long as we proceeded with the cycles. A second hypothesis is that, also due to the high density of oxygen vacancies, the ageing process was simply too slow to be detected within the number of iterations we performed.

5.3.3 Molecular oxygen cycles

Our next step towards real catalysis has been the setup of an oxidation cycle procedure that involved molecular oxygen only. For this purpose, we used the doser described in chapter 3.2.3, that allowed us to have up to $p_{O_2} \sim 10^{-4}$ mbar in front of the sample. Together with these extreme pressures -reaching the very limits of our UHV system- we increased the number of iterations up to more than 40, therefore significantly deviating from a standard surface science preparation.

To prepare a complete surface oxide we had to slightly modify the previous recipes, varying both the oxygen exposure and the sample temperature (see chapter 4.2.3). However, the molecular oxygen-based cycle was based on the simple scheme of the previous cases, consisting of an oxidation (at 400 °C) and a subsequent annealing.

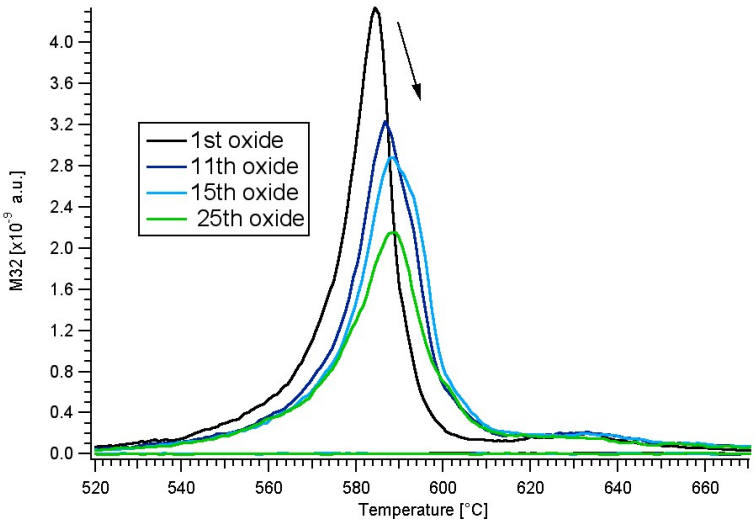

Figure 5.13: Molecular oxygen cycles: selected spectra from the first 25 oxides.

In laboratory ageing tests, catalysts undergo several tens of hours of operation, to better mimic what happens in real catalysis ([16–18]). To stick to this requirement, we performed more than 40 oxidation cycles; as a consequence, several TDS spectra were acquired on oxides that had been left overnight (of for a week-end) in UHV background. Since all these spectra were lower in intensity than the first oxide and backshifted, as already observed and explained (chap. 4.3), we removed them from the overall evolution analysis.
In this section a selection of significative spectra is presented, to discuss their evolution upon cycles iteration; additionally, in appendix B.2 we plot the entire oxidation series. An overview of selected spectra from the 1^{st} to the 25^{th} is plotted in figure 5.13. As the cycles proceed, we observe the following trends:

- the temperature of the maximum of the desorption peaks slightly shifts towards higher values, with respect to the first oxide;

- the peak integrals progressively decrease, reaching (for the 25^{th} oxide) less than $\sim 80\%$ of the first oxide value.

The peak shift is much smaller than in thermal cracker cycles, its maximum value being $\sim 9\,°C$; a tentative explanation for this behaviour will be discussed in the last section of this chapter. However, it is worth noting that the evolution

is slow but continuous, thus strongly suggesting a correlation with the cycles procedure.

As presented in chapter 4, with high pressure molecular oxygen dosing we were able to form thicker oxides, i.e. to grow more than one trilayer. Despite the fact that the integrals decrease with the cycles, even the lowest value (25^{th} oxide) corresponds to more than one complete trilayer. The lowering of the amount of oxygen desorbing from the surface was observed for the first time during the molecular oxygen cycles. Taking into account also the STM data (sec. 5.4.3), we attribute this behaviour to a progressive blocking of the active sites for O_2 dissociation.
With the aim of better understanding the oxides desorption mechanism, after the 15^{th} oxide we performed 3 partial TDS experiments: we annealed the oxides from 16 to 18 below the peak-maximum temperature; in other words, we always stopped prior to complete oxide decomposition. Afterwards, a second spectrum was acquired, up to 850 °C; therefore the surface was annealed twice up to $\sim$ 550 °C before the formation of the subsequent oxide. The images in figure 5.14 were acquired after the first annealing, in two different regions of the crystal: in the first one (images a–c) the oxide is still covering a major part of the surface. There are several monoatomic holes, and we can distinguish the $c(2\times8)$ adsorption structure on the holes bottom. Images d–f, on the other side, present a later stage of oxide decomposition[13]: the oxide and the $c(2\times8)$ occupy nearly the same portion of the surface, and the adsorption structure seems to enter into the oxide's terraces like the sea over a sandy beach. These data confirm that the trilayer surface oxide undergoes a phase transformation upon annealing, and that the "dilute" phase into which it is transformed is indeed the $c(2\times8)$. Moreover, we can state that the second assumption of the kinetic model described in sec. 4.3 is further validated by the results corresponding to the two different areas. In fact it says that –The "complex" phase can only decay via the "dilute" one–, meaning that regardless of the desorption stage, the oxide and the adsorption structure into which it is transformed are the only two phases present. On the other hand the third assumption, saying that the local coverage in the oxides islands is constant during decomposition, seems not to be totally confirmed by our measurements: as shown in figure 5.14f, the oxide region close to a phase boundary is completely covered by the oxygen vacancies network: this would mean that during desorption the local coverage within the "complex" phase islands is *not* constant. Anyway, this was not a general rule, as in the other images the oxide looked nearly complete in most cases.

[13]This can be simply attributed to slightly different temperatures reached by two separate regions on the sample.

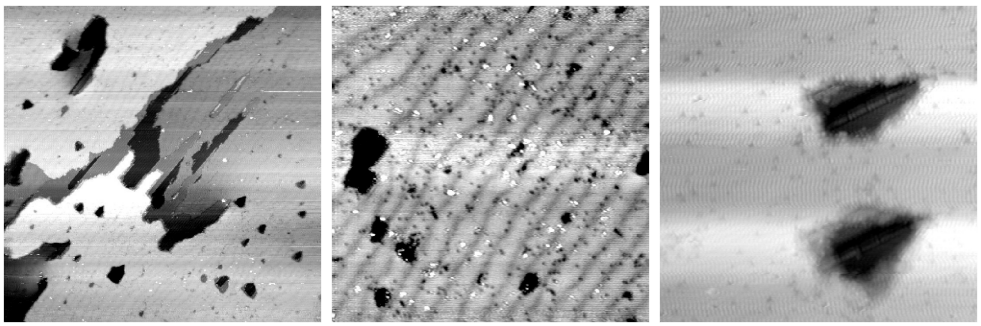

(a) (b) (c)

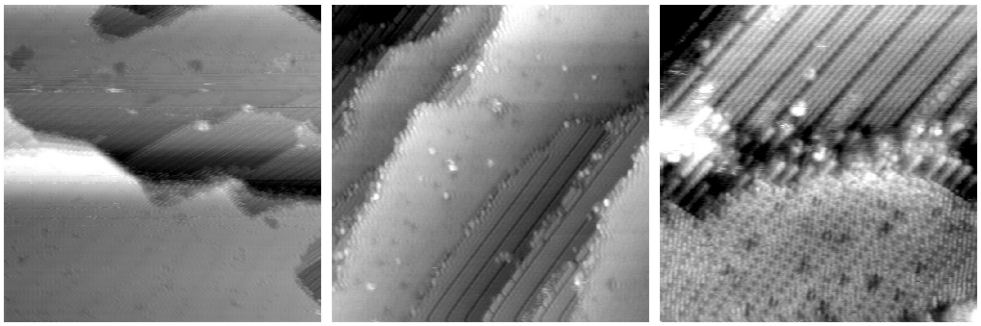

(d) (e) (f)

Figure 5.14: STM images of the 18^{th} oxide, annealed only up to 568 °C: we found two areas with different desorption stages: a)-c), d)-f). a) $(300 \times 300)nm^2$, $V = -0.3\,\mathrm{V}$, $I = 4\,\mathrm{nA}$; b) $(100 \times 100)nm^2$, $V = 0.3\,\mathrm{V}$, $I = 0.4\,\mathrm{nA}$; c) $(35 \times 35)nm^2$, $V = 0.3\,\mathrm{V}$, $I = 0.6\,\mathrm{nA}$; the brighter areas are an artifact due to the background subtraction, that was performed to allow the visibility of the $c(2 \times 8)$ structures on the holes' bottom. d) $(100 \times 100)nm^2$, $V = 0.4\,\mathrm{V}$, $I = 0.6\,\mathrm{nA}$; e) $(35 \times 35)nm^2$, $V = 0.3\,\mathrm{V}$, $I = 0.5\,\mathrm{nA}$; f) $(20 \times 20)nm^2$, $V = 0.3\,\mathrm{V}$, $I = 0.6\,\mathrm{nA}$.

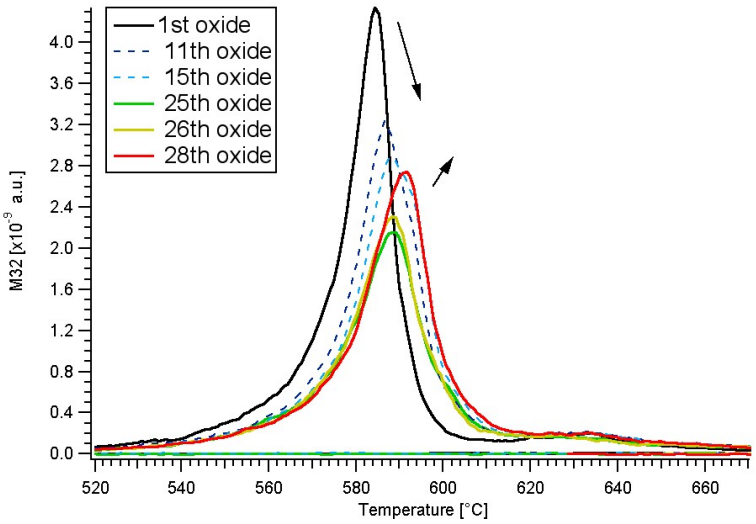

Figure 5.15: Molecular oxygen cycles: selected spectra up to the 28^{th} oxide.

After these partial TDS experiments, we observed an accelerated evolution of the oxides, from both the TDS and the STM point of view: the following oxides (fig. 5.13), in fact, presented lower peak integrals and disrupted oxides surfaces. Our hypothesis is that the responsible of the boosted ageing was the double annealing undergone by the surface up to $\sim 550\,^{\circ}\mathrm{C}$.

Based also on STM data (see also sec. 5.4.3), we thought that the peak integrals could be lowered by a hindered oxygen dissociation; therefore increasing the dosing pressure should have helped in recovering early oxides values. We therefore raised the background pressure by nearly $\sim +50\%$, close to our pumping system's limits: all the oxides starting from the 26^{th} were prepared with this maximum dose. Nevertheless, the 26^{th} oxide peak does not present a significantly increased integral, whereas the 28^{th} does, as shown in figure 5.15. The difference between these two cases can be traced back to the fact that after the 27^{th} TDS, slow annealings in UHV ambient were performed, which changed the (1×1) surface prior to oxide formation (see sec. 5.4.4). Hence the higher dosing pressure seems not to be the main ingredient of the observed integral increase. The inverted decreasing trend of the integrals, anyway, lasted only for a few cycles: as presented in figure 5.16, as long as we proceeded in the oxidations, we observed again a general decrease. This was accompanied by a progressive degrade of the oxides surfaces, and once more by a small but constant forward shift of the temperatures of the desorption maxima. Since we could not use higher oxygen pressures, we stopped the series after 46 cycles; the

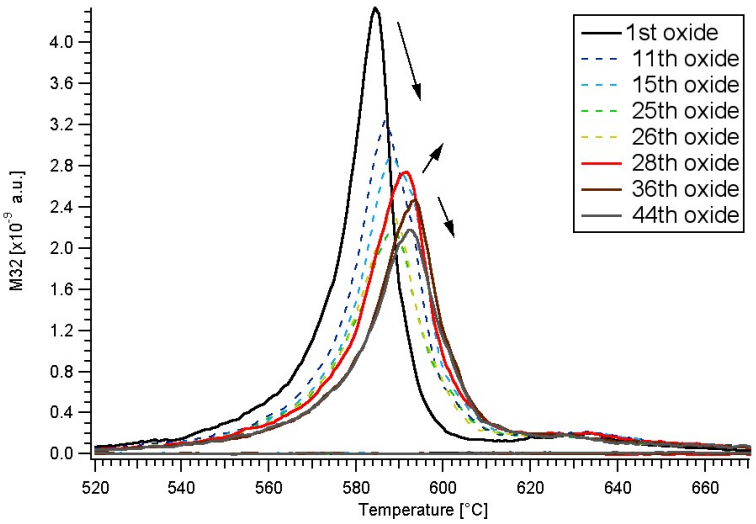

Figure 5.16: Molecular oxygen cycles: selected spectra up to the 44^{th} oxide.

number of iterations was fairly larger than in the previous experiments, and correspondingly provided very useful data to understand the ageing process. In the last two graphs (fig. 5.17) we summarize the changes in the integrals and in the temperatures of peak maxima; for the sake of clarity, we already removed the points corresponding to oxides which have been left in UHV for one night or more[14].
The first oxide we grew with molecular oxygen was thicker than any other one prepared with the previous atomic oxygen recipes (as discussed in chapter 4.2.3), its integral being more than 50% higher than for a single trilayer. This can be due to the high oxygen pressure used in this case, that allowed oxygen to enter deeply into the crystal. For this reason, even the lowest integral corresponded to a complete oxide, as confirmed by STM. We attribute the lowering to the progressive blocking of O_2 dissociation.

The forward shift of the peaks is the other TDS-detectable aspect of ageing. Even if it was considerably smaller than in the thermal cracker case, it followed a constant trend regardless of the oxygen pressure used.

[14]Or which have undergone partial annealings and titration reactions.

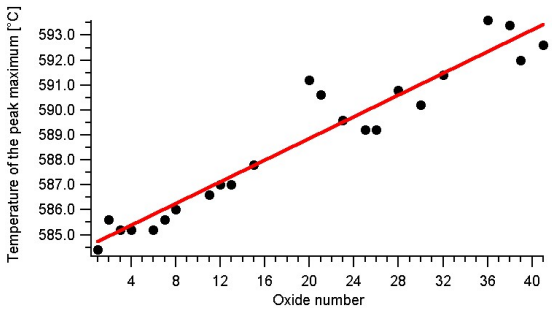

(a) T_{max}

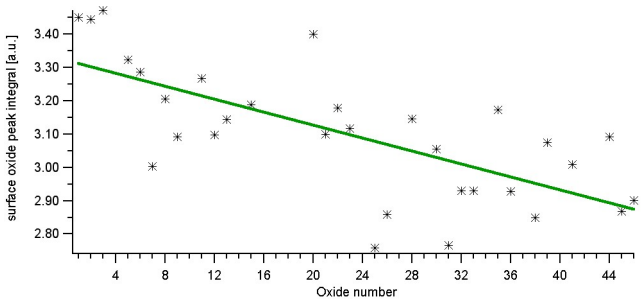

(b) *integrals*

Figure 5.17: a) Temperatures of the peak maxima within the molecular oxygen cycles; b) Integrals of the TDS spectra (up to 730 °C).

5.4 STM data: progressive ageing

In this section we present the STM images acquired during the different cycles measurements. They allowed us to monitor the ageing grade of our sample, on a $(5 \times 5)nm^2$ to a $(500 \times 500)nm^2$ scale. As will be shown at the end of this section, ageing traces remain on the (1×1) surface after TDS, and are fundamental to understand the overall behaviour during oxidation/annealing cycles. These traces will be discussed in chapter 6. Here the oxide morphology is presented.

5.4.1 Thermal cracker cycles

The formation of a complete surface oxide was attained by dosing 24 L of atomic oxygen at 350 °C, as already illustrated in chapter 4.2.3. The first oxide was flat,

with almost no oxygen vacancies and large (i.e. $\geq(100 \times 100)nm^2$) terraces[15]. In figure 5.18 we display six STM images, each one of a $(100 \times 100)nm^2$ area, referring to different stages during the 20 oxidation cycles (sec. 5.3.1). The

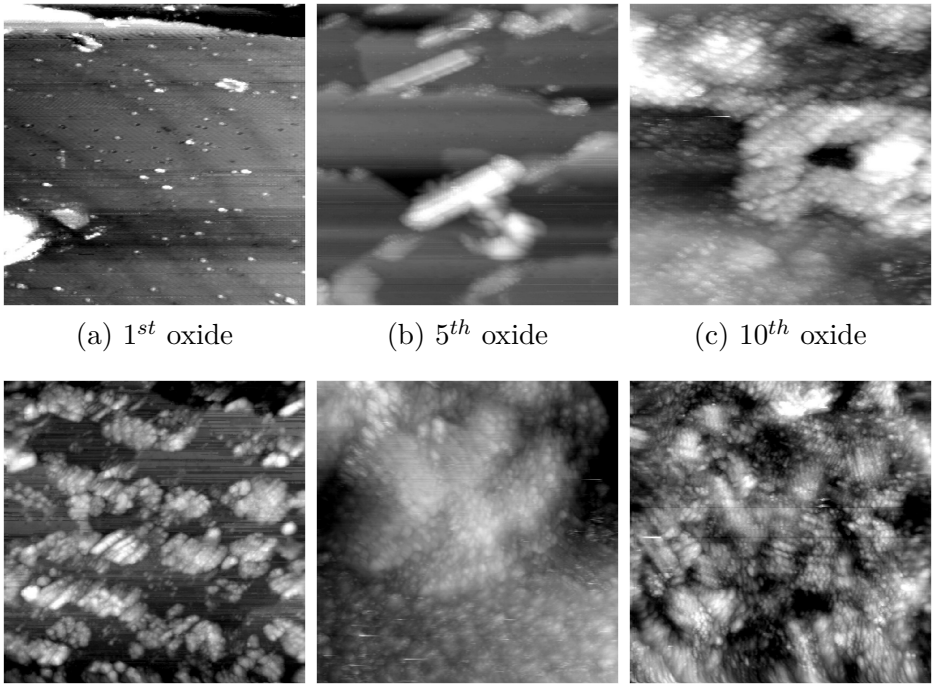

(a) 1^{st} oxide (b) 5^{th} oxide (c) 10^{th} oxide

(d) 12^{th} oxide (e) 16^{th} oxide (f) 18^{th} oxide

Figure 5.18: STM images of selected oxides during the thermal cracker oxidation cycles. Size: $(100 \times 100)nm^2$, a) $V = -0.35\,\mathrm{V}$, $I = 0.3\,\mathrm{nA}$; b)$V = -0.4\,\mathrm{V}$, $I = 0.6\,\mathrm{nA}$; c) $V = -0.3\,\mathrm{V}$, $I = 0.3\,\mathrm{nA}$; d) $V = -0.4\,\mathrm{V}$, $I = 0.6\,\mathrm{nA}$; e)$V = -0.5\,\mathrm{V}$, $I = 1\,\mathrm{nA}$; f)$V = 0.4\,\mathrm{V}$, $I = 1\,\mathrm{nA}$.

progressive changes in the surface morphology during the cycles are evident and huge. After only 4 cycles, the 5^{th} oxide looked decorated by some extra structures, whose density increased as long as we proceeded with the cycles. They start growing at steps but already on the 10^{th} oxide they partially cover also the terraces.
We can distinguish between elongated "bar-shaped" features (roughly aligned along the Rh crystallographic directions $[1\bar{1}0]$ and [001]) and more irregular, rounded ones (fig. 5.18d). In figure 5.19 we plot two images with line profiles

[15]The darker lines in figure 5.18 correspond to strain lines, already discussed in chapter 4.2.1.

across the extra structures: the apparent height of both, with respect to the surface oxide, is $\sim 0.6\,\text{nm}$, corresponding to several rhodium (and oxide) step heights. The rounded clusters lay on the terraces, while the elongated ones mainly grow at the steps.
It was not possible to achieve good resolution on them, because we had to scan at low speed over medium-large areas to avoid tip damaging. Moreover, we cannot exclude that the tunneling parameters used for imaging the oxide were not suitable to resolve such extra structures.
From the 16^{th} oxide on, it got even harder to distinguish what is buried below these extra structures, i.e. to see the oxide's surface. Nevertheless, we know that the oxide is still formed by means of two other techniques: LEED[16] and TDS; in this second case, the oxide peak was always recognizable, even if it indicated a progressively different desorption pathway (see sec. 5.3.1). After the 12^{th} cycle, it got very rarely possible to image the oxide areas between the new features; in these cases, however, we detected some bright little dots, circled in red in figure 5.20; we named them "specks" because they look bright and rounded and, as a general trend, their density was found to increase with the number of oxidation cycles. As a matter of fact, we see also some oxygen vacancies (dark triangular features, circled in yellow) in this last image. However, they are only a few and randomly distributed, i.e. not organized in the $c(2 \times 4)$ network.

Since we know from XPS data (sec. 5.1) that Pt and Ir contamination, stemming from the thermal cracker, was present on the surface, we identify the "bar-shaped" and the rounded extra structures as oxidized platinum and iridium clusters. The most probable scenario is that core-shell clusters were deposited on rhodium, the core being metallic and the shell oxidized. Nevertheless, we cannot exclude some alloy formation, not only between platinum and iridium but also together with rhodium. The maximum coverage calculated from XPS spectra was $\sim 7\%$ for Pt and $\sim 1.5\%$ for Ir, while in the latest oxides the surface looked almost completely covered by the clusters in the STM images. There are two possible explanations for the discrepancy:

either the clusters are not only composed of Pt and Ir but also of Rh,

or the recipe followed at the SuperESCA beamlime did not produce as many of them as in the STM case.

Since at the beamlime we only performed 3 mixed cycles, and the source was

[16]LEED images showed a progressive increase of the background intensity, indicating a less homogeneous surface. No extra spots were detected that could have been attributed to the new structures: this suggests that they do not have a precise crystal structure.

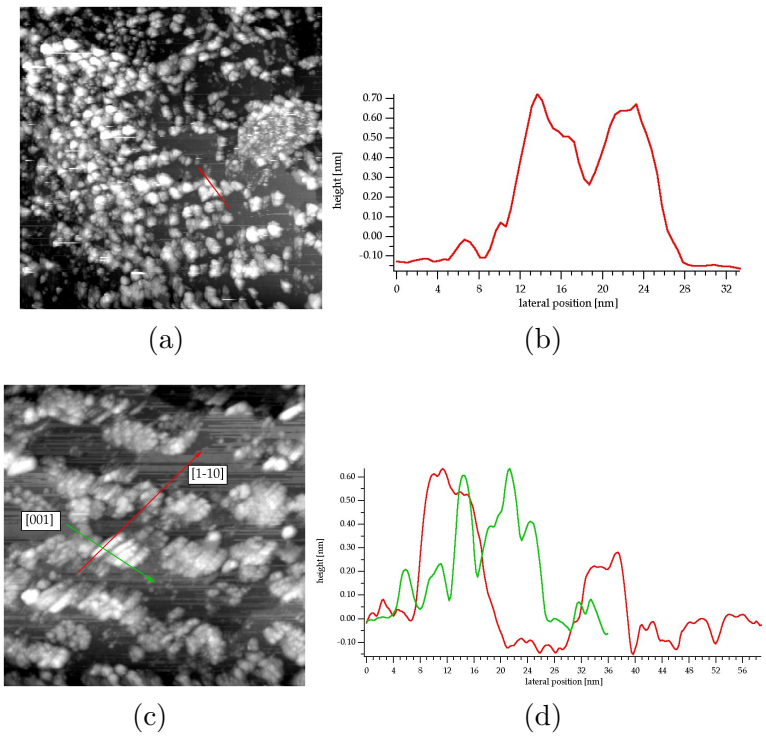

(a) (b)

(c) (d)

Figure 5.19: STM images of the 12^{th} oxide, showing the different kind of clusters Size: $(200 \times 200)nm^2$, a) $V = -0.4\,\mathrm{V}$, $I = 0.6\,\mathrm{nA}$; b) image line profile along the line in a); c) $V = -0.4\,\mathrm{V}$, $I = 0.6\,\mathrm{nA}$; d) image line profiles along the lines in c).

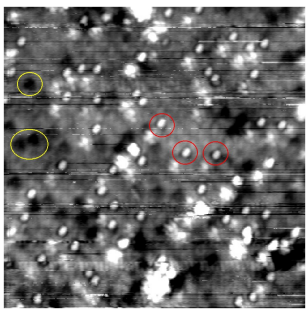

Figure 5.20: Surface oxide small area of a 16^{th} oxide: some little “specks" (circled in red) are visible inside the trilayer’s structure. Size: $(20 \times 20)nm^2$, a) $V = -0.4\,\mathrm{V}$, $I = 1\,\mathrm{nA}$.

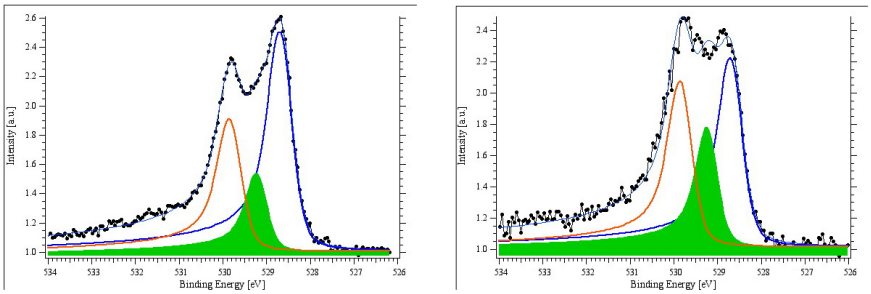

(a) 1^{st} oxide (b) 2^{nd} mixed cycle

Figure 5.21: O1s spectra of a first oxide and a 2^{nd} mixed cycle one. To grow the first oxide the atomic oxygen source was operated for only ~ 15 min; therefore any contaminant presence was below our detection limit, and we can assume that this spectrum was free of contaminants influence.

twice as far from the sample with respect to our UHV chamber, the different mounting geometry seems to be the best hypothesis; anyway, both of them can hold at the same time.

Another evidence of the contaminants-driven ageing could be found in the XPS O1s spectra. As presented in chapter 4, thanks to the capabilities of the SuperESCA beamline we were able to distinguish two (out of three) components related to oxygen at the interface, plotted in orange and green in figure 5.21. After only two mixed cycles we observed a relative increase of the green component together with a decrease of the surface one (in blue): this is an indication that the state of the oxygen at the interface has changed.
When performing the mixed cycles series, after 5 cycles we acquired STM measurements on the 6^{th} oxide, presented in figure 5.22, observing the same features already detected during the single cycles series. In fact, we could distinguish both extra clusters (a) and, on the free oxide terraces, the little "specks" (b, circled in red).

5.4.2 Plasma source cycles

In chapter 4.2.3 we already pointed out that an oxide prepared with the Tectra microwave plasma source[17] contained a high density of oxygen vacancies

[17] described in chapter 3.2.

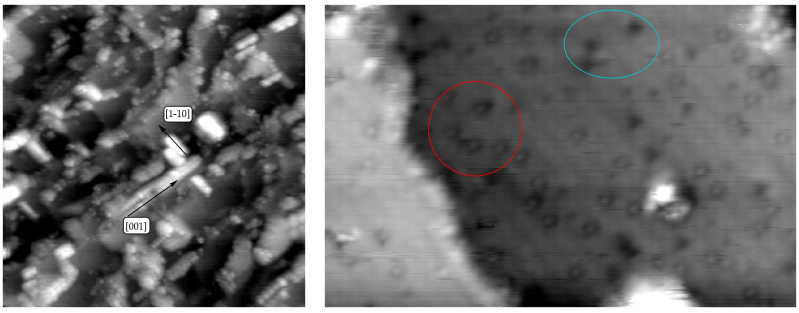

(a) (b)

Figure 5.22: STM images of an oxide prepared at the end of a 6^{th} mixed cycle; a) $(80 \times 80)nm^2$, $V = 0.6\,\mathrm{V}$, $I = 1\,\mathrm{nA}$; b) $(16 \times 25)nm^2$, $V = 0.5\,\mathrm{V}$, $I = 1.2\,\mathrm{nA}$: the red circle encloses some of the ageing seeds candidates, while the light blue one contains some oxygen vacancies.

arranged in the $c(2\times4)$ network, as shown in figure 5.23. This was also observed when performing the oxidation cycles series, i.e. all the oxides were rich in vacancies already after dosing.

In figure 5.24 three images of the 1^{st}, 6^{th} and 12^{th} oxide are shown. It is immediately clear that no morphology evolution could be detected during this series: in fact the oxides remained flat, with the same terrace width and shape as the first one and without any extra structure growing above them. This further suggests that the clusters seen after operating the thermal cracker could have been made of contaminants.
There are two possible reasons why we did not observe any evolution of the oxides grown with the plasma source neither in the TDS spectra of this series nor in the STM images:

either an incomplete oxide simply can never "get old";

or an incomplete oxide, upon annealing, forms much less "ageing nuclei" with respect to a complete one and therefore 12 cycles could have simply been too few to detect any morphology evolution[18].

[18] As will be discussed in chapter 6, we believe that the ageing seeds are created during the oxides deconstruction, and we did not observe them after annealing the oxides grown with the plasma source

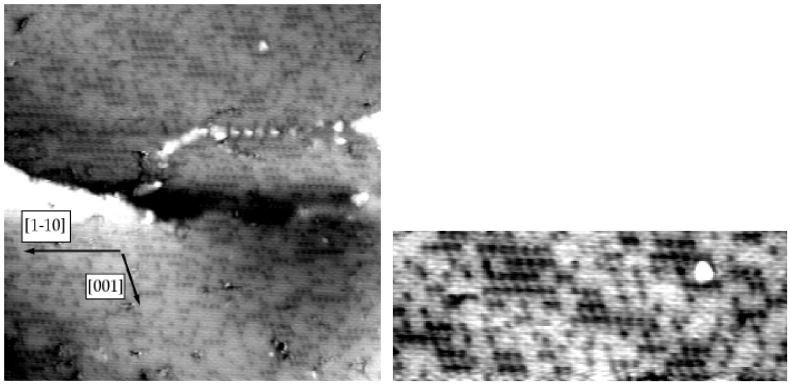

(a) (b)

Figure 5.23: STM image of a first oxide obtained by operating the plasma source, $(35 \times 35)nm^2$ $V = 0.3\,\mathrm{V}$, $I = 0.4\,\mathrm{nA}$; b) zoom on oxygen vacancies $c(2\times4)$ network, $(8 \times 22)nm^2$. With respect to other measurements, the crystal was rotated: main cristallographic directions are thus indicated.

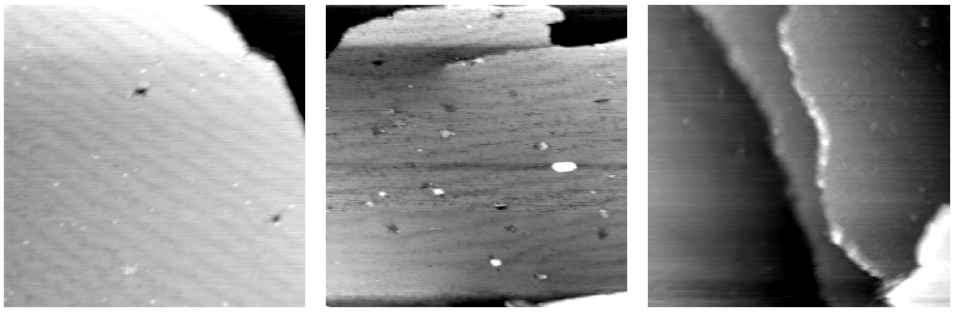

(a) 1^{st} oxide (b) 6^{th} oxide (c) 12^{th} oxide

Figure 5.24: STM images acquired during the plasma oxidation cycles; a) $(100 \times 100)nm^2$, $V = 0.6\,\mathrm{V}$, $I = 0.6\,\mathrm{nA}$; b) $(100 \times 100)nm^2$, $V = 0.4\,\mathrm{V}$, $I = 0.8\,\mathrm{nA}$; c) $(50 \times 50)nm^2$, $V = 0.5\,\mathrm{V}$, $I = 0.8\,\mathrm{nA}$.

5.4.3 Molecular oxygen cycles

In this section we describe the evolution of the oxides morphology that has been observed during the 46 molecular oxygen cycles. We want to remark, once more, that this series has been the crucial one to monitor and understand the ageing phenomenon, for the following reasons:

First, because using high pressure molecular oxygen represented a step towards real catalysis with respect to all the previous preparations;

second, because with this settings we were able not only to form complete (and thick) oxides, but also to avoid source-related contaminants.

Last but not least, we performed quite a high number of iterations, therefore having the possibility to detect huge changes in the oxides.

A comparison between the first oxides grown with the different recipes has been presented in chapter 4.2.3: STM images and TDS integrals values suggested that with molecular oxygen we made thicker oxides, i.e. more than one trilayer was grown at least on some surface areas.

In figure 5.25 we present a large scale overview of selected oxides, to enlighten the evolution of the step heights during the cycles. What we observe is that the step bunches present on the first oxide (figure 5.25a) progressively level off: the average step height is never higher than 2 oxide layers from the $\sim 20^{th}$ oxide on. Moreover, this is accompanied by clear morphology changes also on the terraces: the most disrupted oxides (like the 27^{th} in fig. 5.25c) are full of holes one to two layers deep.

In figure 5.26 we show a large and medium-scale overview of the first and tenth oxide, which at a first glance are quite similar. However, some traces of evolution can already be recognized by their comparison: in the central part of image 5.26c we can see three steps with a finger-like shape, and in 5.26d a (10 layers deep) hole in the middle of an oxide terrace. These two features are part of the ageing phenomenon, as will be shown below.

The oxides from the 16^{th} to the 18^{th} were annealed up to $\sim 550\,^{\circ}$C-$570\,^{\circ}$C to desorb the oxide only partially. This was done to fully confirm the trilayer's desorption mechanism described in chapter 4.3, i.e. the fact that the oxide transforms into the $c(2 \times 8)$ structure (see section 5.3.3).

A second outcome of these experiments, which was partially unexpected, was that by performing partial TDS we significantly speeded up the ageing process, and facilitated its comprehension.

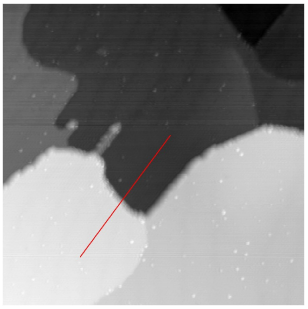

(a) 1^{st} oxide

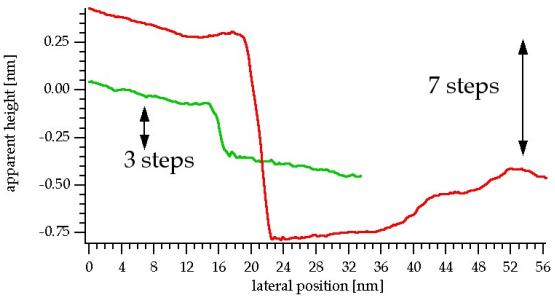

(b)

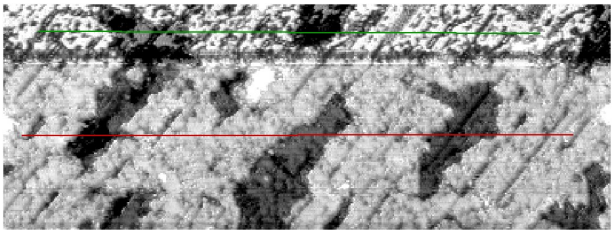

(c) 27^{th} oxide

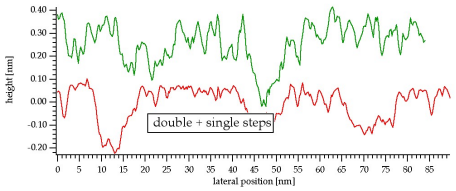

(d)

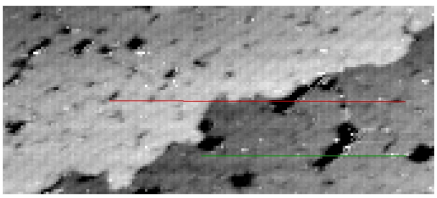

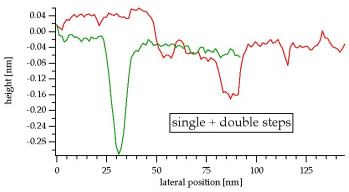

(e) 37^{th} oxide (f)

Figure 5.25: STM images and corresponding line profiles of a) 1^{st} oxide,$(100 \times 100\,)nm^2$, $V = 0.4\,\mathrm{V}$, $I = 0.7\,\mathrm{nA}$; b) line profile across the line in a); b) 27^{th} oxide, $(35 \times 130\,)nm^2$, $V = -0.4\,\mathrm{V}$, $I = 0.4\,\mathrm{nA}$; c) line profiles across the lines in b); d) 37^{th} oxide, $(90 \times 210\,)nm^2$, $V = 0.4\,\mathrm{V}$, $I = 0.4\,\mathrm{nA}$; e) line profiles across the lines in d).

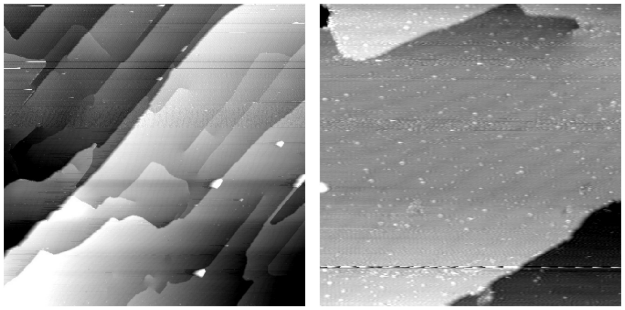

(a) 1^{st} oxide (b) 1^{st} oxide

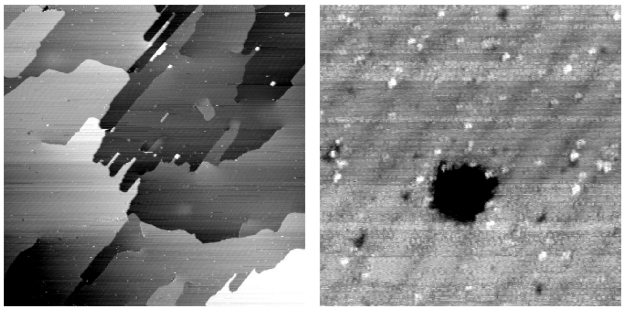

(c) 10^{th} oxide (d) 10^{th} oxide

Figure 5.26: a) 1^{st} oxide,$(500 \times 500)nm^2$, $V = 0.4\,\mathrm{V}$, $I = 0.6\,\mathrm{nA}$; b) 1^{st} oxide, $(100 \times 100)nm^2$, $V = 0.4\,\mathrm{V}$, $I = 0.8\,\mathrm{nA}$; c) 10^{th} oxide, $(500 \times 500)nm^2$, $V = 0.4\,\mathrm{V}$, $I = 0.7\,\mathrm{nA}$; d) 10^{th} oxide, $(50 \times 50)nm^2$, $V = 0.4\,\mathrm{V}$, $I = 0.7\,\mathrm{nA}$.

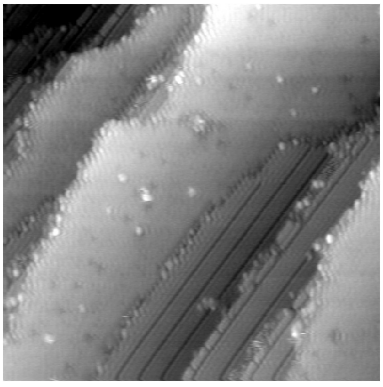

Figure 5.27: Small scale STM image of the surface obtained after a partial annealing up to 568 °C, $(35 \times 35)nm^2$, $V = 0.3\,\mathrm{V}$, $I = 0.5\,\mathrm{nA}$

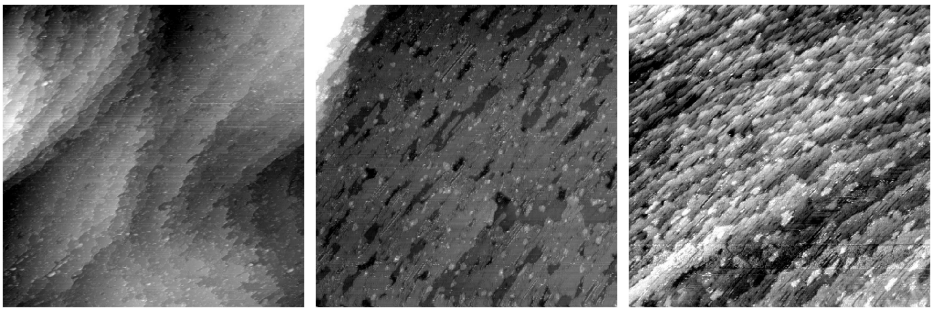

(a) 22^{nd} oxide (b) $24^{th}oxide$ (c) 27^{th}oxide

Figure 5.28: Large scale STM images of a) 22^{nd} oxide: $(500 \times 500\,)nm^2$, $V = -0.4\,\mathrm{V}$, $I = 0.2\,\mathrm{nA}$; b) 24^{nd} oxide: $(300 \times 300\,)nm^2$, $V = 0.3\,\mathrm{V}$, $I = 0.4\,\mathrm{nA}$; c) $(200 \times 200\,)nm^2$, $V = -0.4\,\mathrm{V}$, $I = 0.4\,\mathrm{nA}$.

The surface in figure 5.27 was obtained after annealing the 18^{th} oxide up to 568 °C: we notice that both steps (of the adsorption structure and of the oxide) and domain boundaries between the two are decorated with several small bright spots. These species were found to accumulated with cycles[19]: we already named them "specks", and we think that they block O_2 dissociation during growth, therefore being responsible for the morphology changes in the oxides.

After the partial TDS experiments, we observed a much faster decrease in the peaks integrals, together with a rapid worsening of the oxide structure. The following figures contain a large, medium and small scale overview of the oxides from 22^{nd} to 27^{th}. They were all prepared in the same way except for the last one: in fact, trying to solve the problem of peak integrals decrease, from the 26^{th} oxide on we dosed using our maximum pressure ($p_{O_2} = 1 \times 10^{-5}$ mbar in the chamber, see sec. 5.3.3). Nevertheless, the 27^{th} oxide was the most aged we ever observed: therefore the increase of the oxygen pressure seemed not be the main ingredient for retrieving a flat and ordered oxide.

Large scale images (fig. 5.28) show mainly that the step shape is progressively changing as long as we increase the number of cycles: compared to earlier oxides, steps became more and more "finger-like", or "fringed". When we look at areas of $(100 \times 100\,)nm^2$ (fig. 5.29), more ageing features become evident: first the number of holes is increasing, and secondly their width. It is worth noting that these holes resemble the ones observed after the partial annealing (figure 5.14), but in this case we have oxide also on their bottom; this is also

[19] Also in the thermal cracker cycles, on the oxides areas not covered with the clusters.

confirmed by the peak integrals, which never fell below the oxygen quantity corresponding to a complete trilayer.

Finally, if we zoom in (fig. 5.30), we can distinguish the "specks" decorating almost every step, both at terraces borders and holes ones. Moreover, they seem to organize into a zig-zag structure when two steps are facing each other. Their accumulation was boosted after the partial annealing experiments, suggesting that they require oxide formation/decomposition to be formed. We think that during the oxide formation, when mass transport occurs, they diffuse on the surface; when they got stuck and accumulate in some sites (e.g. at steps), they hinder molecular oxygen dissociation and, as a consequence, a perfect trilayer growth.

5.4.4 Partial oxides recovering

Despite what we have presented up to now, we were able to form some "recovered" oxides after the 27^{th} one: these oxides had slightly increased peak integrals and especially much less disrupted surfaces. The increased oxygen dosing pressure could have helped in growing better oxides. Nevertheless, this cannot be the only explanation: in fact, the 27^{th} oxide presented the most poisoned surface even if it was already prepared with the limit values.

Trying to understand the oxides' ageing causes, we studied the (1×1) surface obtained after acquiring a TDS spectrum: figure 5.31a refers to the surface after the 27^{th} cycle. What we immediately notice is that there is quite a high density ($\sim 6\%$ ML) of bright features, surrounded by a trialgular dark rim, thereon called "units" (or ageing fingerprints). Their structure and behaviour upon oxidation cycles will be discussed in chapter 6.

From our data, we are able to trace back the quality of an oxide (prepared with O_2) to the density of "units" that is present on the (1×1), more than from the quantity of "specks" detected on the previous oxide. While the image on the left in figure 5.31 is the surface observed after annealing the 27^{th} oxide[20], the one on the right is the one over which the 28^{th} oxide was grown. To reach the second situation, a series of slow annealings in UHV ambient between $\sim 250\,°C$ and $\sim 400\,°C$ have been performed.

In figure 5.32 we present an overview of two oxides, which have both been grown on a (1×1) with very few ageing fingerprints. The 29^{th} oxide looks much different from the 27^{th}: the steps are still a bit rounded, but there are very few holes and their extension is several times smaller than for the aged

[20]But we can reasonably assume that we already had such an amount before dosing the 27^{th} oxide itself.

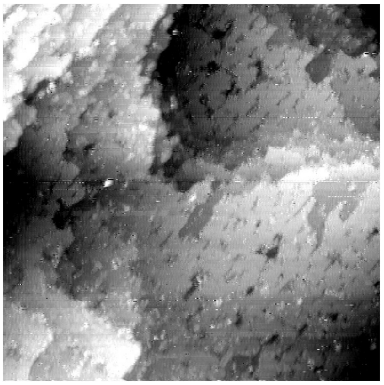

(a) 22^{nd} oxide

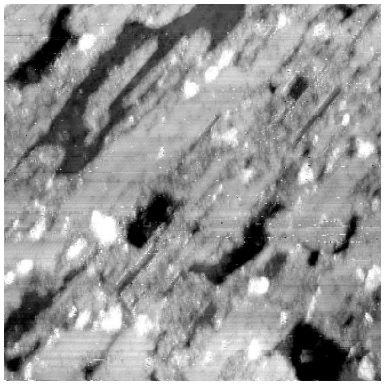

(b) $24^{th}oxide$

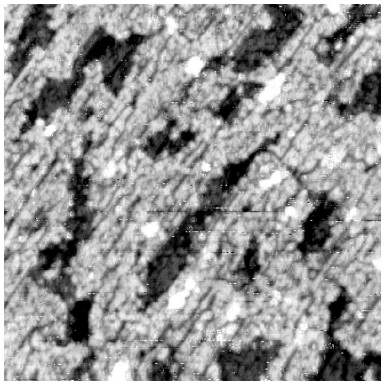

(c) 27^{th}oxide

Figure 5.29: Medium scale STM images of a) 22^{nd} oxide: $(500 \times 500\,)nm^2$, $V = -0.3\,\mathrm{V}$, $I = 0.4\,\mathrm{nA}$; b) 24^{th} oxide: $(300 \times 300\,)nm^2$, $V = 0.3\,\mathrm{V}$, $I = 0.4\,\mathrm{nA}$; c) 27^{th} oxide: $(200 \times 200\,)nm^2$, $V = -0.4\,\mathrm{V}$, $I = 0.5\,\mathrm{nA}$.

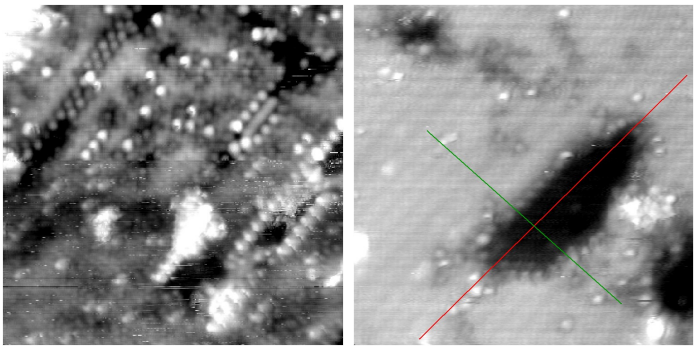

(a) 27^{th}oxide (b) 31^{st}oxide

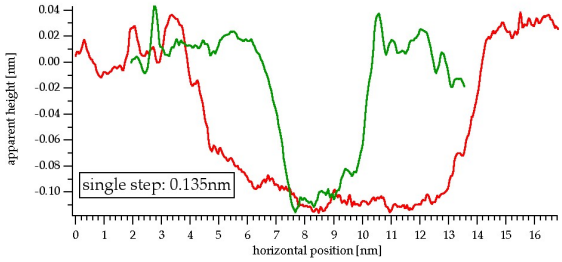

(c) 31^{st}oxide

Figure 5.30: Small scale STM images of a) 27^{th} oxide: $(15 \times 15)nm^2$, $V = 0.4\,\mathrm{V}$, $I = 0.4\,\mathrm{nA}$; b)-c) 31^{st} oxide: $(15 \times 15)nm^2$, $V = 0.3\,\mathrm{V}$, $I = 0.8\,\mathrm{nA}$ and line profiles along the lines in b).

oxides (cfr with fig. 5.29c). Moreover, also the number of "specks" is much lower, and we could find several oxide areas which looked complete, like on a first oxide (fig. 5.32b). The same holds for all the oxides, like the 37^{th}, which were grown on surface with a very small number of "units": therefore their density seems to be a crucial parameter in the ageing process.

Except for the surfaces obtained after the 27^{th} and in a few other cases, we never tried again to reduce the density of ageing fingerprints on the (1×1) surface. As a consequence, we slowly accumulated them in all the cycles from the 29^{th} to the end (46^{th}). In figure 5.33 we present some images of the latest oxides in our series: we progressively observed the re-appearance of larger holes, together with step shape changes towards more involute contours. This is coherent with the TDS evolution of the spectra corresponding to these oxides (fig. 5.16): in fact a decreasing trend of the integrals was observed, suggesting an unavoidable progressive ageing.

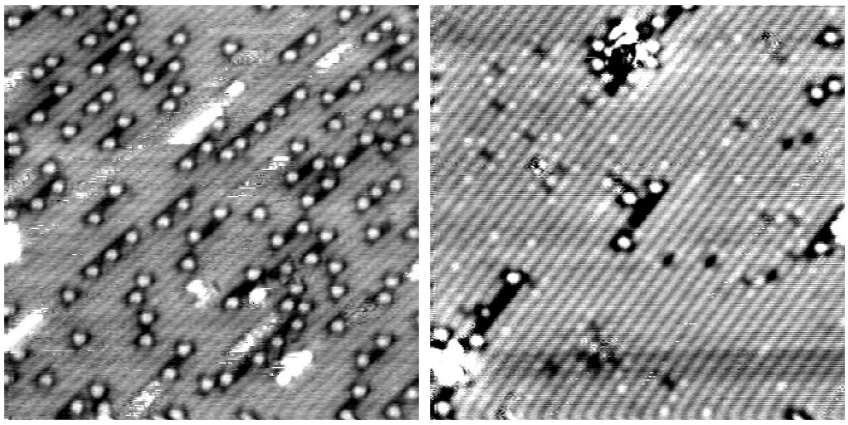

(a) (b)

Figure 5.31: STM images of the (1×1) surface obtained after desorption of the 27^{th} oxide: a) $(15 \times 15)nm^2$, $V = 0.4\,\mathrm{V}$, $I = 0.8\,\mathrm{nA}$; b) surface obtained after several annealing of the a) surface in UHV, with many less"units" $(15 \times 15)nm^2$, $V = 0.4\,\mathrm{V}$, $I = 0.6\,\mathrm{nA}$.

After these oxidation series, it was not possible to recover our sample, i.e. to obtain a "unit"-free surface with straight steps, unless after several cleaning cycles including sputtering and high temperatures annealing.

5.5 Ageing mechanisms

In this section we summarize and analyze the ageing of the surface oxides that was observed during the cycles, highlighting the common ingredients and the differences.

The thermal cracker cycles were strongly influenced by the presence of Pt and Ir contaminations; in fact, we can explain the modifications in both surface structure and desorption spectra with the deposition and decomposition of clusters stemming from the atomic oxygen source.

The molecular oxygen cycles represented a benchmark for studying the ageing processes, because only O_2 was used and because a large number of iterations were performed. For these reasons they were closer, with respect to the other recipes, to what happens in real-catalysis oxidation.

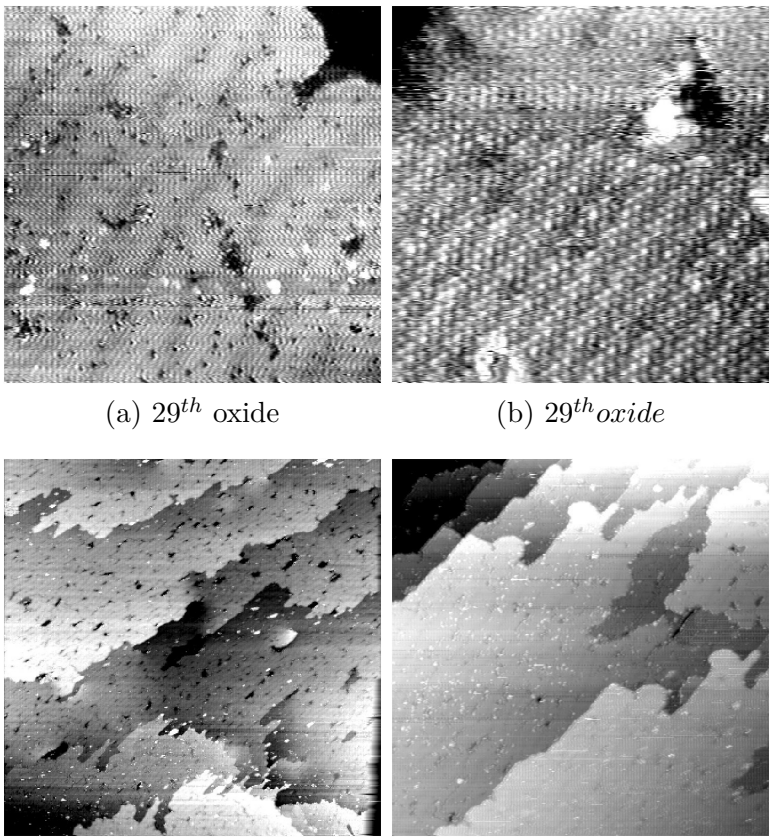

(a) 29^{th} oxide (b) $29^{th} oxide$

(c) 37^{th}oxide (d) 37^{th}oxide

Figure 5.32: STM images of two partially recovered oxides, which were grown on (1×1) surfaces with only a few ageing fingerprint (in the outermost layers) a)29^{th} oxide: $(50 \times 50\,)nm^2$, $V = -0.4\,\mathrm{V}$, $I = 0.6\,\mathrm{nA}$; b) $(10 \times 10\,)nm^2$, $V = 0.35\,\mathrm{V}$, $I = 0.8\,\mathrm{nA}$; c) $(500 \times 500\,)nm^2$, $V = 0.4\,\mathrm{V}$, $I = 0.6\,\mathrm{nA}$; d) $(200 \times 200\,)nm^2$, $V = 0.4\,\mathrm{V}$, $I = 0.6\,\mathrm{nA}$ and line profiles along the lines in d).

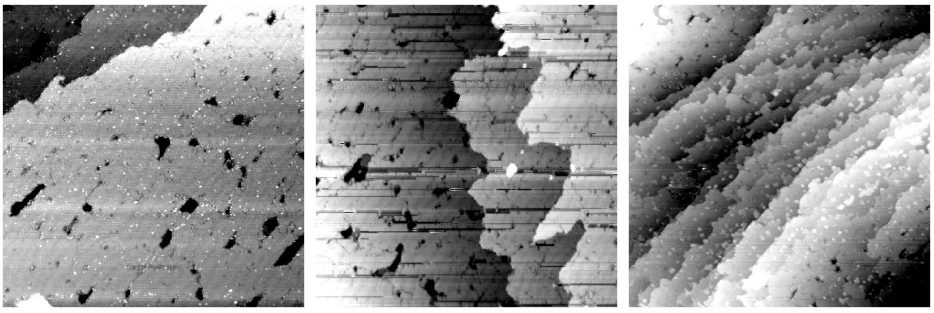

(a) 32^{nd} oxide (b) $35^{th}oxide$ (c) 45^{th}oxide

Figure 5.33: STM images of the last oxides in the series a) 29^{th} oxide: $(200 \times 200)nm^2$, $V = -0.4\,\mathrm{V}$, $I = 0.6\,\mathrm{nA}$; b) $(200 \times 200)nm^2$, $V = -0.4\,\mathrm{V}$, $I = 0.4\,\mathrm{nA}$; c) $(300 \times 300)nm^2$, $V = 0.4\,\mathrm{V}$, $I = 0.4\,\mathrm{nA}$.

During the plasma source cycles, on the other hand, no evolution was observed. This can be traced back to the non-stoichiometric (rich in oxygen vacancies) oxides that were grown.

In our measurements, we were able to detect three features that underwent evolution during the cycles: the TDS peak maxima, their integrals and the oxide surface morphology. The temperature of the peak maxima was observed to shift towards higher values, while the variation in the oxygen quantity desorbing from the surface (i.e. the peak integrals) showed a slight increase when using the thermal cracker and a pronounced decrease when using molecular oxygen. The changes in the surface morphology also depended on the oxygen source used.

Nevertheless, one of the most interesting results of this thesis work is that we found at least two *common* ageing aspects between the thermal cracker and the molecular oxygen cycles:

the shift towards higher temperatures of the maximum of the oxide desorption peak: it was as large as $\sim 60\,^{\circ}\mathrm{C}$ when using the thermal cracker and of $\sim 9\,^{\circ}\mathrm{C}$ when using molecular oxygen;

the presence and accumulation, on the oxides, of the little "specks", despite the very different surface morphology in the two cases. Their origin will be discussed in chapter 6.

In the molecular oxygen case, the TDS peak shift can be explained in two ways, which are both due to the accumulation of the "specks". Either their presence inhibits the oxides' deconstruction, thus requiring a slightly higher temperature for the desorption to reach its maximum or, since oxygen leaves the surface as O_2, they block some of the active sites for oxygen recombination, thus causing the temperature shift.

We think that the "specks"[21] are also responsible for the progressive disruption of the trilayers (and for the lowering of the TDS peak integrals): they hinder O_2 dissociation, therefore poisoning the oxides' growth.

On the other side, even if we were able to detect the "specks" also on the aged thermal cracker oxides, we could not see any oxide damage due to O_2 dissociation blocking in this case, because dosing atomic oxygen we simply overcome this reaction step. For this reason, the oxides patches that we observed between the contaminants clusters were always complete, and the peak integrals were even increasing as long as we proceeded with the cycles. This supports our hypothesis that the disruption observed during the molecular oxygen cycles was due to a hindering of the O_2 dissociation.

The shift of the desorption peaks of the thermal cracker oxides can be explained in three ways, all depending on the contaminants (see section 5.3.1). One of them is remarkably similar to the first hypothesis we exposed for the O_2 cycles: Pt and Ir single atoms can mechanically hinder the conversion of the oxide into the $c(2 \times 8)$ adsorption structure. We had the "specks" also on these oxides, but it is clear that the contaminants slowed down the phase transformation process much more than what happened in the molecular oxygen case.

Finally, the main results of all the oxidation cycles that we performed are the following:

The oxides desorption mechanism was found to be always the same, regardless of the source used and of the number of iterations: what was changing during the cycles was indeed the desorption *pathway*: upon ageing, the oxide was no more converted into a bare $c(2 \times 8)$ adsorption structure to allow desorption, but instead, in a progressively greater portion, into the $c(2 \times 6)$ structure.

From the analysis of the molecular oxygen cycles and from the detailed comparison with the other cases, we were able to define and understand the ageing process. With the help of what will be shown in chapter 6;

[21] As well as the "units", from which they probably derive (see chapter 6).

moreover, we can suggest a double definition for the ageing: "contaminants driven" *versus* "intrinsic" one. The first was evident in the thermal cracker cycles. The intrinsic ageing, on the other hand, showed up clearly during the molecular oxygen cycles but, even if partially hidden, was present also in the thermal cracker case.

The former was observed in the thermal cracker cycles, while the latter was present not only in the molecular oxygen cycles, but also in the contaminated case, being somehow hidden by the use of atomic oxygen and by the contaminants presence.

We proved that the ageing can be, at least partially, reversible: by decreasing the density of the ageing fingerprints, in fact, we could grow oxides with a morphology closer to the one of the 1^{st} oxide than to those of the disrupted ones.

Chapter 6

The units: fingerprints of ageing

At the end of the previous chapter we summarized the oxides' ageing features detected during the cycles. We have identified two new species which are thought to be responsible for the ageing: we named them "specks" and "units", the first laying on the oxides while the second were found on the (1×1) surface.

We believe that the two species are one derived from the other, based on the considerations listed below:

as shown in figure 6.1 their lateral size is the same; they both appear as a bright, rounded central spot enclosed in a dark rim, less visible on the oxide. The "specks" present a circular rim, while the "units" shown a triangular one;

they were both observed when performing oxidation cycles, and they were accumulated during the thermal cracker and the molecular oxygen series.

Based on the STM data described in section 5.4.4, we could establish a direct correlation between the oxides quality and the density of "units" that are present on the (1×1) surface over which the oxide is formed: therefore these are the ageing fingerprints we focused on. In this chapter we first analyze in detail their structure and we present their behaviour during different cycles and preparations. Then we discuss some old STM data in which they were already present. In the end we expose our hypotheses on their identity: these species seem to be *intrinsic*, i.e. not due to contaminations. Unluckily we cannot provide such a detailed analysis about the "specks", but they can anyway be regarded as -units *on* the oxide-.

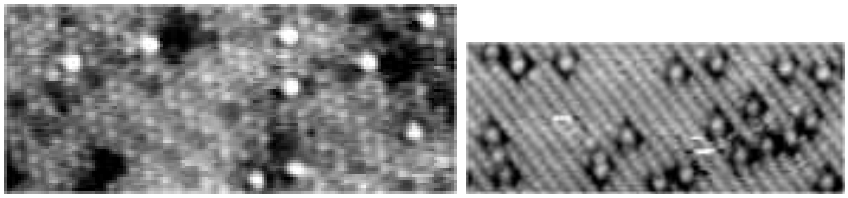

(a) (b)

Figure 6.1: a)STM images, $(10 \times 4)nm^2$, of a surface oxide with several "specks" and of a (1×1) with several "units", respectively; a)$V = 0.25\,\mathrm{V}$, $I = 1\,\mathrm{nA}$; b) $V = 0.3\,\mathrm{V}$, $I = 1\,\mathrm{nA}$.

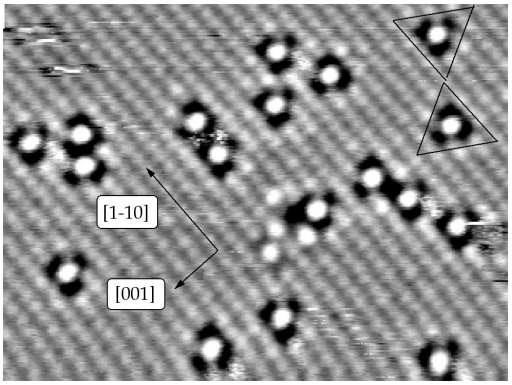

Figure 6.2: STM image of a (1×1) surface with several units: the Rh(110) crystallographic directions, as well as the two possible orientations of the units, are highlighted; $(8 \times 10)nm^2$, $V = 0.4\,\mathrm{V}$, $I = 2\,\mathrm{nA}$.

6.1 Units in detail

Figure 6.2 presents a high-resolution STM image in which we can distinguish the atomic rectangular arrangement of the (1×1) surface of Rh(110). The most visible entity, however, are the bright dots surrounded by a dark triangular rim: this is the species that we named *units*. They are almost randomly distributed over the terrace and they have two equivalent orientations, given by the triangular rim that can point towards the [001] or the $[00\overline{1}]$ direction. During the oxidation cycles, we observed not only an increase in the number of units on the terraces, but also new species at the steps. In fig. 6.3a we can distinguish two features in close proximity of the steps: the first one, indicated by the red arrows, can be recognized as units laying in the outermost available

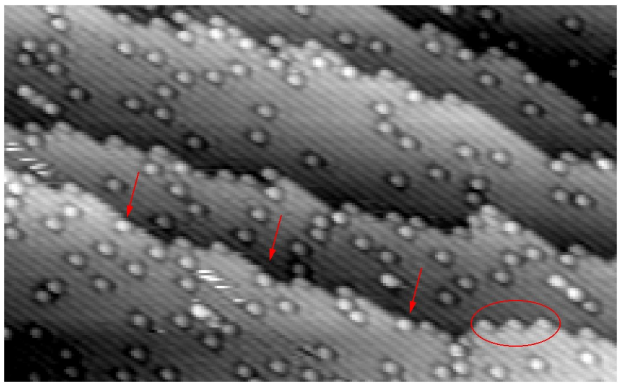

(a)

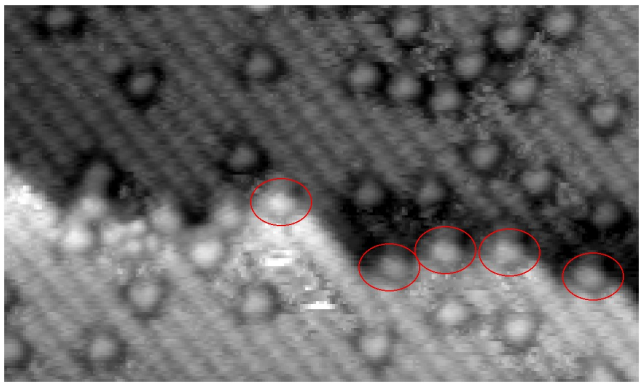

(b)

Figure 6.3: STM images of stepped (1×1) areas: the units at the steps are indicated by the red arrows and circles: a) $(7 \times 12)nm^2$, $V = 0.5\,\mathrm{V}$, $I = 1\,\mathrm{nA}$; b) $(14 \times 24)nm^2$, $V = 0.5\,\mathrm{V}$, $I = 1\,\mathrm{nA}$.

position on the upper terrace. The second one, on the other hand, does not show clearly a dark rim; moreover, it appears lower than the units. Despite all this, we identify also these species with the units, based on the following considerations:

their position corresponds to the one of a unit laying on the lower terrace;

on stepped areas of surfaces which were units-rich, we detected the maximum density of these features (fig. 6.3b).

Therefore from now on we will treat as units both the terraces and the step-belonging features.

To understand the units' structure, we first have to unambiguously determine their position with respect to the rhodium (1×1) surface atoms. For this purpose, we selected some images with very high resolution, we calibrated them to correct for distorsions introduced by our scanner and we superimposed the lattice grid on the units: the results are displayed in figure 6.4, together with a ball model of the Rh(110) surface (fig. 6.4a). In both orientations, the units occupy a bridge position with respect to the close-packed $[1\bar{1}0]$ Rh rows: in other words, the bright central spot is aligned with the 2^{nd} layer close-packed Rh row. One of the three sides of the dark rim, as a consequence, coincides with a first layer close-packed row, resembling a series of Rh atomic vacancies[1].

In the orthogonal direction (i.e. [001]), on the other hand, the bright spot is aligned with the first layer Rh rows, even though never perfectly centered.

We acquired line profiles across STM images containing the units, to measure their relative height/depth with respect to the Rh atoms, thus the knowledge we get contains both topographical and electronical influences. We would expect then the values to depend on the tunneling parameters (V_B and I); as presented in figure 6.5- 6.6, this was not exactly the case. In fact, the apparent height was found to be much more influenced by the tip conditions[2] than by the bias voltage or by the tunneling current.

In lower-resolution images (fig. 6.5) the apparent height of the central spot with respect to the rhodium atoms varies from $\sim 0.025\,\text{nm}$ to $\sim 0.04\,\text{nm}$ (upon a bias increase of $0.1\,\text{V}$); from 6.6, on the other hand, which has a better resolution, we derive much lower values ($\sim 0.007\,\text{nm}$ to $\sim 0.018\,\text{nm}$)[3].

6.2 Accumulation with cycles

During the cycles, we monitored not only the changes of the oxides morphology, but also the evolution of the (1×1) surface over which they were prepared: for this purpose, we often looked at the system with STM right after acquiring a TDS spectrum.

[1] In figure 6.4c we see three units embedded in linear holes made by multiple rhodium vacancies: the triangular dark rim is indistinguishable from the vacancies.

[2] Sometimes the highest resolution images are acquired when an foreign atom from the background or from the surface is picked up by the tip, governing the tunneling.

[3] With the aim of taking line profiles, these images have undergone only plane background subtraction, whereas in the other cases we usually perform a line-by-line correction.

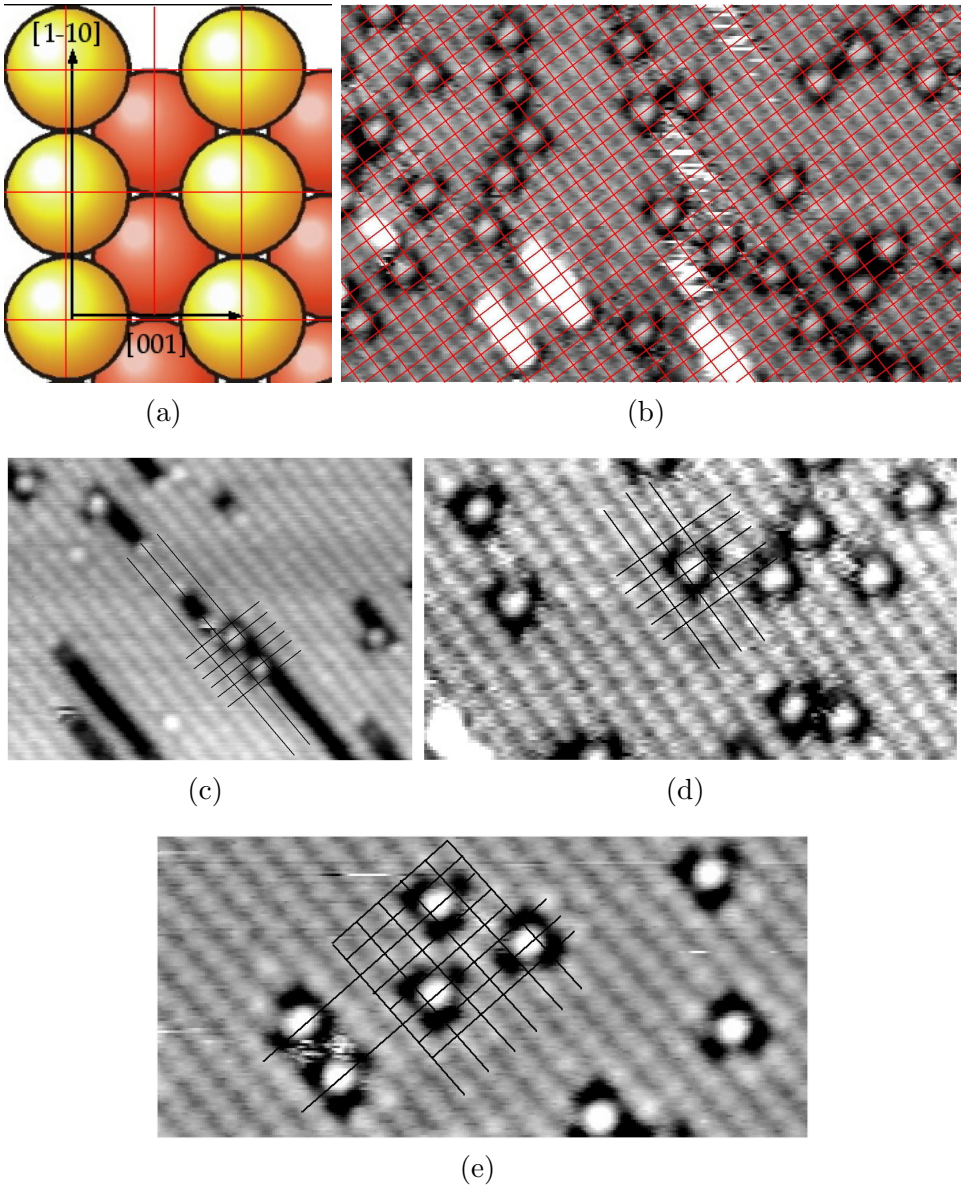

Figure 6.4: a) Ball model of the Rh(110) surface: yellow balls stand for 1^{st} layer Rh atoms, red ones for 2^{nd} layer atoms; crystallographic directions and the grid that is used for STM images calibration are shown. Small scale STM images with calibration grid superimposed to determine the relative units position with respect to the Rh atoms: b) $(6.5 \times 10.1)nm^2$, $V = 0.5\,\mathrm{V}$, $I = 1\,\mathrm{nA}$; c) $(5.5 \times 8)nm^2$, $V = 0.5\,\mathrm{V}$, $I = 1.6\,\mathrm{nA}$; d) $(4 \times 7)nm^2$, $V = 0.5\,\mathrm{V}$, $I = 1\,\mathrm{nA}$; e) $(3.5 \times 7.5)nm^2$, $V = 0.4\,\mathrm{V}$, $I = 2\,\mathrm{nA}$.

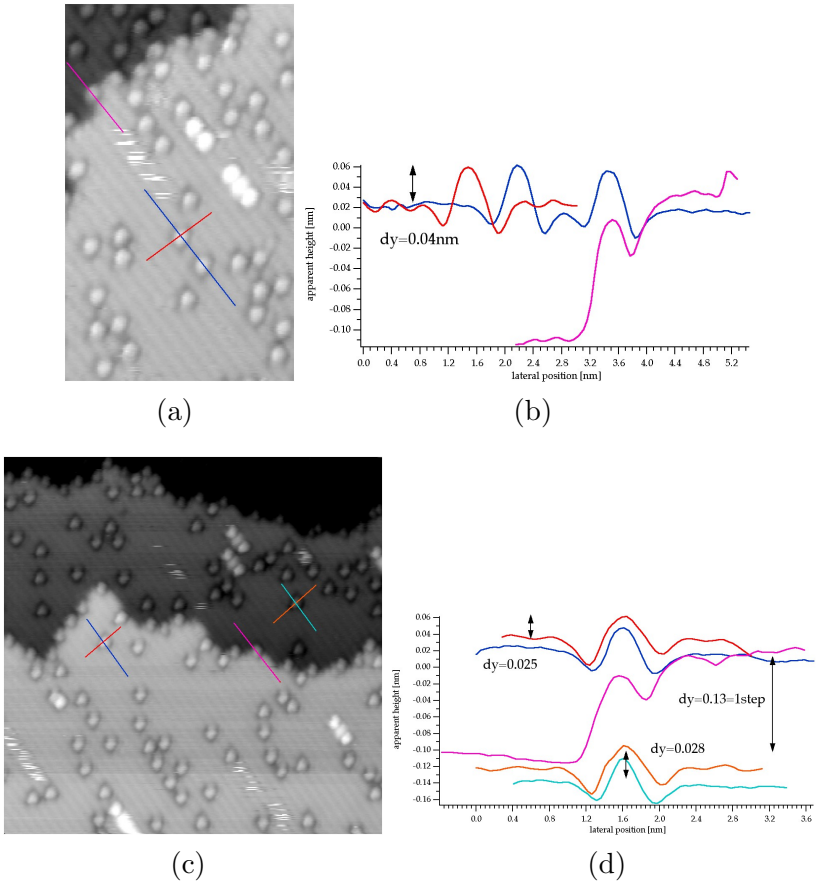

Figure 6.5: STM images of the units and relative line profiles: a)$(13.5 \times 8)nm^2$, $V = 0.5\,\mathrm{V}$, $I = 1\,\mathrm{nA}$; b) line profiles along the lines in a); c)$(20 \times 20)nm^2$, $V = 0.4\,\mathrm{V}$, $I = 1\,\mathrm{nA}$; d) line profiles along the lines in c).

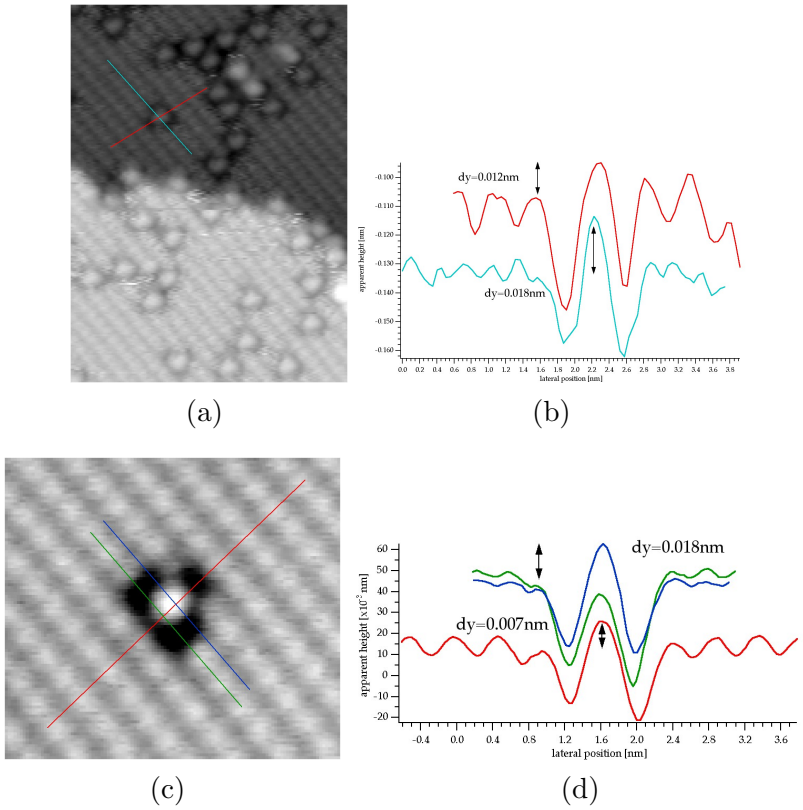

Figure 6.6: STM images of the units and relative line profiles: a)$(11 \times 8)nm^2$, $V = 0.5\,\mathrm{V}$, $I = 1\,\mathrm{nA}$; b) line profiles along the lines in a); c)$(3.8 \times 4.2)nm^2$, $V = 0.4\,\mathrm{V}$, $I = 2\,\mathrm{nA}$; d) line profiles along the lines in c).

6.2.1 Thermal cracker

After a few iterations with the thermal cracker, we discovered the units for the first time. As shown in figure 6.7, we observed a progressive increase in their density, up to a value of $\sim 4\%\,\mathrm{ML}$[4]; the increase was roughly linear up to the 10^{th} cycle, reaching a sort of plateau in the second part of the series.

In the mixed cycles, we focused on the TDS ageing more than on the STM. Nevertheless, we were able to count the units after 6 mixed cycles (see chap. 5, fig. 5.11), extracting a coverage of $\sim 3.5\%\,\mathrm{ML}$. Since using the thermal cracker we suffered from contamination of our oxides, a first idea would be to assign the units to contaminants; nevertheless, we detected them also when dosing molecular oxygen only, and we can therefore rule out this hypothesis.

6.2.2 Plasma source

When using the plasma source, instead, no units were detected on the (1×1) surface (fig. 6.8); this can be due to the following reasons:

all the oxides formed within these cycles were not complete, i.e. rich in oxygen vacancies[5];

the number of cycles performed in this series was lower than in the other cases, and this could have generated an ageing below our detection limit.

In figure 6.8 we present two STM images of the surfaces obtained after annealing the 2^{nd} and the 12^{th} oxide in the mixed cycles. They are similar and both defective, containing single and linear Rh vacancies and at least two foreign species: we cannot assign them to definite elements, but they can be either due to background gases or to contaminants of the crystal, like carbon. The plasma-grown oxides had all the same morphology, and also the TDS spectra were all similar. The lack of units is not only the third common feature between all the oxides of the measurement series, but can be regarded as the key stone for explaining the process: an oxide which is not able/allowed to decompose in a way that creates units, will not follow any ageing pathway. It is also possible that the incomplete oxides were simply forming much less units at every cycle, and therefore the accumulation was so much slowed down that we could not detect any ageing after 12 cycles.

[4]These percentages have been calculated by averaging over several images and assuming a T-student statistical distribution to estimate the error bars [96].

[5]In turn this could be either due to the beam characteristics or to the fact that the crystal could have been contaminated by carbon, see chap. 5.4.2.

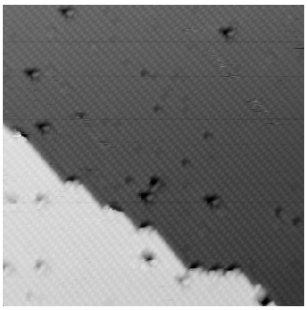

(a) after 3^{rd} cycle

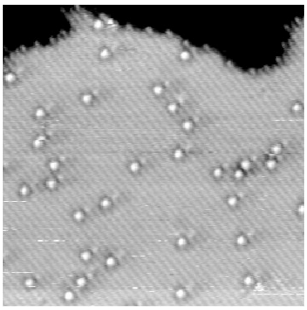

(b) after 5^{th} cycle

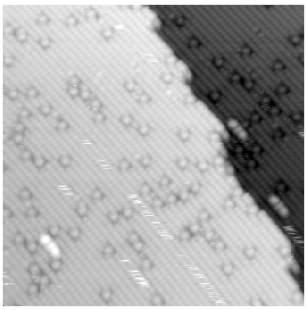

(c) after 7^{th} cycle

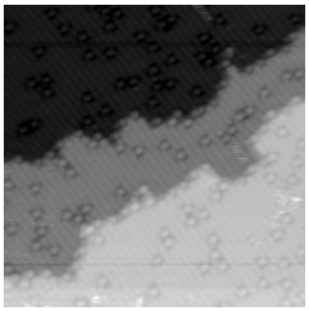

(d) after 10^{th} cycle

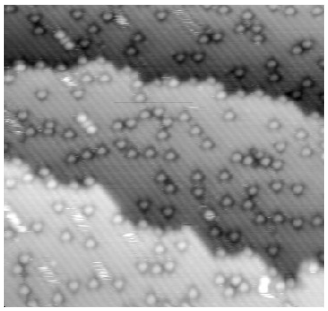

(e) after 12^{th} cycle

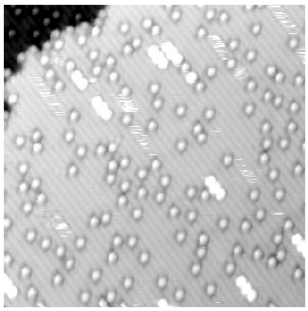

(f) after 15^{th} cycle

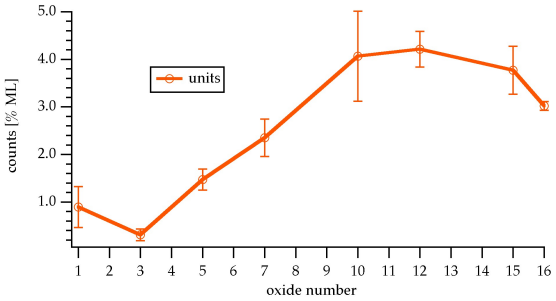

(g) counts

Figure 6.7: a)-f): STM images ($(20 \times 20)nm^2$)of the (1×1) surface obtained after desorption of several oxides during the thermal cracker atomic oxygen cycles. g) Density of units in percentage of Monolayer; the oxide number on the x axis refers to the oxide that was desorbed right before these STM measurements. Therefore the number of units corresponding to the, e.g., 10^{th} oxide will influence the growth of the 11^{th} one, etc.

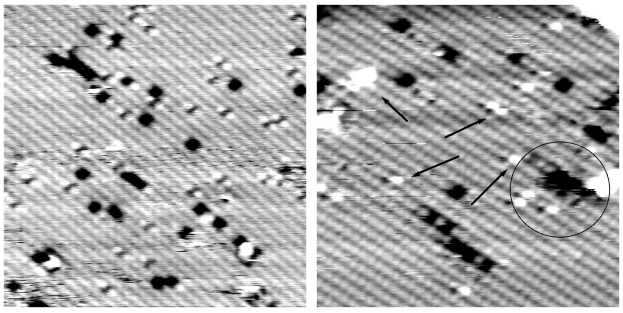

(a) after 2^{nd} mixed cycle (b) after 12^{th} mixed cycle

Figure 6.8: a) $(15 \times 15)nm^2$, $V = 0.4\,\mathrm{V}$, $I = 0.8\,\mathrm{nA}$; b) $(10 \times 10)nm^2$, $V = 0.4\,\mathrm{V}$, $I = 0.8\,\mathrm{nA}$.

6.2.3 Molecular oxygen

During the molecular oxygen cycles, when we attained the highest degree of oxides ageing we also detected the maximum density of units after acquiring the TDS spectra. In figure 6.9a we show an image with a units coverage of $\sim 6\%$ ML: at this point it was striking clear that the unit were *not* made of platinum nor iridium, like we had previously supposed. To support our idea that the units[6] were responsible for the observed ageing, through the blocking of the active sites for O_2 dissociation, we tried to reduce their density without sputtering the surface. This was obtained by several slow annealings in UHV between $\sim 250\,^{\circ}\mathrm{C}$ and $\sim 400\,^{\circ}\mathrm{C}$, and the result is presented in figure 6.9b. As discussed in chapter 5.4.4, this much lower density of units lead to a (partially) recovered oxide, from both the TDS and STM point of view. This was the definitive proof that the units can be considered as fingerprints of the ageing process.

In figure 6.9d we plot a summary of the percentage of units found on rhodium for selected cycles from the 27^{th} to the 46^{th}. We cannot distinguish any increase because our first measurement already gave a high value; moreover, we could never reach this amount again with the subsequent iterations. Except for the (1×1) obtained after the 27^{th} and the 36^{th} TDS, we did not try to reduce the units density: therefore we observed a slow increase after the 37^{th} oxide (fig. 6.9c), anyway not reaching the original coverage. This is consistent with the fact that we never observed such a disrupted oxide (with a tiny TDS

[6] and the specks, that we think are derived from them.

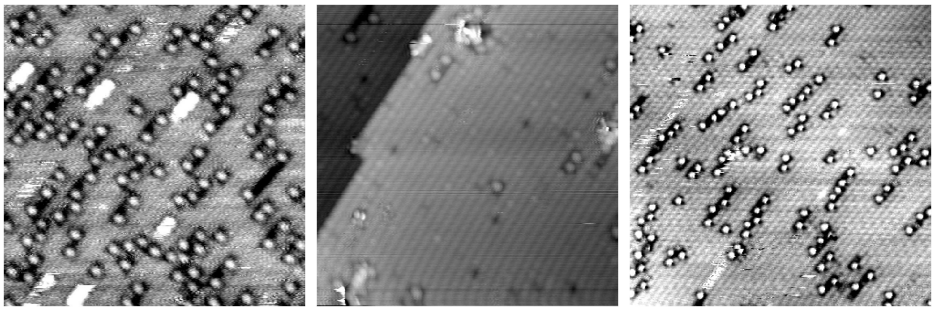

(a) after 27^{th} cycle (b) + UHV annealings (c) after 31^{st} cycle

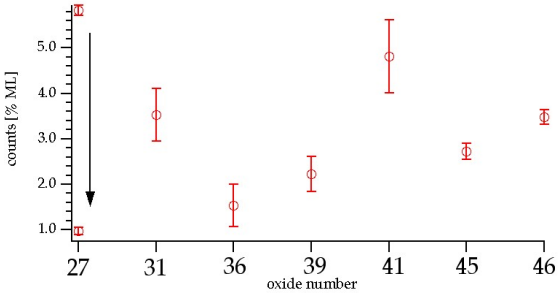

(d) counts

Figure 6.9: a) $(15 \times 15)nm^2$, $V = 0.4\,\mathrm{V}$, $I = 0.7\,\mathrm{nA}$; b) $(15 \times 15)nm^2$, $V = 0.4\,\mathrm{V}$, $I = 0.6\,\mathrm{nA}$; c) $(15 \times 15)nm^2$, $V = 0.4\,\mathrm{V}$, $I = 0.4\,\mathrm{nA}$; d) summary of the units concentration during the molecular oxygen cycles; after the 27^{th} cycle we measured first a high density of units, but then we were able to reduce it significantly with slow UHV annealings: therefore we have two points in the graph corresponding to the (1×1) obtained after the 27^{th} TDS.

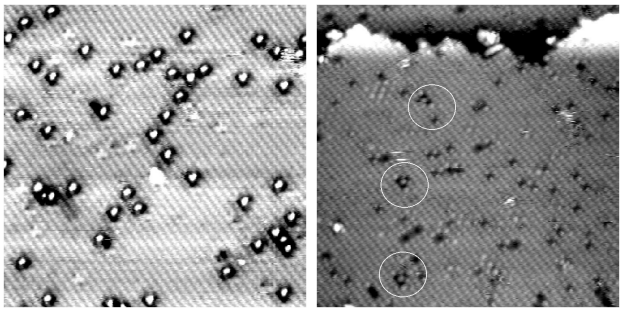

(a) (b)

Figure 6.10: $(20 \times 20)nm^2$, $V = 0.4\,\mathrm{V}$, $I = 1\,\mathrm{nA}$: a) STM image of a units-rich surface b) same surface after dosing $\sim 50\,\mathrm{L}$ of H_2 at 800 °C: the number of units is decreased by $\sim 90\%$.

integral) as the 27^{th} one.

6.3 Units reactivity

To make some hypotheses on the chemical identity of the units, we first review their evolution when exposed to two reducing gases: H_2 and CO. Both these gases were able to modify the density of units, strongly suggesting that the units contain oxygen.

In figure 6.10 we show two images referring to the (1×1) surface obtained after 2 mixed cycles; the second one is acquired after dosing $\sim 50\,\mathrm{L}$ of H_2 at 800 °C. It is clear that the number of units is decreased by $\sim 90\%$. Anyway, this is not enough to support the idea that the units contain oxygen: the high temperature at which the hydrogen was dosed could have been the main agent for anti-segregation or dissociation processes. Nevertheless, we performed several vacuum annealing experiments on the units-rich surfaces, and we could not find a reproducible behaviour when annealing to temperatures higher than 400 °C; on the other hand, the dramatic decrease in the units' density after H_2 dosing at 800 °C was found to be fully reproducible. Therefore hydrogen exposure seems to be necessary to get a decrease in the units density.

The interaction with CO turned out to be less straightforward, and is summarized in figure 6.17. We started from a surface with several linear holes, on which most of the units were positioned at holes' ends: they look like embedded

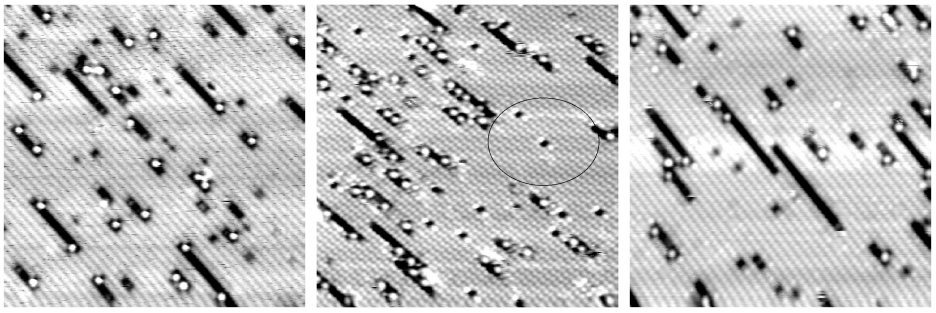

(a) (b) +30 LCO (c) +flash@400 °C

Figure 6.11: $(20 \times 20)nm^2$ a) STM image of a units-rich surface, $V = 0.5\,\mathrm{V}$, $I = 2\,\mathrm{nA}$; b) after dosing 30 L of CO at RT, $V = 0.6\,\mathrm{V}$, $I = 1.6\,\mathrm{nA}$; c) same surface after flashing in vacuum up to 400 °C, $V = 0.5\,\mathrm{V}$, $I = 1.6\,\mathrm{nA}$.

in the missing Rh row, thus suggesting that also some rhodium vacancies may contribute to their structure. Upon CO dosing at room temperature, we observed two changes in the surface:

on the units-free patches, we can see a zig zag arrangement (e.g. in the black circle in fig. 6.11b) given by the $(2\times1)p2mg$ CO adsorption structure [97], having a local CO coverage of 1 ML; therefore at *RT* we were able to cover the surface with one monolayer of carbon monoxide.

The number of units had significantly increased ($+ \sim 50\%$); moreover, also the new ones were positioned *inside* the linear holes.

Finally, performing a flash up to 400 °C, we came back to the original situation: no more CO adsorption structures neither more units. We know ([97]) that CO desorbs from the Rh(110) surface at $\sim$ 230 °C: it is then obvious that after annealing to higher temperatures we did not find any trace of adsorbed molecules. The decrease in the units density, on the other hand, was not expected and it is not well understood so far. However, it points to an oxygen-containing model for the units: we can imagine a CO molecule dissociating or sticking into the holes, providing an oxygen atom to a unit; upon annealing, viceversa, we can think that CO recombines[7], therefore restoring the initial units' density.

[7] Also CO_2 could be formed.

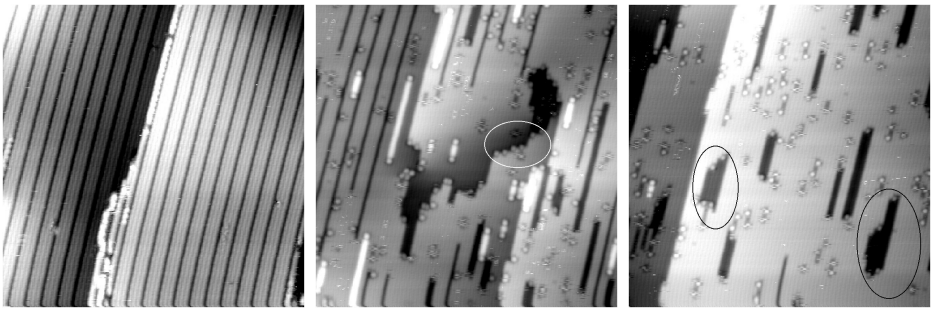

(a) (b) (c)

Figure 6.12: $(30 \times 30)nm^2$ a) $c(2 \times 8)$ adsorption structure, $V = 0.6\,\mathrm{V}$, $I = 0.8\,\mathrm{nA}$; b) during H_2 dosing at $\sim 200\,^{\circ}\mathrm{C}$, $V = 0.6\,\mathrm{V}$, $I = 0.8\,\mathrm{nA}$; c) later stage of the reaction, $V = 0.47\,\mathrm{V}$, $I = 0.8\,\mathrm{nA}$.

6.4 Units in old measurements

Up to now we treated the units as a *new* species, as if they were first observed during the cycles measurements. This is not true, in fact there are some old (i.e. previous to this PhD start) data containing unidentified features which turned out to closely resemble our units.

The common ingredient between the following three cases is that the sample was treated with annealing in oxygen atmosphere. These procedures, together with a short sputtering at 1 keV, may have lead to both units formation and accumulation.

The first case in which units were observed has been the reduction, upon H_2 dose at $\sim 200\,^{\circ}\mathrm{C}$, of the oxygen $c(2 \times 8)$ adsorption structure [98]. The reduction reaction front was faster than the acquisition time, so there was an abrupt change in the surface between two subsequent images: in fig. 6.12b and in the last one we see that the (1×3) Rh reconstruction is progressively lifted, in favor of a clean (1×1) surface with one-layer deep holes in it. What is more interesting for us, however, are the little spots that can be distinguished at steps, both between two terraces and at holes borders (i.e. at troughs ends): to a closer look, these are our units. Also the second case refers to a hydrogen titration reaction, but performed at low ($\sim -14\,^{\circ}\mathrm{C}$) temperature [42, 84, 99]. The starting surface is a $(2 \times 1)p2mg$ oxygen adsorption structure, obtained by dosing 6 L of O_2 at 200 K and annealing to 260 K. The chains visible in the first image of figure 6.13 (elongated in the $[1\bar{1}0]$ direction) are undefined species ar domain boundaries. The reaction proceeds through the formation of

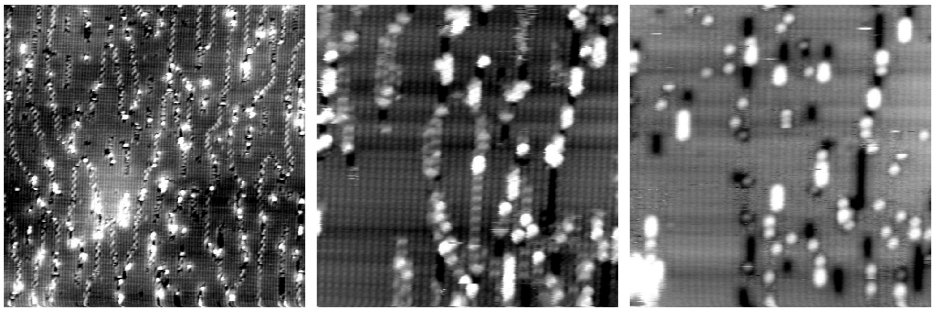

(a) (b) (c)

Figure 6.13: STM images of the $(2 \times 1)p2mg$ O adsorption structure, a) $(50 \times 50)nm^2$, $V = 0.18\,\mathrm{V}$, $I = 0.56\,\mathrm{nA}$, $V = 0.36\,\mathrm{V}$; b) $(20 \times 20)nm^2$ $I = 0.72\,\mathrm{nA}$; c) reduced surface obtained after dosing H_2 at $\sim -14\,^{\circ}\mathrm{C}$, $V = 0.5\,\mathrm{V}$, $I = 1.6\,\mathrm{nA}$.

oxygen pairs arranged in a $c(2 \times 4)$ symmetry and subsequently through an intermediate $c(2 \times 2)$ structure [99]; from the borders of this last structure the water formation reaction proceeds, leaving the (1×1) surface shown in 6.13c. Even if in smaller quantities with respect to the previous reaction, the units are visible inside linear Rh holes as well as isolated on the terraces.

The third system was prepared by saturation of the surface with water at 170 K dosed on 0.35 L of O adsorbed at 273 K, resulting in an OH covered surface shown in figure 6.14a [42]. The layer decomposition was obtained by a slow annealing inside the microscope, from 170 K to 277 K. The final surface is a clean (1×1), with quite a high density of units ($\sim 1.7\%$ ML, fig. 6.14c).

The higher number of units observed in this case with respect to the previous ones can be explained by the fact that the sample cleaning procedure included a continuous annealing between 450 °C and 650 °C in $p_{O_2} \sim 1 \times 10^{-7}$ mbar. This preparation was repeated every day and the 1 keV sputtering might not have erased the units that were eventually formed.

To summarize, the units were detected in past measurements after desorption of oxygen from reconstructed surfaces and consequent deconstruction of rhodium up to the (1×1) structure. Some of the reaction movies (see also chapter 7) suggested that the units could be formed starting from some traveling bright Rh-O complexes ([66, 85]), for example by trapping of one of those complexes inside a rhodium vacancy. These data turned to be useful when validating hypothesis on the units chemical composition, as is discussed in the next section.

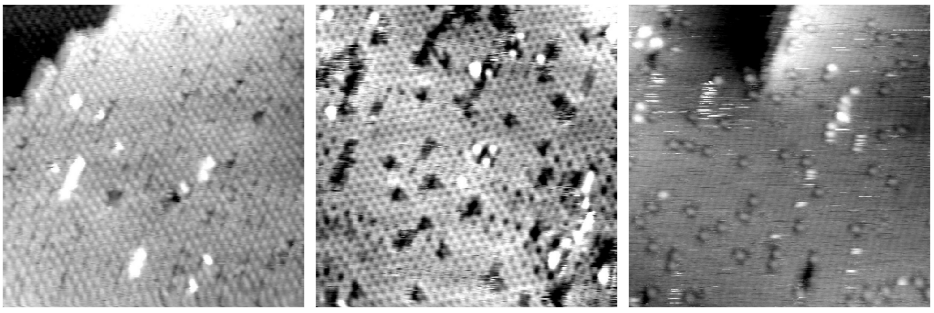

(a) (b) (c)

Figure 6.14: $(20 \times 20)nm^2$ a)STM image at 270 K of a OH+O covered surface, $V = 0.1$ V, $I = 0.6$ nA; b) after gradual annealing, acquisition at ~ 225 K, $V = 0.34$ V, $I = 0.59$ nA; c) acquisition at 277 K, $V = 0.6$ V, $I = 0.6$ nA.

6.5 Hypothesis on units' identity

We can think of two main possibilities for the nature of the units:

either they are a contaminant stemming from our UHV system

or they are *intrinsic*, i.e. related to Rh and oxidation/reduction treatments -and eventually oxygen- only.

The first hypothesis can in turn be split in two: as a contaminant we can either have a background gas sticking to the Rh (1×1) surface, or a foreign metal atom coming from our chamber, from the sample holder or from the crystal itself.

Since STM has not chemical sensitivity, identification of an unknown species directly from the images is not achievable in most situations. However, it is possible to dose gases while scanning, and so a simple way to assign a feature to a specific gas is to increase the partial pressure of that gas during measurements. Our first try was then to compare the images of the units and those obtained after exposing the Rh(110) surface to the most common background gases of our experimental system: H_2O, H_2 and CO.

In figure 6.15 we present an image of a $H_2O + O$ overlayer on Rh(110): as already shown in previous studies, water-related species form islands, even at room temperature, with an hexagonal inner arrangement [42, 99]. It is thus unlikely that the units are related to H_2O, because they do not resemble any

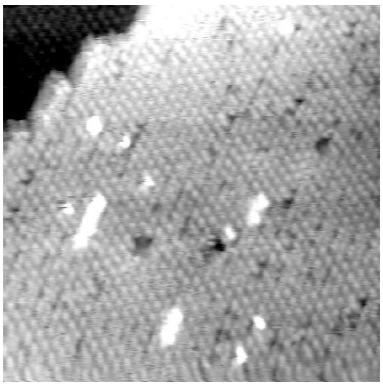

Figure 6.15: STM image of a $H_2O + O$ hexagonal network on the Rh(110) surface; $(20 \times 20)nm^2$, $V = -0.15\,\mathrm{V}$, $I = 0.28\,\mathrm{nA}$.

building block of the water network and they were never found in homogeneous islands.

The prevailing species in our background pressure is hydrogen; therefore one of our hypotheses was considering hydrogen as their building-block. Recent measurements on the interaction of hydrogen with the Rh(110) surface are discussed in [100]. Hydrogen forms a series of adsorption structures with coverages from 0.33 ML to 2 ML; all of them are based on H atoms arranged in linear chains, giving rise to rectangular units cells. In figure 6.16 we report an STM image of the (1×3) 1 ML coverage structure. The surface arrangement formed by H_2 does not correspond to the units triangular appearance; moreover, all these structures are stable only for $T \leq 300\,\mathrm{K}$, while we observed the units also at 200 °C (e.g. see the previous section). Therefore also hydrogen can be ruled out from the list of possible candidates for building the units.

We know from previous data that CO_2 does not stick on the rhodium (1×1) surface at room temperature ([61]). We have already presented the interaction between the units and carbon monoxide. Since we observed an increase in their density upon CO dosing, we present the hypothesis that this molecule could be involved in the units formation process. To understand this, we dosed CO while scanning, thus performing a different measurement from the *ex situ* one described above, using quite lower tunneling currents. In figure 6.17 we plot two images acquired on the same area at two different stages of dosing: it is clear that the bright, elongated fuzzy features are increasing with the exposure. These species can therefore be assigned to carbon monoxide molecules; since we

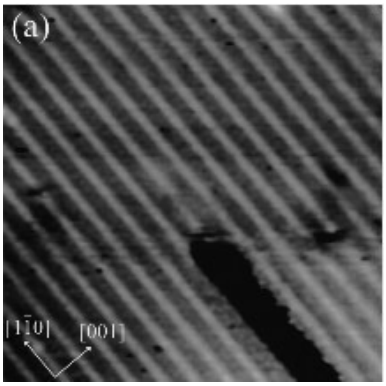

Figure 6.16: STM image of the (1×3) hydrogen adsorption structure on Rh(110); $T = 140\,\mathrm{K}$, $(15 \times 15)nm^2$, $V = 0.4\,\mathrm{V}$, $I = 1\,\mathrm{nA}$.

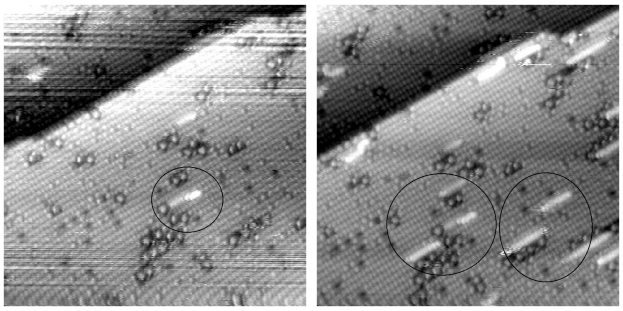

(a) (b)

Figure 6.17: $(20 \times 20)nm^2$, $V = 0.3\,\mathrm{V}$, $I = 0.7\,\mathrm{nA}$; STM images of a units-rich surface, during CO dosing from the background ($p_{\mathrm{CO}} \sim 2 \times 10^{-9}\,\mathrm{mbar}$) at room temperature, at two subsequent times..

know, however, that CO caused an increase in the density of units, we cannot exclude that some CO dissociation products (e.g. oxygen) or CO containing species may play a role in their formation.

Finally, the argument that lead us to reject the hypothesis that the units are contaminants coming from the background pressure, stems from a statistical consideration. During thousands of hours of STM measurements, it never happened that a unit (or a part of it) was picked up by the tip and removed or simply moved around on the surface. Even while scanning at $\sim 200\,^{\circ}\mathrm{C}$, we only observed a flip movement of the units, switching between the two possible orientations; during chemical reactions, they were observed moving for no more than a few atomic positions. The usual behaviour of an isolated adsorbed species is completely different: it is not rare to pick it up.

To discuss the possibility that the units are a contaminant different from the common UHV background gases, we have to recall what have been presented in chapter 5.1. Using the thermal cracker, we faced Pt and Ir contaminations; nevertheless, we found the units also after dosing molecular oxygen only, and therefore we can exclude that they were made of one of these two metals. The only common contaminant throughout our measurements has been Nickel. Nickel came most probably from our Chromel and Alumel type K thermocouples, that contain more than $\sim 90\%$ of Ni [67][8]. The maximum Ni coverage we detected on our sample was $\sim 1\,\%$ML, therefore quite lower than the $4-5\%$ deduced from several STM images. In the end, the most important information came from the old data: in the first case, in fact, the thermocouples were still *not* mounted neither on the sample nor on the sample holder. This fact allows us to exclude that the units are formed by Ni.

From all these considerations, it is reasonable to think that these ageing fingerprints are really *intrinsic*; in other words, not related to any external source of contamination but instead due to the cyclic treatments undergone by the sample. A hint to develop a tentative model of the units comes the following considerations:

they are formed when a deconstruction of an oxygen-rich phase occurs, either by means of annealing or by hydrogen titration[9];

[8] It could have come also from the Rh bulk, where it is declared to be present in $\leq 5\,\mathrm{ppm}$. However, in this case we would have expected to see the units also during the plasma source cycles, if their segregation simply had been due to annealing.

[9] The TDS spectra presented in the previous chapter helped us in understand the formation and accumulation of the ageing seeds. In fact, even if an oxide was grown on a surface with a small number of them (resulting in a different morphology), its spectrum was forward shifted: this suggests that the already formed ones segregate to the surface during the oxide annealing, and in the meantime the new ones are formed.

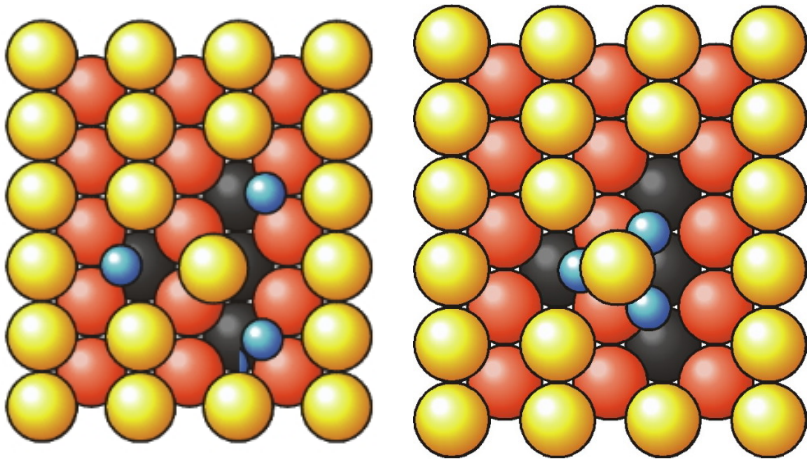

(a) (b)

Figure 6.18: Tentative models for a unit: yellow, red and black balls represent 1^{st}, 2^{nd} and 3^{rd} layer Rh rows, respectively; small blue circles represent oxygen atoms.

they are accumulated upon oxidation cycles[10];

their number can be lowered by hydrogen titration at high temperatures or by slow annealing below 400 °C;

they seem to be not related to the presence of any surface contaminant, despite playing a major role in the ageing process.

From these facts we tentatively suggest a unit structure involving only rhodium and oxygen. Moreover, from the STM images we get also a strong indication that the dark triangular rim of every unit may be made of Rh vacancies. This does not exclude, however, the presence of oxygen atoms inside the vacancies. In fact, the dark area surrounding the central bright spot resembles the O rich troughs of the $c(2 \times 2n)$ adsorption structures. On Rh(110), oxygen was found to sit preferentially into threefold adsorption sites, up to 1 ML coverage (see fig. 4.16, [84]). Therefore our first model, sketched in figure 6.18a, involves:

- a quadruple rhodium vacancy,
- four oxygen atoms positioned in threefold adsorption sites,
- and a "trapped" central Rh atom[11].

[10] With the exception of the plasma source case, discussed in chapter 5.4.2.
[11] The balance is therefore of three rhodium vacancies per unit.

However, in this configuration the oxygen atoms are not directly bonded to the central Rh, which has no special reason to keep its position. Therefore we propose an alternative model (fig. 6.18b) in which, instead, oxygen is bond to the isolated rhodium; the oxygen sites are not precisely threefold, because each O is indeed fourfold coordinated.

From out data it is not possible to discriminate between these two models; this is a case in which complementary techniques like XPS and DFT are needed.

Chapter 7

Reactivity studies

This chapter is dedicated to reactivity studies over the trilayer surface oxide. First we review STM measurements that allow imaging a reaction down to the atomic scale; then we present LEEM experiments that provide complementary information on the mesoscopic scale.

7.1 Surface oxide titration reactions imaged by STM

Imaging a chemical reaction by STM fully exploits the capabilities of this technique, combining spatial and temporal resolution. Even if lacking in chemical sensitivity, STM can help to understand a reaction mechanism: a fast acquisition becomes therefore of crucial importance, to access every reaction step [42, 79, 84][1].

7.1.1 H_2 titration reactions

The H_2 titration reaction of the Rh(110) surface oxide was already investigated in a previous work [66]: we describe it as a useful benchmark to be compared with the H_2 reaction we performed during this PhD work and the LEEM data. At that time, the starting surface was not completely covered with the trilayer that coexisted with oxygen adsorption structures covering $\sim 30\%$ of the surface. The reaction was performed at 370 K: at this temperature the reaction product, H_2O, immediately desorbs from the surface, and it is therefore not imaged;

[1] Recently our group developed an electronical *add-on* module that permits to speed up the usual acquisition rate by a factor of ~ 1000, thus reaching ~ 30 msec/image, i.e. real videorate acquisition [101]. In this thesis, however, we will show only reactions studied with the standard speed and not with the boosted one.

hydrogen was dosed in the background while scanning, and the effective pressure at the surface below the tip was $p_{H_2} \sim 1 \times 10^{-8}$ mbar [66]. In figure 7.1a the surface before the reaction is shown: the surface oxide coexists with the $(2 \times 1)p2mg$ adsorption structure (which has an O coverage of 1 ML), in the center. The induction time needed to detect a visible change in the images was $\sim$ 18 L of H_2, in agreement with photoemission data (see ref. [66]) and with the LEEM movie acquired over an oxide covering only part of the surface. Figure 7.1b displays the first new features that were observed upon hydrogen dosing, appearing as "bright dashes" homogeneously distributed over the oxide areas; similar features were attribute to mobile Rh-O species [85]. It is worth noting that after a few images ($\sim$ 7 min) these little stripes disappear, and in the same time new dark features show up inside the oxide regions: as visible in the inset of fig. 7.1c), they are organized in a $c(2 \times 4)$ structure; in ref. [66] the authors suggested that this network could be made of oxygen vacancies. During this PhD thesis, we observed a network with exactly the same appearance when an oxide was left for several hours in UHV (i.e. reducing, see chap.r 4.2.2), as well as before a titration reaction over a complete oxide: based on these results, we can confirm the hypothesis that this structure is an ordered array of oxygen vacancies. It is likely that the first H atoms are produced by H_2 dissociation on some defects, resulting in the formation of nuclei of reduced rhodium: the oxygen vacancies network seems therefore to be necessary for the ignition of the reaction: in fact, the subsequent image (d) shows how the reduction front, appearing as a diagonal line, propagates over the surface within the acquisition time (32 sec) of a single frame. The sharp and atomically resolved edge in the bottom part of the figure separates a still nonreduced oxide region ahead of the front from the structurally changed reduced area behind. From the STM images we can estimate a speed of the reaction front of $\sim$ 0.5 nm/sec that will be compared with LEEM data in the next section. In a few scan lines the Rh atoms rearrange into a Rh(110)$-(1 \times 1)$ layer with added $[1\bar{1}0]$ rows above[2], which are stabilized by the remaining oxygen. The reduction front also attacks the $(2 \times 1)p2mg$ adsorption phase, over which oxygen is thought to rearrange into $O - O$ pairs [99]. Finally, the removal of the remaining oxygen takes place at a slower rate (see fig. 7.1e), following the same pathway observed for the $(2 \times 2)p2mg$ oxygen adsorption structure [102].

In this work, we decided to perform a titration reaction with hydrogen over a complete oxide, obtained after several cycles with molecular oxygen. The temperature was the same as in the previous case, i.e.$\sim$ 370 K; the gas partial

[2]Due to the 25% higher density of rhodium in the surface oxide with respect to the Rh(110) surface.

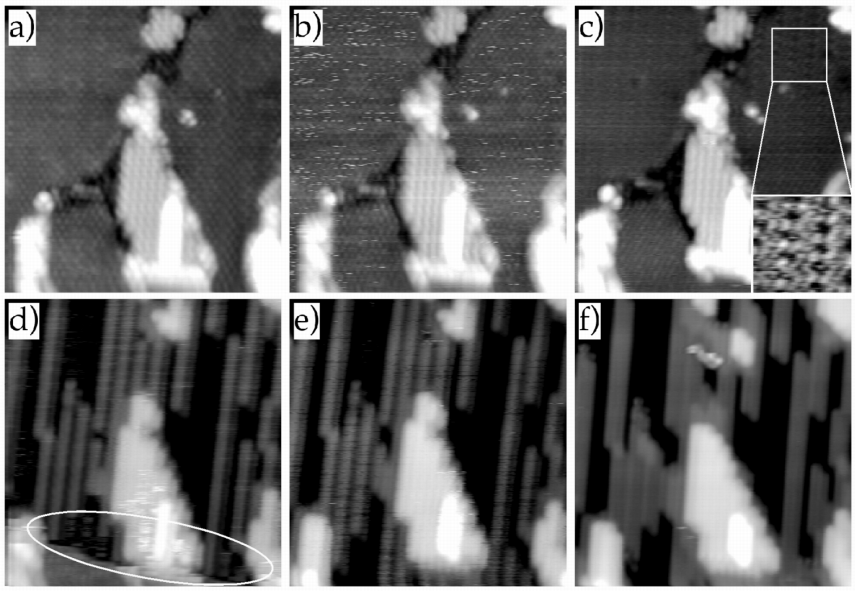

Figure 7.1: STM images acquired at 370 K during H_2 reduction; $(15.5 \times 16)nm^2$, 32 sec/image, $V_B = -0.6$ V, $I = 0.4$ nA. The insert in (c) is a zoom of the area, where the created $c(2\times4)$ network of oxygen vacancies has formed. The white ellipse in (d) indicates the reaction front (propagating downward). H_2 exposures: a) 17.7 L, b) 19.3 L, c) 23.1 L, d) 23.4 L, e) 23.7 L, f) 28.6 L [66].

pressure was chosen to be $p_{H_2} \sim 4.4 \times 10^{-9}$ mbar at the sample[3]. The starting surface, shown in figure 7.2a, is the 37^{th} oxide grown during the molecular oxygen cycles[4]; this oxide did not coexist with adsorption structures, covering indeed all the surface but presenting some little holes one-trilayer deep. With respect to the previous case, we observed a shorter induction time before detecting the reaction front: this can be due to the fact that the background pressure in the chamber was slightly higher in this case, therefore favouring the formation of oxygen vacancies. It has to be remarked, however, that from an STM movie we can only get an estimate of the order of magnitude of an induction time, because we do not know how far the front was ignited from

[3]In [85] it was estimated that the STM tip was screening a background gas pressure, in the scan area, of a factor ~ 5; therefore in this experiment the H_2 background pressure was $\sim 2.2 \times 10^{-8}$ mbar, but the value at the sample was the one reported in the text.

[4]See chapter 5.4.3: this was an oxide partially recovered from ageing, with a morphology more similar to a first, complete oxide than to a disrupted one.

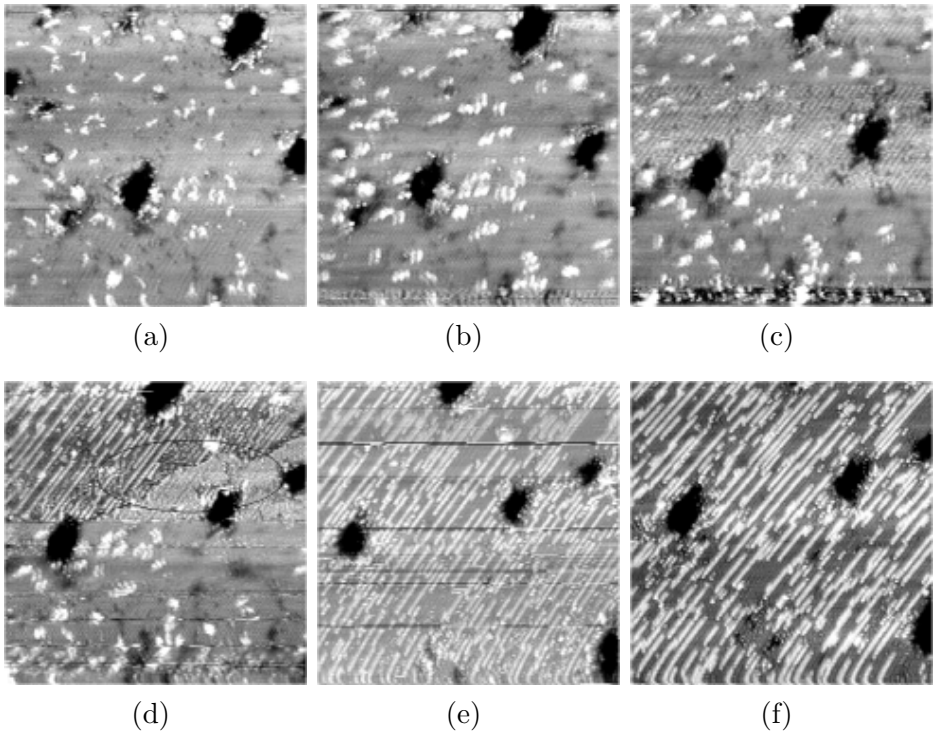

Figure 7.2: STM images acquired at 370 K during H_2 reduction; $(50 \times 50)nm^2$, 41 sec/image, $V_B = 0.35$ V, $I = 0.5$ nA. H_2 exposures: a) 2.16 L, b) 2.43 L, c) 2.7 L, d) 2.83 L, e) 2.97 L, f) 3.37 L. The white blurred things observed over the oxide can be attributed to CO molecules, based also on what shown in chapter 6.3; anyway, they do not have any influence of the reaction.

the area we are looking at[5]; moreover, a correct estimate of an induction time should be based on some statistic measurements, i.e. on several experiments.

A part from the induction time, the reaction pathway reproduces what observed over the mixed oxide+adsorption structure surface:

the $c(2 \times 4)$ network of oxygen vacancies is visible as a dark modulation in the central part of fig. 7.2c, and looks completed right before the passage of the reaction front;

the front speed can be roughly estimated to be $\sim 0.5\,\mathrm{nm/sec}$, from image 7.2d;

behind the front, a (1×1) surface with added rows is formed, and the Rh atoms show a transient mobility (see single atoms diffusing in fig. 7.2d) before sticking at segmented rows (fig. 7.2f).

after the front, the second part of the reduction is slower and homogeneously occurring over the surface.

Therefore on both surfaces a complete vacancies network has to form on the oxide to allow faster H_2 dissociation and subsequent front propagation; a tentative comparison between the front speeds will be discussed in the next section.

7.2 LEEM: a mesoscopic scale view of the surface oxide

In this section we describe the measurements that have been performed with the SPELEEM instrument at the *Nanospectroscopy* beamline (Elettra, Trieste) [71]; the basics of the LEEM technique are described in section 2.5. The LEEM is capable of imaging the surface morphology on areas of several $\mu\mathrm{m}^2$ (far too large for any STM), and to achieve lateral resolution as high as $\sim 20\,\mathrm{nm}$, therefore representing a valuable link between the atomic and the mesoscopic scale. The results are discussed only from a qualitative point of view; nevertheless, LEEM data enriched our knowledge on both the oxide structure and reactivity.

7.2.1 Domains

As already presented in chapter 4.1, the trilayer surface oxide grown on Rh(110) has 2 rotational domains, whose structure is schematized in figure 7.3 [24].

[5] And this is far more crucial in STM than in LEEM, because we look at much smaller regions.

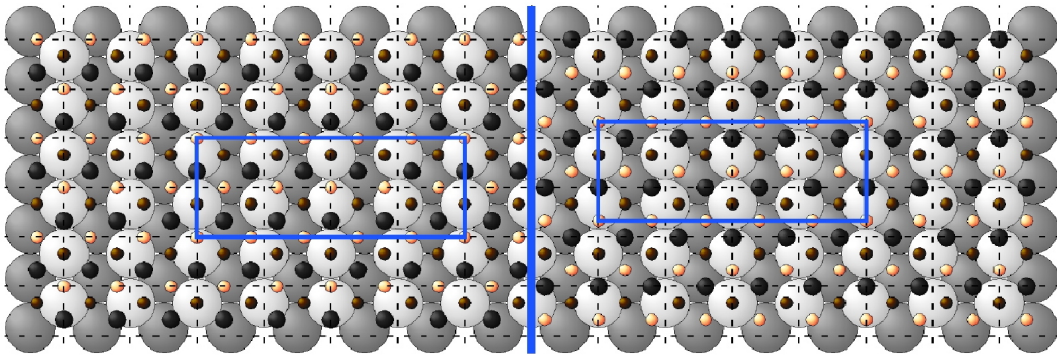

Figure 7.3: Structural model of the two domains formed on the c(2×4): the domain on the right is rotated by 180 °C. Large spheres: bulk Rh atoms; medium dark ones: trilayer Rh atoms; yellow and purple small spheres stand for oxygen atoms in the topmost and interface layers, respectively. [24].

A grid with substrate periodicity is superimposed in a way that the topmost oxygen atoms building an oxide unit cell coincide with grid crossings, in the left hand part of the image; the units cells are highlighted in both domains. The cells are shifted in the $[1\bar{1}0]$ direction by $\sim 30\%$ of the Rh lattice constant. The domain on the right can be explained as a 180 °C rotation of the domain on the left around the axis orthogonal to the surface, intersecting it at the position of a substrate Rh atom. The two domains are energetically equivalent, i.e. they are expected to cover $\sim 50\%$ of the surface each. Nevertheless, as we will show, this is not necessarly the case on our Rh(110) crystal. When performing *bright-field* LEEM, as in figure 7.4, the two domains show no contrast (see 2.5, [104]). In the *dark-field* mode, on the contrary, a secondary diffracted beam is selected for imaging: all and only the areas that contribute to the formation of the chosen beam appear bright. When choosing two non-equivalent spots of the c(2×4) (spots "A" and "B" in figure 7.5a) for imaging the same system[6], we observed two "domains". From LEED as well as from STM data we knew that the surface was completely covered with the oxide, and that the domains size is comparable to what we see in the LEEM images. Moreover, the contrast of the two images 7.5b and 7.5c is inverted, thus confirming that there are two structures contributing in opposite way to the spots.

Looking closer at the images, it is evident that the two domains do not cover the same area on the surface, i.e. the one which is bright in figure 7.5b

[6]Preliminary LEED-I/V data showed that these spots have not the same behaviour, probably due to to the different contribute of each domain.

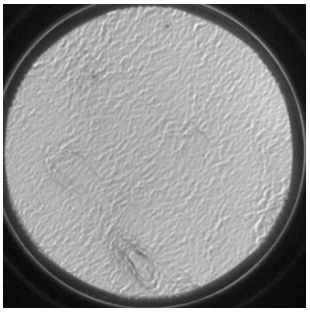

Figure 7.4: Brightfield image of the Rh(110) surface oxide; field of view (fov)=6μ m. In this mode, the two domains show no specific contrast; the lines visible in the image are steps (or step bunches)..

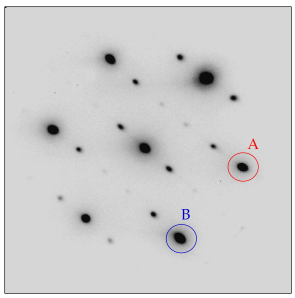

(a) leed 40 eV

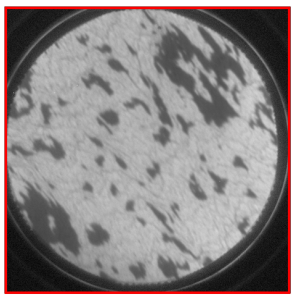

(b) darkfield with spot A

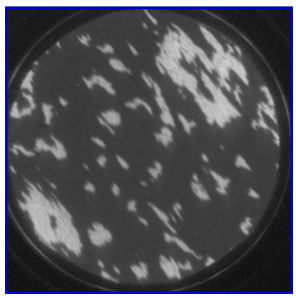

(c) darkfield with spot B

Figure 7.5: LEED image of the surface oxide with the two spots chosen, and corresponding darkfield images; E=30 eV, fov=6 μm [103].

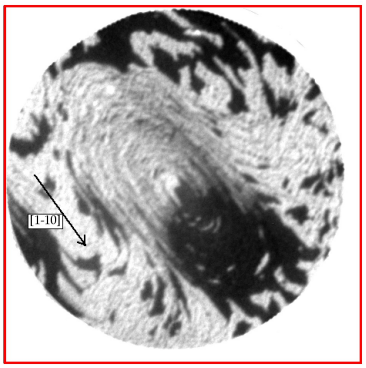

Figure 7.6: Darfield with spot A, E=28 eV a) fov=6 μm.

is extended over $\sim 80\%$ of the surface. In figure 7.6 we show a darkfield image of a mesa structure, a hill elongated along the $[1\bar{1}0]$ direction. We know that the crystal presented a small ($0.5\,^{\circ}$) miscut along the $[1\bar{1}0]$ direction, and so we can assign the steps in the bright region as "climbing up" ones while the others are going down; hence the prevailing domain all over the surface, which is bright in this image, is the one laying on the ascending terraces. Since the oxide starts to grow *from* the steps, it is quite intuitive to think that one of the two domains will be favoured to grow from an ascending step, while the other (which is symmetric) will start from the descending one. Therefore we can explain the average discrepancy between the area coverages of the two otherwise equivalent domains with the intrinsic miscut of the rhodium crystal.

The unequal domain distribution over the surface that we have just presented refers to a first oxide, prepared on a pristine surface. We once prepared on purpose a "disordered" oxide: after making a standard oxide, we titrated it using H_2; from STM we know that the resulting (1×1) surface is not as smooth as the one which is obtained after a *sputtering+annealing* treatment: it has indeed a high density of added Rh segments, like the surfaces in figures 7.1 and 7.2f.

The morphology of the oxide grown on such a rough (1×1) is remarkably different from that of the first oxide: as shown in figure 7.7, the domains are much smaller than in the flat oxide case; moreover, image analysis shows that they are equally distributed. Brightfield LEEM, in addition, showed a high density of steps. This oxide can be described as disordered or rough based on both atomic and mesoscopic scale measurements, thus suggesting a link between the morphology of the (1×1) surface over which the oxide is grown and the size and distribution of the domains.

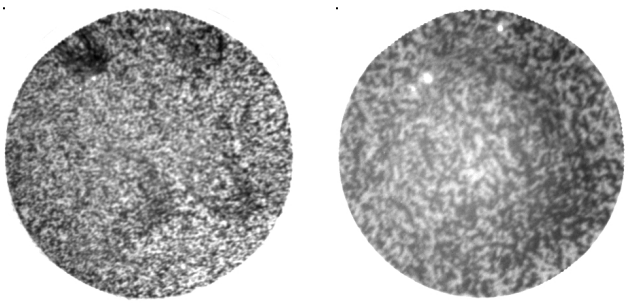

(a) (b)

Figure 7.7: Darfield with spot A, E=28 eV a) fov=20 μm; b) fov=6 μm.

As presented below, with LEEM we were also able to relate the oxides reactivity upon H_2 dosing to their morphology: on the "rough" oxide the reaction front was significantly lower than on the flat one.

7.2.2 H_2 titration reactions

The following movies have been recorded with the LEEM letting hydrogen flow into the microscope's chamber during measurements. Here we display reactivity data regarding three different oxides, namely:

- an incomplete oxide, covering a fraction of the surface;
- a complete oxide formed with the thermal cracker atomic oxygen source;
- the "disordered" oxide, prepared right after a reaction of a complete oxide.

The two relevant parameters for reactivity studies that we could estimate from our movies were, as for the STM case, the induction time prior to the ignition of the reaction front and the speed of the front itself. For imaging the first two reactions, we used the brightfield mode of LEEM: the contrast mechanism in these cases is simply given by structural differences between the oxide and the adsorption structures. To be able to recognize each structure at a given energy, we recorded I/V curves for the (0,0) LEED spot[7]. From figure 7.8 it is clear that the surface oxide (trilayer) will show up as darker than any other oxygen adsorption structure at 19 eV, while above 30 eV it will be the opposite case.

[7]For more details, see chapter 2.5.

In the following, the first movie presents the oxide as dark while it is bright in the second.

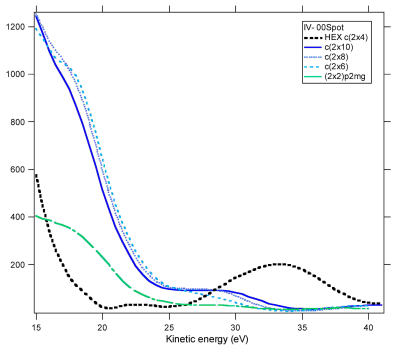

Figure 7.8: I/V curve of the (0,0) LEED spot.

Figure 7.9 shows snapshots from the movie of the oxide titration by H_2 at a temperature of $\sim 150\,^{\circ}C$[8]. The oxide covers nearly 20% of the surface, while the remaining area is covered by adsorption structures, mainly the (10×2) and the $c(2 \times 8)$. The reaction front starts, after $\sim 22\,L$ of H_2 dosing, from the adsorption structures, over which the hydrogen dissociation proceeds much faster than on the oxide. The induction time (and dose) is the same as in the first STM case; from STM we know that during induction the oxide undergoes a partial deconstruction, leading to the formation of the $c(2 \times 4)$ network of O vacancies. In the LEEM movie, prior to the front we can already see a slight shrink of the oxide islands, indicating a second pathway in which hydrogen is dissociated at the islands' borders. Anyway, this mechanism is unfavoured with respect to the other one, and the front removes oxide and adsorption structures with the same rate[9]; the estimated front speed was $\sim 26\,nm/sec$. After front propagation, the surface displays a (1×2) reconstruction with adsorbed oxygen, which is slowly removed in a homogeneous way.

[8]This temperature was chosen to be comparable to the one previously used in STM reactions.

[9]In fact, the front does not break when crossing and oxide island.

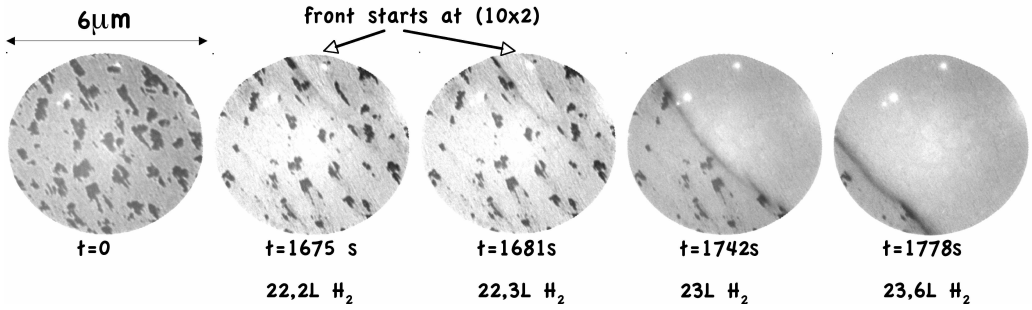

Figure 7.9: H_2 titration reaction of an incomplete oxide. E=19 eV, fov=6 μm, T$\sim$ 160 $^\circ C$, $p_{H2} \sim 1 \times 10^{-8}$ mbar .

The next figure (7.10) shows the titration reaction over a first complete oxide. The electron energy was set to 31 eV so that the oxide appears brighter than the $c(2 \times 2n)$ adsorption structures (see fig. 7.8). On this surface and at this energy the reaction front is clearly distinguishable: from its low intensity we can infer that it is composed of oxygen containing species, most probably OH. Behind the front, the intensity in the brightfield images increases again due to the subsequent deconstruction into the (1×2) and (1×1) structures.

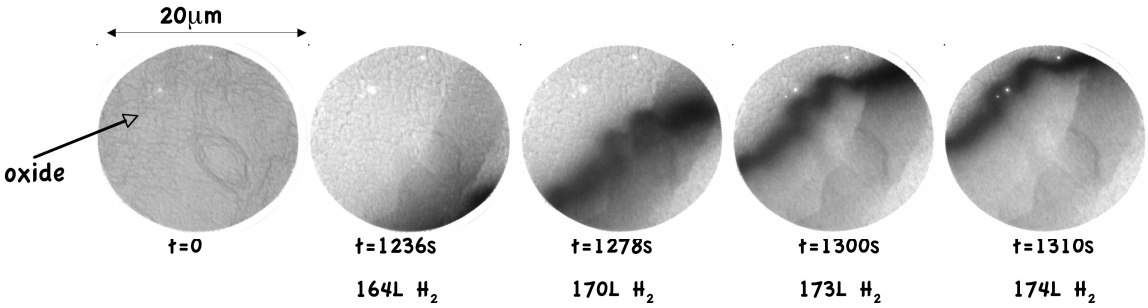

Figure 7.10: H_2 titration reaction of a complete surface oxide. E=31 eV, fov=20 μm, T$\sim$ 150 $^\circ C$, $p_{H2} \sim 1 \times 10^{-7}$ mbar .

The partial O_2 pressure was 10 times higher than in the incomplete oxide case, so a direct comparison between the front speeds is not feasible. The induction dose, however, was 8 times higher in the oxide case, supporting the idea that the trilayer is less reactive for H_2 dissociation than the adsorption structures. The front speed on the complete oxide was estimated to be $\sim$ 240 nm/sec. Looking for a common scaling law for the two reactions, we

realized that both oxides obey to the following expression:

$$\frac{V_{front}}{p_{H_2}} \sim const \sim 2.5 \times 10^9 \tag{7.1}$$

Such a condition is fullfilled when the front speed depends only on the oxygen consumption.

From the STM reaction over the complete oxide we estimated a front speed of $\sim 0.5\,\mathrm{nm/sec}$[10], with a hydrogen pressure of $p_{H_2} \sim 4.4 \times 10^{-9}\,\mathrm{mbar}$. This leads to a value $V_{front}/p_{H_2} \sim 1 \times 10^8$, therefore lower than what obtained from the first two LEEM movies. However, the temperature was nearly 50 °C lower than in the LEEM movies, and according to refs. [105, 106] this can lead to a decrease in the front speed of about one order of magnitude. Taking this into account, we get a value for the V_{front}/p_{H_2} ratio which is comparable to the one in equation 7.1.

To study the domain boundary influence on the reaction front speed, we titrated the disordered oxide of figure 7.7, that had a completely different domains size and distribution from the previous cases; to image the oxide domains, we followed this reaction using the LEEM darkfield mode. Since we set the same H_2 pressure and temperature, we could easily compare this reaction to that on the complete oxide. The induction time was ~ 8 times smaller, and this can be explained by the surface morphology, as a defects-rich surface offers more sites for hydrogen dissociation. However, the front speed was 5 times lower ($\sim 60\,\mathrm{nm/sec}$, fig. 7.11) than on the complete oxide. We exclude that this is due to a different stoichiometry: the oxide, in fact, was prepared with the same oxygen exposure but on a rough substrate. The different behaviour might be instead related to the high density of domain boundaries and defects. As a consequence, the expression in eq. 7.1 does not provide the same constant as for a complete oxide

The second oxide that was titrated during STM measurements (the one coexisting with adsorption structures) resembled much more the "disordered" oxide than the incomplete one of the LEEM data series: it was rich in domain boundaries as the former, and covered the great part of the surface, unlike the latter. STM observations on such an heterogeneous surface evidenced a lower V_{front}/p_{H_2} ratio than in the STM complete oxide case, despite being performed at the same temperature. Since the H_2 pressure was higher, the front speed was lower than expected from the scaling law. This surface presented a much higher density of phase and domain boundaries than the complete oxide one,

[10]This value is not as reliable as that obtained by LEEM, because LEEM is a parallel imaging techinque. In STM the data pixels of one image are not acquired at the same time.

and its behaviour upon titration is hence in agreement with the one of the rough oxide observed in the LEEM experiment described above.

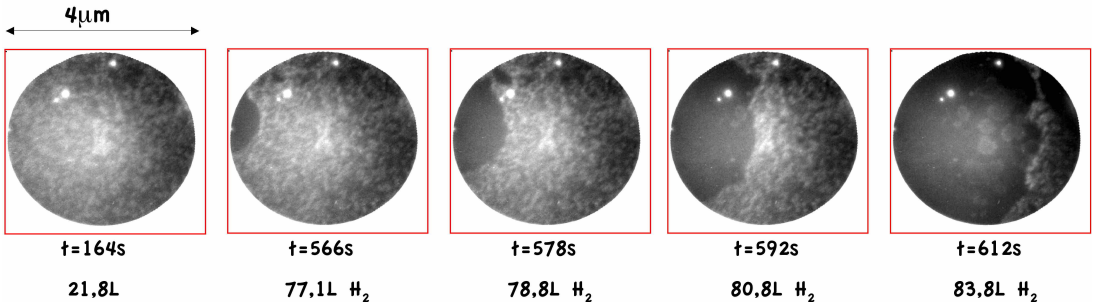

Figure 7.11: H_2 titration reaction of a disordered oxide; DARKFIELD imaging with LEED spot A. E=30 eV, fov=4 μm, T$\sim$ 140 $^\circ C$, $p_{H2} \sim 1 \times 10^{-7}$ mbar .

In conclusion, in this chapter we presented a series of hydrogen titration reactions over different surface oxides; while STM provided the atomic scale information on the reaction pathway, LEEM allowed us to link, at least qualitatively, the oxides morphology and reactivity. The LEEM experiments allowed us to verify that front velocity and H2 pressure are linked by a scaling law only for the case of well-prepared smooth oxide surfaces. This indicates that the front speed is set by the oxygen consumption rate. A significantly lower velocity to pressure ratio was instead observed on surfaces with a high density of domains boundaries, i.e. oxides grown on rough substrates. We hypotize that the reduced front velocity can be explained by the existence of kinetic barriers across the domain boundaries that hinder the diffusion of reaction intermediates like OH species.

Chapter 8

Conclusions

In this thesis, the capabilities of surface science equipments and techniques for studying the ageing of a model catalyst were exploited.

For this purpose, we moved towards real catalysis under two different aspects: by trying to bridge, al least partially, the "pressure gap" when oxidizing the Rh(110) single crystal and by setting up an ageing protocol in UHV ambient. The oxides were formed with three different oxygen sources and studied with TDS to understand their desorption mechanism, and with STM to look at their structures down to single-atom scale. LEEM and XPS complemented our measurements, providing large scale and chemical information, respectively.

A first relevant result of this thesis is that using high pressure molecular oxygen we could form thicker oxides than previously possible. Furthermore, we also highlighted the importance of the O_2 dissociation step in oxides formation and ageing.

The ageing protocol that mimics real catalytic oxidation conditions consisted of an oxidation followed by an annealing, repeated in cycles up to more than ~ 40 times, without cleaning the sample in between. This goes beyond the usual surface science approach, and allowed us to observe huge changes in the oxides desorption and morphology.

Due to the extreme oxidation conditions and to the iterative procedure, when using the thermal cracker oxygen source we had to face unforeseen presence of contaminants, whose accumulation lead to a first kind of ageing that we named "contaminant driven". We detected a second, more intriguing kind of ageing that seems not to be related to any contaminant, and that we therefore named "intrinsic": it was thoroughly characterized for the case of the molecular oxygen cycles, but was also detected in the presence of contaminants, even if shadowed.

An important result, however, is that regardless of the kind of ageing, the general oxide desorption mechanism was always the same. The degree of ageing was found to be dependent on the amount of a newly observed species, the "units", remaining on the metallic surface after oxide desorption and that is most probably composed of oxygen and rhodium atoms. Furthermore, we demonstrated that by reducing the density of this species, a recover of the oxide characteristics was possible, i.e. that the intrinsic ageing was partially reversible.

We believe that the units may play a crucial role in the ageing process: therefore more studies are needed to definitively unravel their chemical composition and structure; Photo-Electron Diffraction measurements and DFT calculations will probably be the best techniques to tackle this issue.

As an outlook towards future studies triggered by this work, we list the following. Based on our reactivity studies on first oxides, STM and LEEM measurements on progressively aged oxides will help in deeper understanding of the ageing.

Starting from the atomically resolved information obtained in this work, one subsequent step towards real catalysis will be to connect a high pressure cell to the UHV chamber and perform the oxidation cycles again over the Rh single crystal, but at industrially relevant oxygen pressures, while retaining the possibility of using surface science techniques for chacterization. On the other side, it would be interesting to increase the complexity of the model catalyst, for example applying our cycle recipe to Rh nanoparticles, while remaining under UHV atmosphere.

In conclusion, with this thesis we addressed the issue of the oxidative ageing of a model catalyst, thereby linking real catalysis and surface science to get an insight into a process of great relevance as the progressive deterioration of a catalytic material.

Appendix 1

A.1 List of acronyms

AES Auger Electron Spectroscopy

DFT Density Functional Theory

DOS density of states

LDOS local density of states

LEED Low Energy Electron Diffraction

LEEM Low Energy Electron Microscopy

RGA Residual Gas Analyzer

PBN Pyrolytic Boron Nitride

QMS quadrupole mass spectrometer

RT room temperature

SEM Scanning Electron Microscopy

SPEM Scanning PhotoEmission Microscopy

SSR Surface Structure and Reactivity

STM Scanning Tunneling Microscopy

TDS Thermal Desorption Spectroscopy

TEM Transmission Electron Microscopy

TPD Temperature Programmed Desorption

TWC Three Way Catalyst

UHV Ultra High Vacuum

XPS X-ray Photoelectron Specroscopy

Appendix 2

B.2 Molecular oxygen cycles overview

TDS spectra of the 46 oxide formed by molecular oxygen dosing at 400 °C. The "MAX" ones are obtained by dosing with the maximum pressure, i.e. $p_{O_2} \sim 1 \times 10^{-5}$ mbar in the chamber.

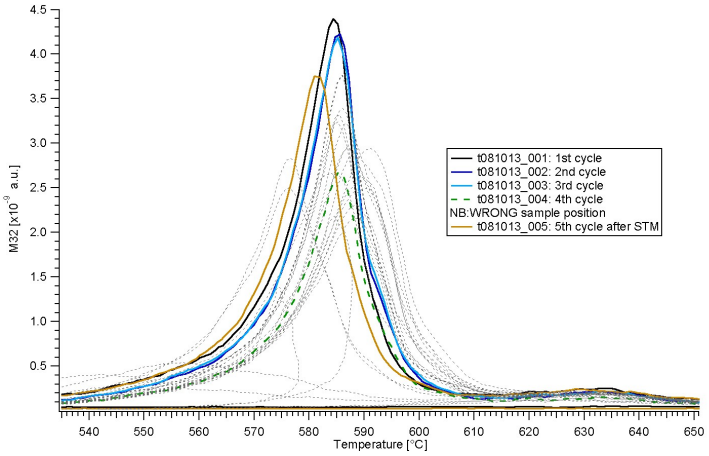

(a) 1^{st}-5^{th} oxide

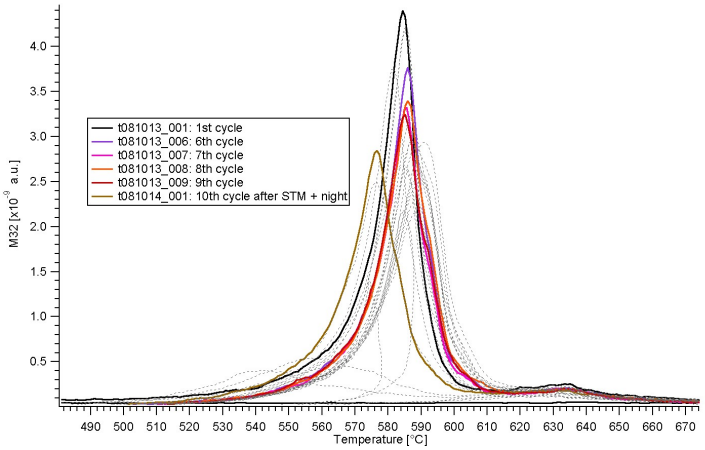

(b) 6^{th}-10^{th} oxide

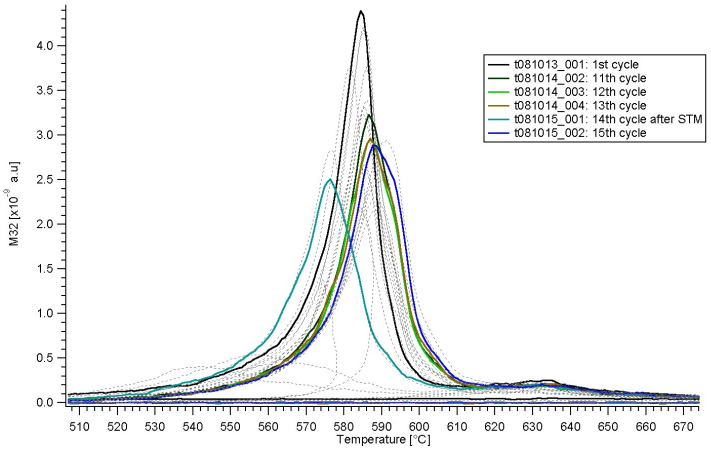

(c) 10^{th}-15^{th} oxide

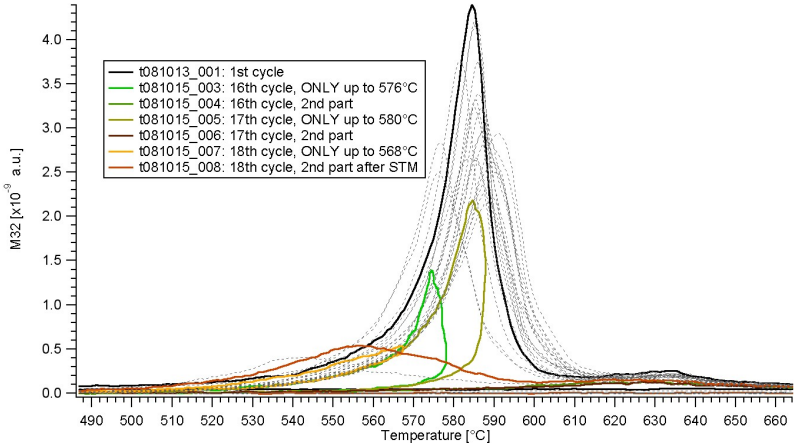

(d) 16^{st}-18^{th} oxide

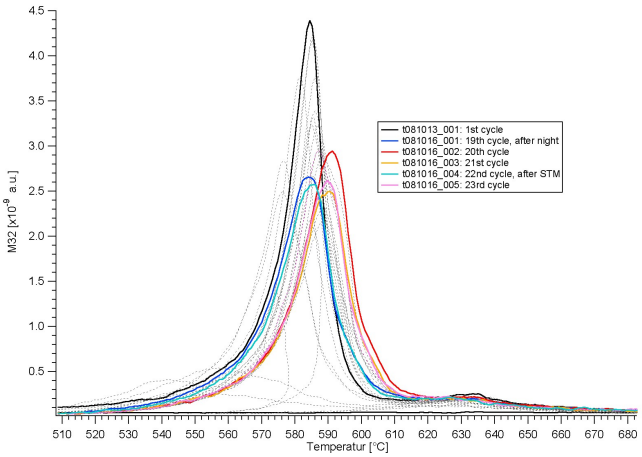

(e) 19^{th}-23^{rd} oxide

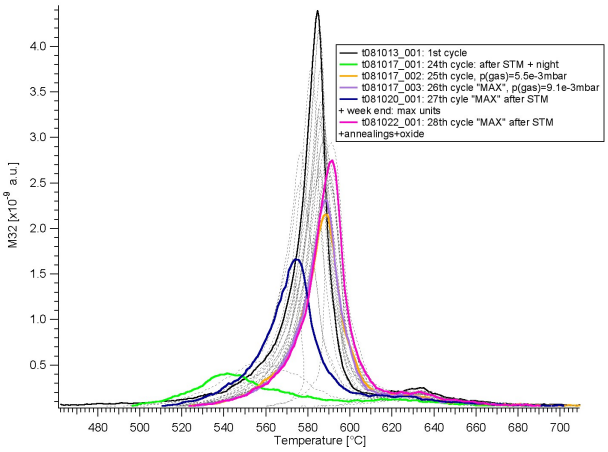

(f) 24^{th}-28^{th} oxide

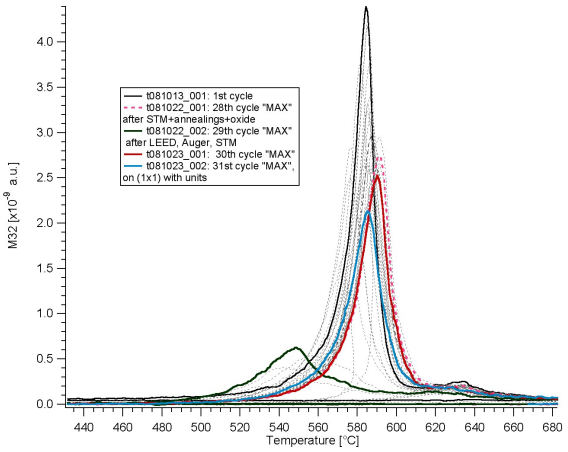

(g) 29^{th}-31^{st} oxide

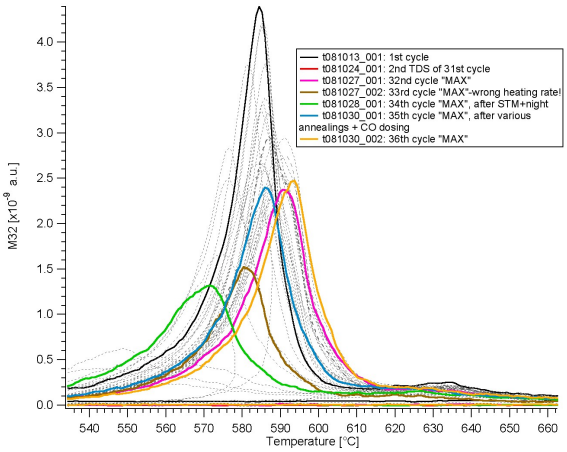

(h) 32^{nd}-36^{th} oxide

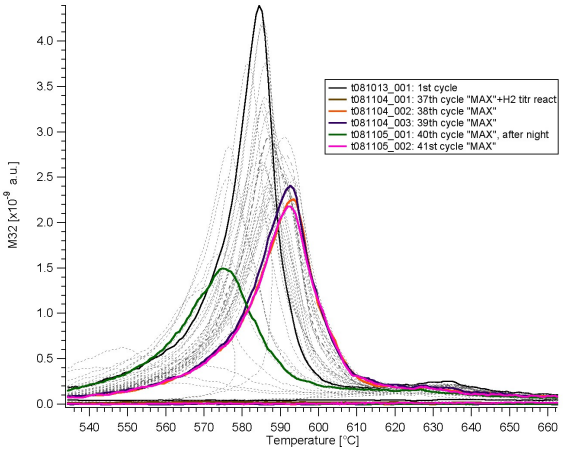

(i) 37^{th}-41^{st} oxide

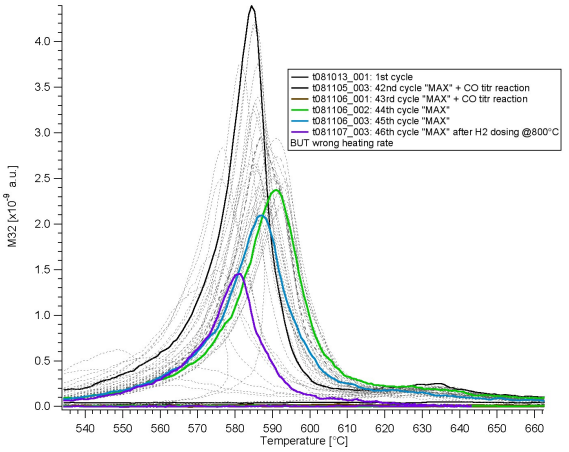

(j) 42^{nd}-46^{th} oxide

Bibliography

[1] I. Chorkendorff and J. W. Niemantsverdriet, *Concepts of Modern Catalysis and Kinetics* (Wiley-VCH, 2003).

[2] J. Thomas and W. Thomas, *Principles and Practice of Heterogeneos Catalysis* (Wiley-VCH, 1997).

[3] G. Ertl, H. Knötzinger, and J. Weitkamp, *Environmental Catalysis* (Wiley-VCH, 1999).

[4] G. Ertl, H. Knötzinger, F. Schüth, and J. Weitkamp, *Handbook of heterogeneous catalysis* (Wiley-VCH, 2008).

[5] C. Satterfield, *Heterogeneous Catalysis in Practice* (Mc Graw Hill, 1980).

[6] P. Nolte, A. Stierle, N. Y. Jin-Phillipp, N. Kasper, T. U. Schulli, and H. Dosch, *Schape changes of Supported Rh Nanoparticles During Oxidation and Reduction Cycles*, Science **321**, 1654 (2008).

[7] H. S. Gandhi, G. W. Graham, and R. W. McCabe, *Automotive exhaust catalysis*, Journal of Catalysis **216**, 433 (2003).

[8] C. Campbell, Surf. Sci.Rep. **27**, 1 (1997).

[9] S. Street, C. Xu, and D. Goodman, Annu.Rev.Phys.Chem. **48**, 43 (1997).

[10] C. Henry, Surf. Sci.Rep. **31**, 157 (1998).

[11] H.-J. Freund, Phys.Stat.Sol.(b) **192**, 407 (1995).

[12] H.-J. Freund, *Model systems in heterogeneos catalysis: Selectivity studies at the atomic level*, Topics in Catalysis **48**, 137 (2008).

[13] J. Niemantsverdriet, *Spectroscopy in Catalysis* (Wiley-VCH, 2000).

[14] F. Besenbacher, J. V. Lauritsen, and S. Wendt, *Stm studies of model catalysts*, Nano Today **2**, 30 (2007).

[15] T. Risse, S. Shaikhutdinov, N. Nilius, M. Sterrer, and H.-J. Freund, *Gold supported in thin oxide films: From single atoms to nanoparticles*, Acc.Chem.Res. **41**, 949 (2008).

[16] C. H. Bartholomew, *Mechanisms of catalyst deactivation*, Applied Catalysis A: General **212**, 17 (2001).

[17] K. Kallinen, A. Suopanki, and M. Härkönen, *Laboratory scale simulation of three-way catalyst engine ageing*, Catalysis Today **100**, 223 (2005).

[18] L. Martin, J. L. Arranz, O. Prieto, R. Trujillano, M. J. Holgado, M. A. Galan, and V. Rives, *Simulation three-way catalyst ageing: Analysis of two conventional catalyst*, Applied Catalysis B: Environmental **44**, 41 (2003).

[19] G. Rupprechter and C. Weilach, *Mind the gap! spectroscopy of catalytically active phases*, Nano Today **2**, 20 (2007).

[20] G. Ketteler, F. D. Ogletree, H. Bluhm, H. Liu, E. L. D. Hebenstreit, and M. Salmeron, *In Situ Spectroscopic Study of the Oxidation and Reduction of Pd(111)*, Journal of the Americal Chemical Society **127**, 18269 (2005).

[21] B. L. M. Hendriksen, S. C. Bobaru, and J. W. M. Frenken, *Looking at heterogeneous catalysis at atmospheric pressure using tunnel vision*, Topics in Catalysis **36**, 43 (2005).

[22] R. Westerström, J. Gustafson, A. Resta, A. Mikkelsen, J. N. Andersen, E. Lundgren, N. Seriani, F. Mittendorfer, M. Schmid, J. Klikovits, et al., *Oxidation of Pd(553): From ultrahigh vacuum to atmospheric pressure*, Phys. Rev. B **76**, 155410 (2007).

[23] J. Gustafson, A. Mikkelsen, M. Borg, E. Lundgren, L. Köhler, G. Kresse, M. Schmid, P. Varga, J. Yuhara, X. Torrelles, et al., *Self-limited growth of a thin oxide layer on Rh(111)*, Phys. Rev. Lett. **92**, 126102 (2004).

[24] C. Dri, C. Africh, F. Esch, G. Comelli, O. Dubay, L. Koehler, F. Mittendorfer, G. Kresse, P. Dudin, and M. Kiskinova, *Initial oxidation of the Rh(110) surface: Ordered adsorption and surface oxide structures*, The Journal of Chemical Physics **125**, 094701 (2006).

[25] J. Klikovits, M. Schmid, L. R. Merte, P. Varga, R. Westerstrom, A. Resta, J. N. Andersen, J. Gustafson, A. Mikkelsen, E. Lundgren, et al., *Step-orientation-dependent oxidation: From 1d to 2d oxides*, Phys. Rev. Lett. **101**, 266104 (2008).

[26] J. Gustafson, R. Westerström, A. Mikkelsen, J. N. Andersen, A. Resta, O. Balmes, X. Torrelles, M. Schmid, P. Varga, B. Hammer, et al., *Structure and catalytic reactivity of Rh oxides*, Catalysis Today, in press (2009).

[27] D. Zemlyanov, B. Aszalos-Kiss, E. Kleimenov, D. Teschner, S. Zafeiratos, M. Hävecker, A. Knop-Gericke, R. Schlögl, H. Gabasch, W. Unterberger, et al., *In situ XPS study of Pd(1 1 1) oxidation. Part 1: 2D oxide formation in 10-3 mbar O_2*, Surface Science **600**, 983 (2006).

[28] H. Gabasch, W. Unterberger, K. Hayek, B. Klötzer, E. Kleimenov, D. Teschner, S. Zafeiratos, M. Hävecker, A. Knop-Gericke, R. Schlögl, et al., *In situ XPS study of Pd(1 1 1) oxidation at elevated pressure, Part 2: Palladium oxidation in the 10-1 mbar range*, Surface Science **600**, 2980 (2006).

[29] H. Gabasch, W. Unterberger, K. Hayek, B. Klötzer, G. Kresse, C. Klein, M. Schmid, and P. Varga, *Growth and decay of the Pd(1 1 1) / Pd_5O_4 surface oxide: Pressure-dependent kinetics and structural aspects*, Surface Science **600**, 205 (2006).

[30] A. J. Titkov, A. N. Salanov, S. V. Koscheev, and A. Boronin, *Mechanisms of Pd(1 1 0) surface reconstruction and oxidation: XPS, LEED and TDS study*, Surface Science **600**, 4119 (2006).

[31] J. Han, D. Y. Zemlyanov, and F. H. Ribeiro, *Interaction of O_2 with Pd single crystals in the range 1-150 Torr: Surface morphology transformations*, Surface Science **600**, 2730 (2006).

[32] J. Han, D. Y. Zemlyanov, and F. H. Ribeiro, *Interaction of O_2 with Pd single crystals in the range 1-150 Torr: Oxygen dissolution and reaction*, Surface Science **600**, 2752 (2006).

[33] M. D. Ackermann, T. M. Pedersen, B. L. M. Hendriksen, O. Robach, S. C. Bobaru, I. Popa, C. Quiros, H. Kim, B. Hammer, S. Ferrer, et al., *Structure and reactivity of surface oxides on Pt(110) during catalytic CO oxidation*, Phys. Rev. Lett. **95**, 255505 (2005).

[34] J.-D. Grunwaldt, M. Caravati, and A. Baiker, *Oxidic or metallic palladium: Which is the active phase in Pd-catalyzed aerobic alcohol oxidation?*, The Journal of Physical Chemistry B Letters (2006).

[35] H. S. Grunwaldt, Jan-Dierk, C. G. Schroer, and A. Baiker, *2D-Mapping of the Catalyst Structure Inside a Catalytic Microreactor at Work: Partial*

Oxidation of Methane over Rh/Al_2O_3, Journal of Physical Chemistry B **110**, 8674 (2006).

[36] H. Over, Y. D. Kim, A. P. Seitsonen, S. Wendt, E. Lundgren, M. Schmid, P. Varga, A. Morgante, and G. Ertl, *Atomic-scale structure and catalytic reactivity of the RuO_2(110) surfaces*, Science **287**, 1474 (2000).

[37] E. Lundgren, A. Mikkelsen, J. N. Andersen, G. Kresse, M. Schmid, and P. Varga, *Surface oxides on close-packed surfaces of late transition metals*, J.Phys.: Condens.Matter **18**, R481 (2006).

[38] G. Binnig, H. Rohrer, C. Gerber, and E. Weibel, *Surface studies by scanning tunneling microscopy*, Phys. Rev. Lett. **49**, 57 (1982).

[39] G. Binnig, H. Rohrer, C. Gerber, and E. Weibel, *Tunneling through a controllable vacuum gap*, Appl. Phys. Lett. **40**, 178 (1982).

[40] G. Binnig and H. Rohrer, in *Nobel lecture* (1986), URL `http://nobelprize.org/nobel_prizes/physics/laureates/1986/binnig-lecture.pdf`.

[41] C.Dri, *Characterization and manipulation of single molecules and molecular complexes by low temperature scanning tunneling microscopy.*, Ph.D. thesis, Università degli Studi di Trieste (2008).

[42] C. Africh, *Atomic scale investigations of model catalysts for oxidation reactions*, Ph.D. thesis, Università degli Studi di Trieste (2004).

[43] N.Nilius, *Light Emission spectroscopy with the STM - in "Probing the Nanoworld"*, vol. 34 of *Matter and Materials* (Forschungszentrum Juelich, 2007).

[44] G. A. Somorjai and J. Y. Park, *Evolution of the surface science of catalysis from single crystals to metal nanoparticles under pressure*, The Journal of Chemical Physics **128**, 182504 (2008).

[45] R. Temirov, S. Soubatch, O. Neucheva, A. C. Lassise, and F. S. Tautz, *A novel method achieving ultra-high geometrical resolution in scanning tunnelling microscopy*, New Journal of Physics **10**, 053012 (2008).

[46] K.Christmann, *Introduction to Surfaces Physical Chemistry* (1991).

[47] J. Wintterlin and R. J. Behm, *Scanning Tunneling Microscopy*, vol. I (Springer, Berlin, 1992).

[48] C. J. Chen, *Introduction to scanning tunneling microscopy* (Oxford University Press, 1993).

[49] R. J. Behm and W. Hösler, *Chemistry and Physics of Solid Surfaces*, vol. IV (Springer, Berlin, 1986).

[50] J. Bardeen, *Tunnelling from a many–particle point of view*, Phys. Rev. Lett. **6**, 57 (1961).

[51] J. Tersoff and D. R. Hamann, *Theory and application for the scanning tunneling microscope*, Phys. Rev. Lett. **50**, 1998 (1983).

[52] J. Tersoff and D. R. Hamann, *Theory of the scanning tunneling microscope*, Phys. Rev. B **31**, 805 (1985).

[53] I. Ekvall, E. Wahlström, D. Claesson, H. Olin, and E. Olsson, *Preparation and characterization of electrochemically etched W tips for STM*, Meas. Sci. Technol. **10**, 11 (1999).

[54] F. Calleja, *Contrast reversal and shape changes of atomic adsorbates measured with scanning tunneling microscopy*, Physical Review Letters **92**, 206101 (2002).

[55] N. D. Lang, *Theory of single-atom imaging in the scanning tunneling microscope*, Phys. Rev. Lett. **56**, 1164 (1986).

[56] I. Tilinin, M. Rose, J. Dunphy, M. Salmeron, and M. V. Hove, Surface Science **418**, 511 (1998).

[57] E. K. G. Doyen, D. Drakova and R. B. (1988), J. Vac. Sci. Technol. A **6**, 327 (1988).

[58] D. P.Woodruff and T. A.Delchar, *Modern techniques of surface science* (Cambridge University press, 1986).

[59] P.Redhead, Vacuum **12**, 203 (1963).

[60] D.King, *Thermal desorption from metal surfaces: a review*, Surface Science **46**, 384 (1975).

[61] G. Comelli, V. R. Dhanak, M. Kiskinova, K. C. Prince, and R. Rosei, *Oxygen and nitrogen interaction with rhodium single crystal surfaces*, Surf.Sci. Rep. **32**, 165 (1998).

[62] B. Klötzer, K. Hayek, C. Konvincka, E. Lundgren, and P. Varga, *Oxygen-induced surface phase transformation of Pd(111): sticking, adsorption and desorption kinetics*, Surface Science **482-485**, 237 (2001).

[63] G. Ertl and J. Kuppers, *Low Energy Electrons and Surface Chemistry* (Verlag Chemie, 1985).

[64] N. Ashcroft and D. Mermin, *Solid State Physics* (Saunders College Publishing, 1976).

[65] A. Einstein, Annalen der Physik **132**, 17 (1905).

[66] P. Dudin, A. Barinov, L. Gregoratti, M. Kiskinova, F. Esch, C. Dri, C. Africh, and G. Comelli, *Initial Oxidation of a Rh(110) Surface Using Atomic or Molecular Oxygen and Reduction of the Surface Oxide by Hydrogen*, The Journal of Physical Chemistry B **109**, 13649 (2005).

[67] URL `http://en.wikipedia.org`.

[68] E. Bauer, Ultramicroscopy **17**, 51 (1985).

[69] E. Bauer, *Leem basics*, Surface Review and Letters **5**, 1275 (1998).

[70] E. Bauer, *Low energy electron microscopy*, Rep. Prog. Phys. **57**, 895 (1994).

[71] URL `http://www.elettra.trieste.it/nanospectroscopy`.

[72] T. O. Mentes, N. Stojic, N. Binggeli, N. M. A., A. Locatelli, L. Aballe, M. Kiskinova, and E. Bauer, *Strain relaxation in small adsorbate islands: O on W(110)*, Phys. Rev. B **77**, 155414 (2008).

[73] URL `http://physics.ust.hk/department/phaltman/leem/`.

[74] T. Schmidt, S. Heun, J. Slezak, J. Diaz, K. C. Prince, G. Lilienkamp, and E. Bauer, *SPELEEM: Combining LEEM and Spectroscopic Imaging*, Surface Review and Letters **5**, 1287 (1998).

[75] E. Bauer, *Photoelectron spectromicroscopy: present and future*, Journal of Electron Spectroscopy and Related Phenomena **114-116**, 975 (2001).

[76] S. Günther, B. Kaulich, L. Gregoratti, and M. Kiskinova, *Photoelectron microscopy and applications in surface and material science*, Progress in Surface Science **70**, 187 (2002).

[77] A. Locatelli, C. Sbraccia, S. Heun, S. Baroni, and M. Kiskinova, *Energetically Driven Reorganization of a modified surface under Reaction Conditions*, Journal of the American Chemical Society **127**, 2351 (2005).

[78] A. Locatelli, T. O. Mentes, L. Aballe, A. Mikhailov, and M. Kiskinova, *Formation of Regular Surface-Supported Mesostructures with Periodicity Controlled by Chemical Reaction Rate*, The Journal of Physical Chemistry B Letters **110**, 19108 (2006).

[79] C. Dri, Master's thesis, Università degli Studi di Trieste (2004).

[80] A. Spessot, Master's thesis, Università degli Studi di Trieste (2003).

[81] O. A. Research, *Universal thermal cracker for surface science*, Tech. Rep. (2005), URL `www.oaresearch.co.uk/oaresearch/brochures/TC50ApplicationNotes.pdf`.

[82] O. A. Research, *Thermal cracker application note*, Tech. Rep. (2005), URL `www.oaresearch.co.uk/oaresearch/brochures/TCSeries.pdf`.

[83] Tectra, *Application Note: Plasma Atom Source GenII*, Tech. Rep., Tectra GmbH (2005), URL `www.tectra.de`.

[84] C. Africh and G. Comelli, *Scanning Tunnelling Microscopy Investigations of Simple Surface Reactions on Rh(110)*, J. Phys.: Condens. Matter **18**, R387 (2006).

[85] C. Africh, F. Esch, G. Comelli, and R. Rosei, *Dynamics of the o induced reconstruction of the Rh(110) surface: A scanning tunnelling microscopy study*, J. Chem. Phys. **115**, 477 (2001).

[86] J. Gustafson, A. Mikkelsen, M. Borg, J. N. Andersen, E. Lundgren, C. Klein, W. Hofer, M. Schmid, P. Varga, L. Köhler, et al., *Structure of a thin oxide film on rh(100)*, Phys. Rev. B **71**, 115442 (2005).

[87] E. Lundgren, G. Kresse, C. Klein, M. Borg, J. N. Andersen, M. De Santis, Y. Gauthier, C. Konvicka, M. Schmid, and P. Varga, *Two-Dimensional Oxide on Pd(111)*, Phys. Rev. Lett. **88**, 246103 (2002).

[88] C. T. Campbell, *Surface science: Enhanced: Waltzing with o2*, Science **299**, 357 (2003).

[89] R. Schaub, E. Wahlstrom, A. Ronnau, E. Lagsgaard, I. Stensgaard, and F. Besenbacher, *Oxygen-mediated diffusion of oxygen vacancies on the TiO_2(110) surfaces*, Science **299**, 377 (2003).

[90] F. Esch, S. Fabris, L. Zhou, T. Montini, C. Africh, P. Fornasiero, G. Comelli, and R. Rosei, *Electron localization determines defect formation on ceria substrates*, Science **309**, 752 (2005).

[91] S. Ulrich, N. Nilius, and H.-J. Freund, *Growth of thin alumina films on a vicinal nial surface*, Surface Science **601**, 4603 (2007).

[92] J. F. Skelly, T. Bertrams, A. W. Munz, M. J. Murphy, and A. Hodgson, *Nitrogen induced restructuring of Cu(111) and explosive desorption of* N_2, Surface Science **415**, 48 (1998).

[93] C. D. Wagner, W. M. Riggs, L. E. Davis, J. F. Moulder, and G. E. Muilenberg, *Handbook of X-ray Photoelectron Spectroscopy* (Perkin Elmer Corporation, 1979).

[94] G. C. Koltsakis and A. M. Stamatelos, Prog. Energy Combust. Sci. **23**, 1 (1997).

[95] M. A. Härkönen, E. Aitta, A. Lahti, M. Luoma, and T. Maunula, SAE Techincal Paper Series p. 910846 (1991).

[96] P. R. Bevington and D. K. Robinson, *Data reduction and error analysis for the physical sciences* (Mc Graw Hill, 2002).

[97] A. Baraldi, V. R. Dhanak, G. Comelli, K. C. Prince, and R. Rosei, *Comparative study of the adsorption of CO, NO and hydrogen on (1x1) and (1x2) Rh(110)*, Surface Science **293**, 246 (1993).

[98] C. Africh, *Private communication*, Tech. Rep., INFM-CNR-TASC Laboratory (2003).

[99] C. Africh, L. Haiping, M. Corso, F. Esch, R. Rosei, W. A. Hofer, and G. Comelli, *Water Production Reaction on Rh(110)*, Journal of the American Chemical Society **127**, 11454 (2005).

[100] E. Vesselli, M. Campaniello, A. Baraldi, L. Bianchettin, C. Africh, F. Esch, S. Lizzit, and G. Comelli, *A Surface Core Level Shift Study of Hydrogen-Induced Ordered Structures on Rh(110)*, The Journal of Physical Chemistry C **112**, 14475 (2008).

[101] A. Spessot, F. Esch, C. Africh, C. Dri, and G. Comelli, *Real-time eye on chemical reactions: the fast-stm project*, in preparation (2009).

[102] C. Africh, F. Esch, G. Comelli, and R. Rosei, *Reactivity and deconstruction of the (1 x 2)-Rh(110) surface studied by scanning tunneling microscopy*, J. Chem. Phys. **116**, 7200 (2002).

[103] C. Blasetti, C. Africh, F. Esch, G. Comelli, T. O. Mentes, M. A. Nino, and A. Locatelli, in *LEEM PEEM 6 International Conference* (2008).

[104] IBM, *How does a leem work?*, Tech. Rep., IBM research (2006), URL `http://www.research.ibm.com/leem/`.

[105] F. Mertens and R. Imbihl, *Parameter-dependent anisotropy of front propagation in the H_2+O_2 reaction on Rh(110)*, Chemical Physics Letters **242**, 221 (1995).

[106] A. Makeev and R. Imbihl, *Simulations of anisotropic front propagation in the H_2 + O_2 reaction on a Rh(110) surface*, J. Chem. Phys. **113**, 3854 (2000).

Acknowledgements

I would like to thank my tutor Dr. Cristina Africh, who provided me systematic guidance throughout these PhD years. With both patience and firmness she taught me how to become an experimentalist, and a more self-confident person. My tutor Dr. Friedrich Esch was also important for this work: his ideas and enthusiasm always managed to convince me that the next *experiment would be easy and great. I am very grateful to my supervisor, Prof. Giovanni Comelli, for always having confidence in me, more than I did myself: without his help, this thesis would not have easily come to the end.*

A big thanks to the friends with whom I shared the days in the lab: Carlo, Nasiba and Florian, for being different but great examples to follow and to laugh with. Thanks to all the people from the TASC laboratory, especially the two Stefanos for cheering me up, and Silvia and Martina for hundreds of morning coffees. I would like to thank Erik and the staff of the SuperESCA beamline at Elettra, for their scientific and friendly contribution; and I do not want to forget Andrea ("Lupo"), Onur and Miguel from the Nanospectroscopy beamline, where I spent a very pleasant and useful month. I would like to thank Prof. Freund for giving me the opportunity to join his department at the world-renowed Fritz Haber Institute, Berlin: in one month I could see excellent research groups at work and learn a lot about science and life.

Thanks to Martina, for finishing her PhD right before me and reminding me that there is a life after graduation. Thanks to all my other friends for their kindness and support, and to my parents who sustained me with comprehension and affection.

In particular, I thank my husband Francesco, who had to hear too many times: "I just wanna do one more cycle...". He was always understanding with me, helping in practical and mood issues, and made me feel loved and optimistic.

Typeset with LaTeX 2ε. Trieste, March 5, 2009.